

On the limitations of Froude's actuator disc concept

Citation for published version (APA):

Kuik, van, G. A. M. (1991). *On the limitations of Froude's actuator disc concept*. [Phd Thesis 1 (Research TU/e / Graduation TU/e), Applied Physics and Science Education]. Technische Universiteit Eindhoven.
<https://doi.org/10.6100/IR345682>

DOI:

[10.6100/IR345682](https://doi.org/10.6100/IR345682)

Document status and date:

Published: 01/01/1991

Document Version:

Publisher's PDF, also known as Version of Record (includes final page, issue and volume numbers)

Please check the document version of this publication:

- A submitted manuscript is the version of the article upon submission and before peer-review. There can be important differences between the submitted version and the official published version of record. People interested in the research are advised to contact the author for the final version of the publication, or visit the DOI to the publisher's website.
- The final author version and the galley proof are versions of the publication after peer review.
- The final published version features the final layout of the paper including the volume, issue and page numbers.

[Link to publication](#)

General rights

Copyright and moral rights for the publications made accessible in the public portal are retained by the authors and/or other copyright owners and it is a condition of accessing publications that users recognise and abide by the legal requirements associated with these rights.

- Users may download and print one copy of any publication from the public portal for the purpose of private study or research.
- You may not further distribute the material or use it for any profit-making activity or commercial gain
- You may freely distribute the URL identifying the publication in the public portal.

If the publication is distributed under the terms of Article 25fa of the Dutch Copyright Act, indicated by the "Taverne" license above, please follow below link for the End User Agreement:

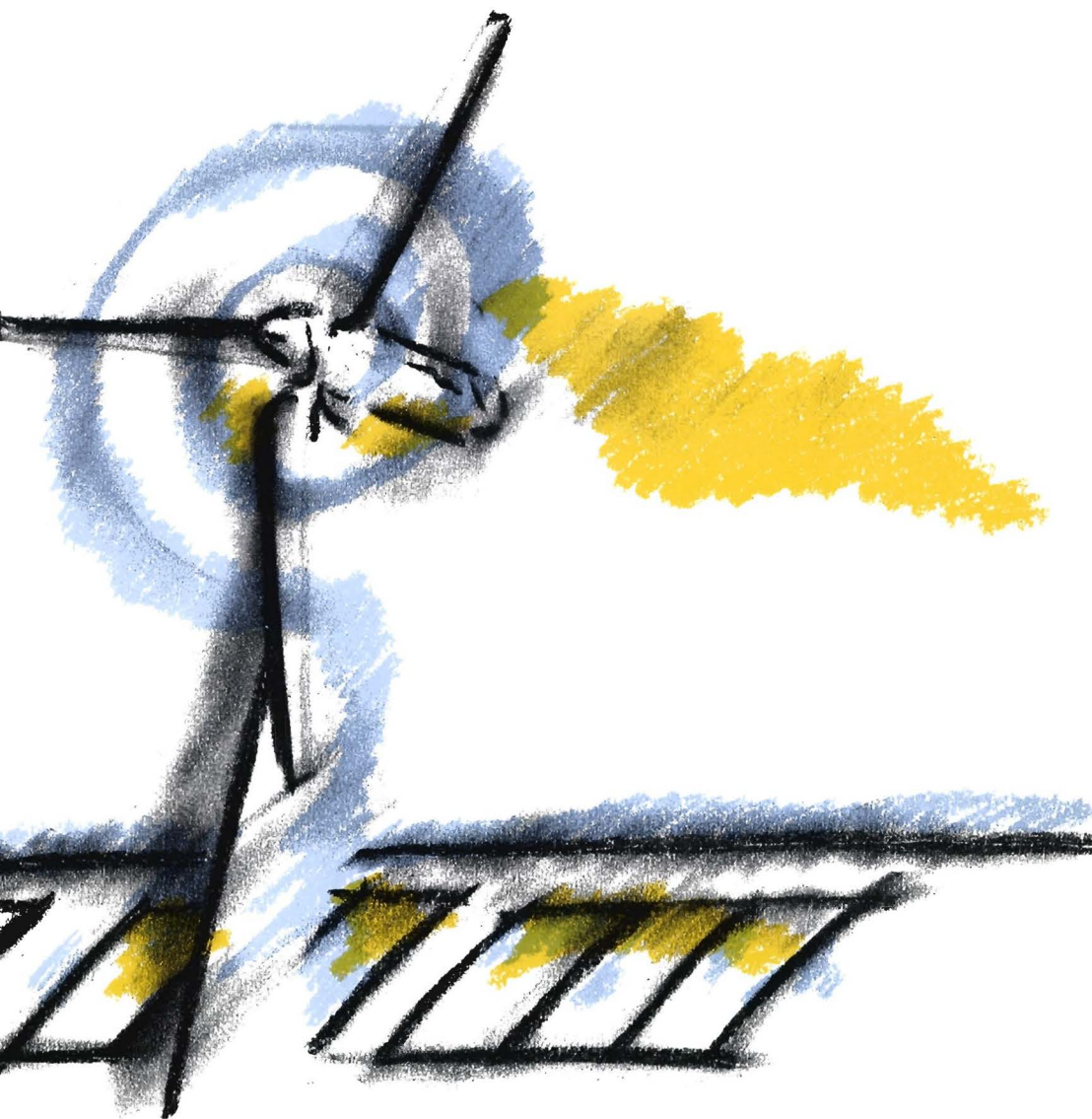
www.tue.nl/taverne

Take down policy

If you believe that this document breaches copyright please contact us at:

openaccess@tue.nl

providing details and we will investigate your claim.



**ON THE LIMITATIONS OF FROUDE'S
ACTUATOR DISC CONCEPT**

G.A.M. VAN KUIK

ON THE LIMITATIONS OF
FROUDE'S ACTUATOR DISC CONCEPT

ON THE LIMITATIONS OF FROUDE'S ACTUATOR DISC CONCEPT

PROEFSCHRIFT

ter verkrijging van de graad van doctor aan de Technische Universiteit Eindhoven, op
gezag van de Rector Magnificus, prof. ir. M. Tels, voor een commissie aangewezen
door het College van Dekanen, in het openbaar te verdedigen op
vrijdag 8 februari om 16.00 uur

door

Gijsbertus Arnoldus Maria van Kuik
geboren te Mierlo

Dit proefschrift is goedgekeurd door de promotoren:

prof. dr. ir. G. Vossers

en

prof. dr. ir. P.P.J.M. Schram

Copromotor: dr. ir. A. Hirschberg

Het onderzoek, beschreven in dit proefschrift, is uitgevoerd aan de Technische Universiteit Eindhoven, faculteit der Technische Natuurkunde, vakgroep Transportfysica, gebouw W & S, postbus 513, 5600 MB Eindhoven.

Druk: Anraad, Utrecht

Illustratie omslag: Gerda Vink, Rotterdam. Copyright CEA, Rotterdam

SUMMARY

The actuator disc is the first mathematical model of a propeller, helicopter- or wind turbine rotor, introduced by R.E Froude one century ago. His concept of the actuator disc concerns a permeable surface covered with a uniform normal load, which represents the action of the rotor. The performance prediction by momentum theory based on this concept is very simple, reason why it is still used to predict the performance of rotors. However, the accuracy of this prediction leaves much to be desired: a survey of experimental data shows that in all rotor flow states the average velocity of the flow through the rotor is 10 to 15% higher than predicted by momentum theory. This suggests a 'natural' concentration effect to be present: artificial concentrator systems such as rotors with shrouds or tipvanes show this increased mass flow through the rotor. The momentum theory for these concentrator systems shows that the appropriate way to account for this effect is to add edge forces to Froude's concept. The characteristic of these edge forces is that they are perpendicular to the local flow, so cannot perform work. Consequently, only a part of the total load on the rotor performs work. In Froude's actuator disc concept this distinction is not made: the entire load converts power.

The question arises whether the actuator disc including edge forces is a better representation of the action of conventional rotors than Froude's concept is. A confirmative answer is obtained in two ways. It is shown that the load on the chordwise bound vorticity of the rotor blade does not perform work, which conflicts with Froude's assumption of the load converting power being equal to the total load. Furthermore an experiment on a model rotor in hover has been conducted which indeed shows the load converting power to be smaller than the total load on the rotor. The wake contraction has been compared with the prediction by the momentum theory including edge forces. The agreement is very reasonable, in contrast with the classical prediction. The prediction of the average velocity through the rotor also improves compared with the classical prediction, but remains too low. The conclusion of this part is that the addition of edge forces to Froude's concept improves the performance prediction for rotors significantly, although discrepancies between prediction and measurements remain.

From the literature numerical as well as experimental data are known regarding flows induced by actuator discs, which seem to conflict with Froude's results. Therefore the second part of the work concerns the actuator disc itself, and focuses on the question whether the edge forces are an inherent part of the load, instead of merely an addition to Froude's concept in order to improve the representation of real rotors. A numerical as well as analytical approach has been followed. A non-linear, viscous finite element calculation has been set up for the flow of a two dimensional actuator strip with a smooth load distribution. By increasing the Reynolds number and the steepness of the distribution as far as the numerical method allowed, and by extrapolation of the data the inviscid flow induced by a uniform load is approached. The results of this extrapolation comply with the classical performance prediction. Using the results of our numerical method, most of the mentioned experimental and numerical data from the literature can now be explained. For the remaining data (one numerical and one experimental) this still is impossible.

The analytical approach first proceeds from actuator discs with a smooth load distribution. Illustrated by an exact solution of Wu's actuator disc equation, a relation between the externally applied normal load and a tangential (in-plane) force density has been established. If the thickness of the disc is zero, the order of this force density is too low to yield a contribution to the resultant load. For a non-zero thickness the in-plane force density yields a resultant load. In order to explain the physical origin of this force density, we set up the hypothesis that it is the shear stress required to generate vorticity on streamlines passing the disc, even if the Reynolds number based on the disc radius is infinitely large. For one specific case this has been confirmed; in general the interpretation of the origin is incomplete.

For the disc and strip covered with a uniform load, the flow is singular at the edge. The singularity is a vortex which, in case of steady flow, carries a non-zero edge force. The order of this force is the order of the velocity at the edge. This order is unknown, so the force can be infinitely small. The answer to the question of the existence of edge forces as an inherent part of the load awaits an analytical or numerical study towards the entire flow field, induced by discs or strip with a constant uniform load.

TABLE OF CONTENTS

	page
Summary	i
Table of contents	iii
List of symbols	vi
1. Introduction	1
2. The actuator disc problem	3
2.1 The role of Froude's actuator disc in performance prediction by momentum theory	3
2.2 The classical actuator disc performance compared with theory and experiments	7
2.3 The force field of a real rotor and wing compared with the actuator disc force field	11
2.4 The actuator disc concept extended with edge forces	15
Part I : The representation of a rotor by an actuator disc	19
3. The use of the modified actuator surface concept in the momentum theory	21
3.1 Momentum theory including edge forces	21
3.2 Typical results for the actuator disc representing the ideal wind turbine or propeller	25
3.3 The conservation laws for general non-uniform load distributions	27
4. Experimental verification of the momentum theory including edge forces on a model rotor in hover	29
4.1 The momentum theory for real rotors	29
4.2 The determination of the power	32
4.3 The measuring devices	34
4.4 The elaboration of the measurements	36
4.5 Comparison with momentum theory results	40
4.6 Accuracy of the experiment	41
4.7 Discussion and conclusions	43

Part II: The force and flow field of the actuator surface	47
5. The equation of motion	49
5.1 The equation of motion including the force field term	49
5.2 Definition of the actuator surface force field	52
5.3 Dimension analysis of actuator surface flow	53
6. Numerical analysis of the actuator strip flow	57
6.1. Inviscid calculations	57
6.1.1 The actuator cylinder of Madsen	57
6.1.2 The actuator strip of Lee & Greenberg	59
6.1.3 The actuator strip of Schouten	61
6.2. Viscous calculations	62
6.2.1 The force distribution and the definition of the Reynolds number	62
6.2.2 The computational method	65
6.2.3 Results for $m=17$, $Re \rightarrow \infty$	67
6.2.4 Extrapolation towards infinite m	67
6.2.5 The interpretation of the strip experiment of Lee & Greenberg	70
7. The generation of vorticity by force fields	73
7.1 The force density f in Wu's equation illustrated by an exact solution	73
7.2 The smooth actuator surface force field	80
8. The edge singularity of an actuator surface with a constant normal load	84
8.1 A discrete vortex as edge singularity	84
8.2 The possible existence of edge forces	89
8.3 The comparison with other solutions	91
8.3.1 The spiral solution of Schmidt & Sparenberg	91
8.3.2 Greenberg's square root singularity	93

9. Discussion on the results; conclusions	97
9.1 Survey of the results	97
9.1.1 Part I: the rotor problem	97
9.1.2 Part II: the actuator surface problem	99
9.2 Discussion on the results	103
9.3 Conclusions	106

References	108
-------------------	------------

Appendices

A: Sparenberg's translation theorem	113
B: The exponential spiral with infinite length as the limit of a finite length spiral	115
C: The viscous solution of the flow induced by a half-infinite, infinitely thin actuator strip	123
D: The force on a 2-D discrete vortex obtained by an actuator strip limit	125
E: Justification of the experiment	127
F: The boundary layer flow for infinite Reynolds number	131

Samenvatting	135
---------------------	------------

Nawoord	137
----------------	------------

Curriculum vitae	138
-------------------------	------------

List of symbols

a	distance	m
A	area	m^2
b	length	m
c	constant	—
C	dimensionless coefficient	—
\underline{e}	unit vector	—
\underline{f}	force density vector	N/m^3
\underline{F}	surface force vector	N/m^2
$\underline{\hat{F}}$	line force vector	N/m
G	integration volume	m^3
h	scale factor	
H	Bernoulli constant	N/m^2
l	length	m
m	mass of fluid passing a surface per second	kg/s
n	normal coordinate	m
p	pressure	N/m^2
P	force density potential	N/m^2
	power	W
Q	torque	Nm
r	local radius or radial coordinate	m
R	radius of rotor or actuator disc	m
Re	Reynolds number	—
s	streamwise coordinate	m

S	surface	m^2
t	time	s
t	complex number	—
T	thrust of rotor	N
U	parallel flow	m/s
u	components of velocity v in x, y, z direction	m/s
v		
w		
\underline{v}	velocity vector	m/s
x	components of position vector \underline{x}	m
y		
z		
z	complex number	—
α	angle	rad
γ	vortex sheet strength	m/s
Γ	vortex strength	m^2/s
ϵ	thickness of a surface	m
η	imaginary part of ζ	m
ζ	complex number	—
Θ	polar angle in 2-D system	rad
μ	dynamic viscosity	kg/ms
ν	kinematic viscosity	m^2/s
ξ	real part of ζ	m
ρ	density	kg/m^3
	radius in the complex ζ plane	m
φ	azimuth angle in 3-D system	rad
	polar angle in the complex ζ plane	rad

ϕ	velocity potential	m^2/s
χ	complex potential	
ψ	stream function in two dimensional flow	m^2/s
	stream function in three dimensional flow	m^3/s
ω	vorticity	$1/\text{s}$
Ω	angular velocity	$1/\text{s}$

Indices

ax	axial component
d	position at the rotor or actuator disc
ext	externally applied
i	induced quantity
n	normal component
o	undisturbed flow state
P	power
s	streamwise component
t	total, in relation with pressure
T	thrust
work	component doing work
x	component in x-direction
y	component in y-direction
ΔH	component related to a jump in H
$\perp\psi$	component normal to the stream tube
w	fully developed wake state

Chapter 1

INTRODUCTION

The subject of this thesis is the classical actuator disc in axial flow. It is the oldest mathematical representation of a propeller or wind turbine in fluid dynamic calculations. The concept was introduced by R. E. Froude¹ [1889] one century ago, as a continuation of the work of Rankine [1865] on the momentum theory for propellers. Froude's actuator disc is still used as an easy qualitative diagnostic model, and any textbook on rotary wing aerodynamics starts with it. Its importance in performance prediction for propellers and helicopter rotors is nowadays small, but this is different in wind turbine performance prediction. Almost any currently used method is based on Froude's actuator disc concept, despite experimental and numerical evidence that this application displays systematic shortcomings. The application of wind energy in the last decades generated a renewed interest in the actuator disc. This interest stems not primarily from an academic point of view, but is stimulated by the need for cheap, reliable performance prediction methods.

The prediction of the performance of the actuator disc is based on the momentum theory as developed by Rankine and Froude. Often this momentum theory is considered to be the source of the discrepancies mentioned before between prediction and measurement. The present research investigates the limitations of the actuator disc concept itself. Chapter 2 poses the problem, illustrated by numerical and experimental results found in literature. An extension of Froude's concept is proposed by the addition of edge forces.

The improvement of the performance prediction of rotors by using a momentum theory accounting for these edge forces is the subject of part I. Chapter 3 presents this modified momentum theory. Chapter 4 describes an experiment on a model rotor in

¹The initials are mentioned here to distinguish R. E. Froude from W. Froude. Subsequent references to Froude always apply to R. E. Froude, so the initials will be omitted.

hover and investigates the ability of this momentum theory to predict the performance of a real rotor.

Part II has a different character. It treats the actuator disc and strip flow from the fluid dynamic point of view. Since the actuator disc is represented by a force field, and the flow induced by this force field is characterized by the shedding of vorticity, the main question is how to model the generation of vorticity by force fields in an ideal fluid. The appropriate equation of motion describing the relation between the action of force fields and the generation of vorticity is discussed in Chapter 5. Chapter 6 then proceeds with a numerical approach of the problem by discussing numerical results from literature, and by presenting our own calculations on an actuator strip. Chapters 7 and 8 deal with an analytical approach. In Chapter 7 the generation of vorticity by smooth force fields is discussed, and illustrated by two examples of flows in which vorticity is generated by force fields. Chapter 8 treats the problem of a force field which is discontinuous at the edge. This discontinuity induces a flow singularity at the edge. The type of this singularity is determined, and is compared with other solutions known from the literature.

The final Chapter 9 summarizes the results of both parts, and discusses some unresolved problems. An important one is the question whether the actuator disc concept including edge forces is merely an improved representation of a real rotor (the approach of part I) or is dictated by the flow equations as treated in part II.

Chapters 2 and 9 may be read together, without detailed knowledge of the chapters in-between. These chapters contain the statement of the problem (Chapter 2) and a comprehensive survey and discussion of the results (Chapter 9).

Parts of the work described in this thesis combined with related work have been reported at several wind energy and rotorcraft conferences. The corresponding papers can be considered as progress reports in Dutch (van Kuik [1985a, 1985b, 1988]) and English (van Kuik [1986, 1987, 1989a, 1989b])

Chapter 2

THE ACTUATOR DISC PROBLEM

The origin of the present research is to be found in the unsatisfactory accuracy of performance prediction methods based on Froude's actuator disc concept. Experiments on rotors as well as on two-dimensional actuator strips reported in the literature are discussed. The differences between the measured performance and the performance prediction based on Froude's results suggest an extension of Froude's concept by the addition of edge forces in order to improve the prediction. The critical evaluation of this extension is the subject of the following chapters.

2.1. The role of Froude's actuator disc in performance prediction by momentum theory

The concept of the actuator disc was established by Froude [1889], after Rankine [1865] had introduced the use of momentum theory. The striking result of Froude's analysis was that the increase or decrease of the velocity at the disc amounts to

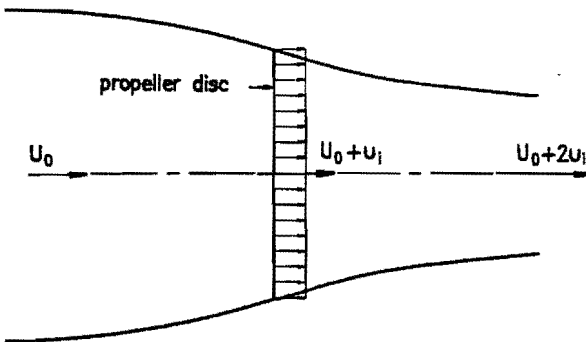


Figure 2.1. Froude's actuator disc concept.

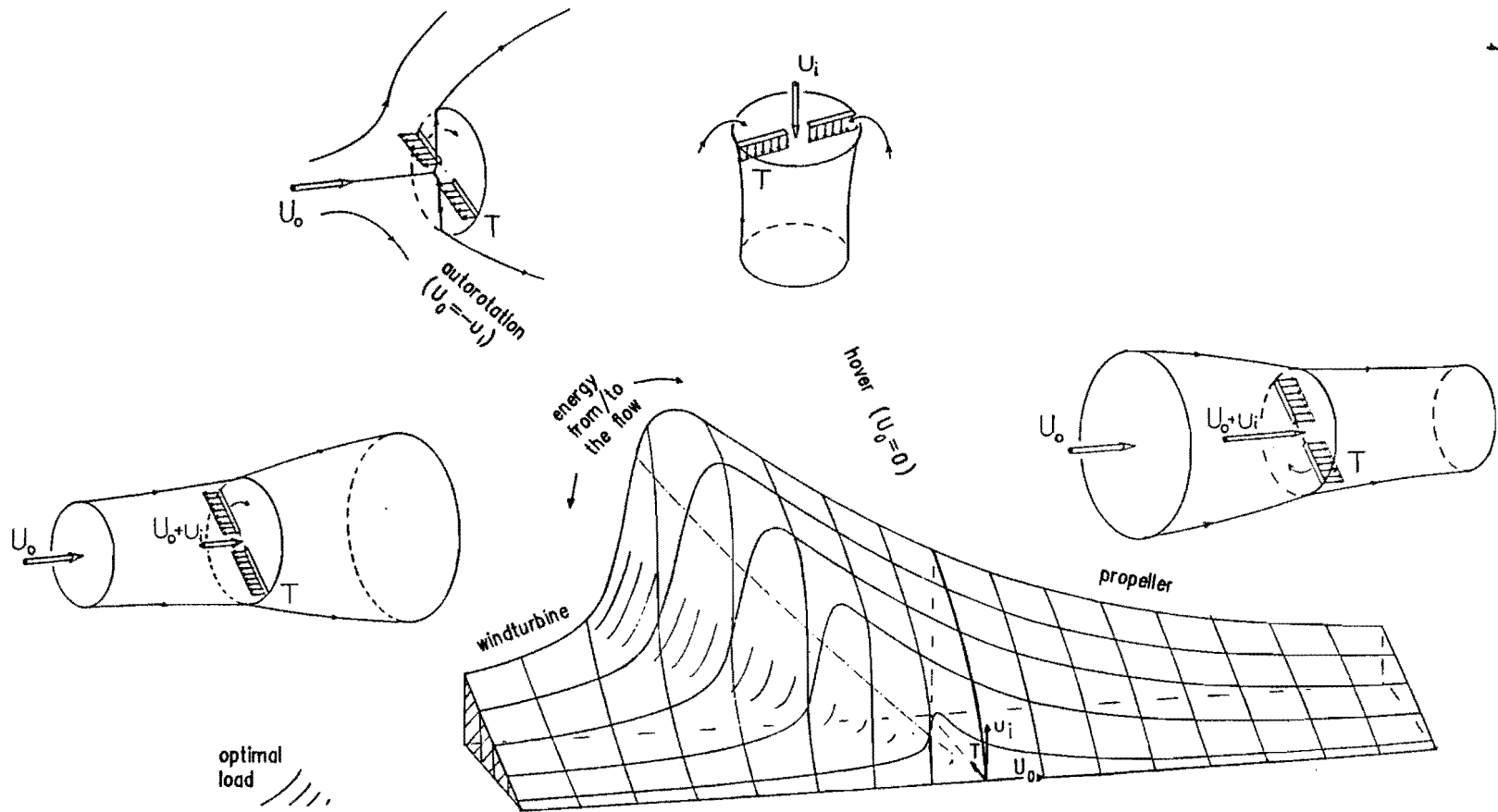


Figure 2.2. A survey of all axial flow states of a rotor: the induced velocity at the rotor disc (u_i) as a function of the thrust (T) and undisturbed wind speed (U_0). A negative sign of U_0 indicates that its direction is opposite to the direction of the thrust T .

exactly half the increase or decrease of the velocity in the ultimate slipstream. Lanchester [1915] was the first to predict the performance in two typical actuator disc flow states: the disc in hover and the disc extracting the maximum amount of energy from the flow. This maximum is usually called the Betz-maximum, after Betz [1920]: only recently Bergey [1979] called attention to Lanchester's publication. Lanchester's results are still considered to describe the ideal performance of a wind turbine and a helicopter rotor in hover.

Owing to its simplicity the actuator disc momentum theory plays a prominent role in current performance prediction methods for wind turbine applications. Unfortunately this application calls for the highest accuracy of the momentum theory compared with propeller and helicopter rotor applications. Figure 2.2 presents schematically the performance of all rotors in axial flow. The velocity disturbance at the disc u_i is shown as a function of the thrust T and the undisturbed velocity U_o . The curves with $T = \text{constant}$ are congruent: a dimension analysis shows that the dimensionless quantities $U_o/\sqrt{T/(\rho\pi R^2)}$ and $u_i/\sqrt{T/(\rho\pi R^2)}$ are related uniquely. Using these dimensionless velocity scales, the 3-D surface of figure 2.2 becomes the 2-D figure 2.4, where the scales are defined quantitatively. In figure 2.2 u_i and T have the same direction; a negative sign of U_o indicates that the thrust acts against the undisturbed wind speed. The average velocity through the rotor is $\bar{u}_d = U_o + u_i$. For $\bar{u} > 0$ this velocity has the same direction as the thrust, so the rotor puts energy into the flow. For $\bar{u} < 0$ energy is taken from the flow.

In all performance prediction methods, u_i is very important: once u_i is known, the performance is known. It depends non-linearly on T and U_o , and especially for heavily loaded wind turbines (high T , low U_o) any small variation of U_o or T induces large variations of u_i . This implies that the model for predicting u_i has to be very accurate: any small inaccuracy in the relation between U_o , T and u_i may cause large differences between prediction and measurement.

An essential extension of the actuator disc momentum theory has been given by Glauert [1935]. In this publication Glauert includes the results of many other investigators, particularly Drzewiecki [1892] and Prandtl [1919]. In order to distinguish Glauert's momentum theory from the actuator disc momentum theory, it is called the blade-element momentum theory. The main features are:

- Glauert assumes that each annulus of the disc can be considered as an actuator "annulus", independent of its neighbouring annuli (figure 2.3).
- According to Drzewiecki [1892] the thrust within each annulus is assumed to be

exerted by the blade elements within the considered annulus. The load on the blade elements depends on the local velocity. Drzewiecki assumes that this velocity is built up from the undisturbed wind speed U_0 and the rotational velocity Ωr . Glauert accounts for the de- or acceleration of the flow by using momentum theory. Both consider each element to be independent from its adjacent elements.

- For a given blade-element load the classical momentum theory applied to the annulus provides the velocity in the annulus at the rotor. However, this velocity has to be known in order to determine the load on the element, using two-dimensional aerofoil data. Usually an iterative procedure is necessary to determine the load and the velocity together.
- Froude's result of the induced velocity being half the induced velocity in the fully developed wake is used in each element without any modification. The effect of the finite number of blades is accounted for by a tip correction factor developed by Prandtl [1919]. This correction factor influences the elements near the blade tip. It decreases the load and consequently the resulting velocity at the element, but Froude's result remains unaffected. No correction is applied for the finite aspect ratio of the blades.

Since Glauert the blade-element momentum theory has remained unchanged essentially. Adapted for modern numerical treatment, the method has been actualized by Wilson, Lissaman & Walker [1976]. Their method is the current performance prediction method in wind turbine design. In the next section we will show that the results of this method are far from satisfying in case of off-design performance prediction. Still there exists hardly any non-empirical research on the improvement of the blade-element momentum theory, except the work done by Viterna & Corrigan [1981]. They proposed to include a new tip-correction factor in the design method: this correction accounts for the aspect ratio of the blade so it is essentially different from Prandtl's tip correction. Especially in the tip region their correction alters the flow field: there the velocity at the rotor is not the average of the velocity far up- and downstream as assumed by Froude. Although this correction cannot be founded in the framework of the classical momentum theory, it provides good results for fast running wind turbines. This suggests that the tip flow requires improved modeling.

Not discussed in this thesis is the development of performance prediction methods based on vortex theory instead of momentum theory. A thorough comparison of these methods can be found in de Vries [1979]. A common feature of many vortex methods is that for computational efficiency the velocity at the rotor disc is assumed to be the average of the upstream and downstream values, which is exactly Froude's result.

Therefore it is not surprising that the results of these vortex methods agree very well with the momentum theory results, which implies that the accuracy is limited. This accuracy is the subject of the next section.

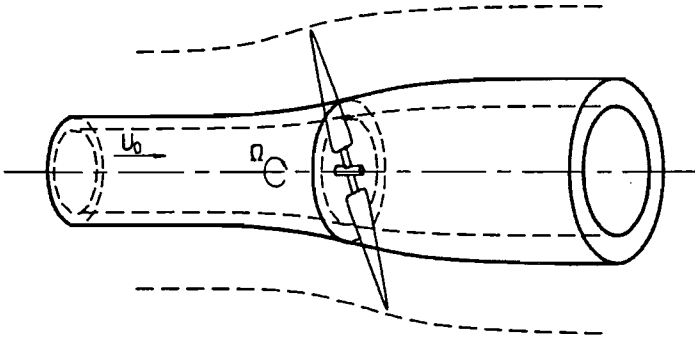


Figure 2.3. The actuator "annulus".

2.2. The momentum theory results compared with theory and experiments

In general, the results obtained by the actuator disc or blade-element momentum method provide food for thought: the agreement with experiments is rather bad (van Bussel & van Kuik, [1985]). For a specific wind turbine the performance can be calculated reasonably as far as the power is concerned, but the thrust prediction is not satisfactory. In off-design conditions the calculated power as well as the thrust are far from the measured data. The thrust is underestimated systematically. Furthermore Stoddard [1977] reports measured values of the thrust which exceed the theoretical upper limit as predicted by the momentum theory by 20% to 50%.

Figure 2.4 (on page 8) is a dimensionless presentation of figure 2.2, and shows the usual way of presenting the actuator disc performance. For a constant thrust T , the induced velocity at the disc u_i is given as a function of the undisturbed wind velocity U_0 . Both velocities have been made non-dimensional by $\sqrt{T/2\rho A}$ which is the induced velocity at the rotor according to the classical momentum theory in case of hover, with A being the rotor area and ρ the fluid density. Also we show the combination of two

compilations of experiments on real rotors, obtained by Stoddard [1977] and Johnson [1980]. For the propeller flow the momentum theory underestimates the induced velocity, while for the wind turbine flow this is overestimated. As the induced velocity has a different sign in both flow regimes, the total velocity at the disc $u_d = U_0 + u_i$ is underestimated in all flow states: the mass flow through the rotor is always higher than predicted by the classical momentum theory. The right hand side of figure 2.4, the propeller regime, is well known in helicopter literature, as is the left-hand side in wind turbine literature. The combination of both in one figure is not usual, so the systematic deviation has not been noticed before.

Hütter [1977] has investigated this increased mass flow through the rotor in case of wind turbines. He observed that the performance exceeds the Lanchester-Betz maximum by 4% to 13%. As an explanation he suggests that turbulent mixing of the

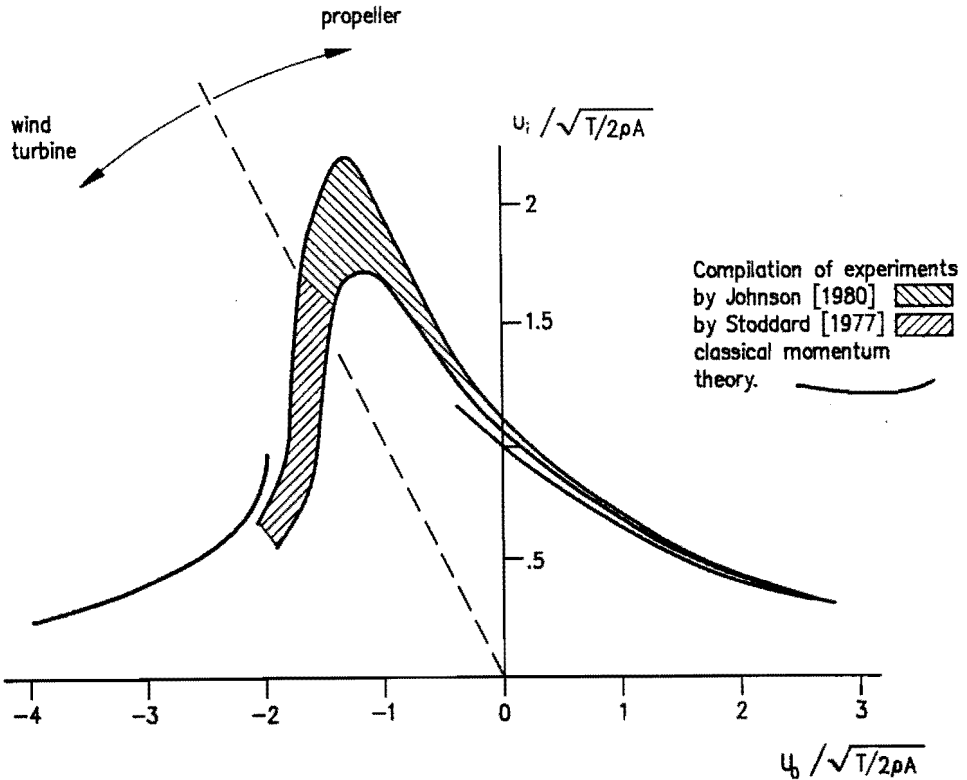


Figure 2.4. The systematic deviation of experimental rotor results from classical momentum theory results.

wake flow with the flow adjacent to the wake generates an increased momentum of the wake, by which the average velocity and the performance increase. However this explanation cannot be valid for a helicopter rotor in hover or for propellers. In the hover case the flow outside the wake has an opposite direction compared with the wake flow itself, see figure 2.2, so turbulent mixing only lowers the wake velocity. The same is true for the propeller flow: the velocity outside the wake is smaller than the wake velocity, so mixing has a decelerating effect on the wake flow.

From the literature two actuator strip experiments are known, which show the same deviations from the classical momentum theory. Lee & Greenberg [1984] performed a two-dimensional experiment in a shallow water tank (shallow enough to ignore the third dimension): they simulated a line momentum source by an array of closely spaced nozzles, injecting high-velocity, turbulent, incompressible jets into the flow. By rapid mixing of the jets, and tuning of the jet flow in order to have a negligible mass injection combined with a high momentum, this arrangement is meant to simulate an actuator strip with constant load. The ambient velocity was zero, so the hover result should be obtained. The classical theory predicts a value 0.5 for the ratio of average velocity at the strip to average velocity in the far field. Measured at the nozzle outlet line, the experimental ratio varies from ≈ 0.46 to ≈ 0.55 , depending on the number of nozzles, flow rate, etc., and on the jet Reynolds number. The highest Reynolds number, which yields the best approximation of inviscid flow, gives the ratio 0.55. We have obtained these data by integration of the measured velocity distribution given by Lee & Greenberg¹. In this integration, the mass flow near the edge (approximately 10% of the strip length) is assumed to be zero. The possibility of reversed flow and the uncertainty where to assume the actual strip position, see section 6.2.5, prohibit a clear interpretation of these experimental results with respect to a deviation from Froude's results. The only mechanism which can increase the average velocity at the strip beyond the value predicted by the momentum theory is turbulent mixing of the wake flow with the outer flow. However, as discussed before in this section, this is possible only in flows which have a decelerating wake. Therefore no explanation for the exceeding of Froude's factor 0.5 is available, except for possible experimental inaccuracies.

Castro [1971] reports an experiment on a wire gauze placed in a wind tunnel from wall to wall. Such a gauze decelerates the flow passing through it more or less uniformly,

¹ This distribution is shown in figure 6.15.

and represents the "wind turbine" actuator disc. The ratio of screen area to windtunnel cross section area was 0.045, so there is little fear for blockage effects. Castro observed that the gauze started to act as a solid plate at a thrust coefficient $C_T = \frac{2T}{\rho U^2 A}$ above 1.2, where T denotes the thrust, A the screen area, U the undisturbed velocity and ρ the fluid density. Below $C_T = 1.2$ there was a clearly defined wake flow with a vortex sheet separating the wake from the outer flow. Above $C_T = 1.2$ the flow behind the disc was stagnant accompanied by unsteady vortex shedding. The classical actuator disc theory expects this to occur at $C_T = 1.0$, as then all kinetic energy of the flow passing the disc should be absorbed by the disc.

The effect of turbulent mixing in the wake cannot clarify this deviation. According to Hütter [1977] this effect can increase the average velocity through a wind turbine 4% to 13%. The boundary of the wake of a wind turbine consists of spiraling tip vortices which enable a larger amount of turbulent mixing than a smooth vortex sheet does as present in Castro's experiment. Therefore this mixing cannot clarify Castro's results.

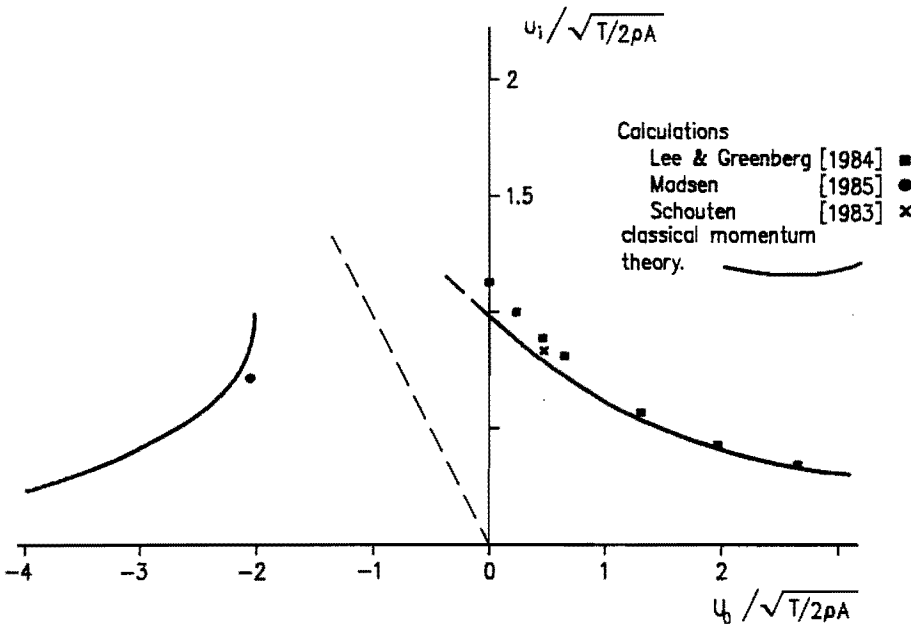


Figure 2.5. Comparison of classical momentum theory with non-linear numerical methods.

The conclusion we can draw from this survey of experimental results is that the velocity at the rotor disc or at the gauze is systematically higher than predicted by Froude's result. Therefore it is obvious to compare Froude's concept of the actuator disc with a disc concept which accounts for such an increased velocity: the disc with edge forces. This actuator disc concept has been developed for rotors making use of concentrators like shrouds or tipvanes. These devices increase the flow through the rotor in an artificial way. The present analysis suggests a natural concentration effect to be present by which an extension of Froude's concept with edge forces seems appropriate. In the following sections we will give this extension a more solid basis.

Besides the experimental data, also numerical data exists which show a discrepancy with momentum theory results. For completeness they are shown in this section in figure 2.5. Lee & Greenberg [1984] report results of a 2-D actuator strip flow field calculation. Schouten [1983] also performed an actuator strip flow field calculation, using a similar model. Madsen [1985] performed a calculation on a heavily loaded actuator cylinder: it represents the cross-section with the horizontal plane of a vertical axis Darrieus wind turbine. The methods are discussed in Chapter 6, the results are shown in figure 2.5.: all show the same deviation from momentum theory results. All data are obtained by 2-D calculations. Greenberg [1972] published 3-D results, which show exactly the same deviation.

2.3. The force field of a real rotor and wing compared with the actuator disc force field

In the present work, the actuator disc is defined as a permeable surface on which force densities are distributed. This distribution induces a pressure jump across the disc, without any jump in the velocity. Would the actuator disc concept have any physical background, then it should be the result of the force field of a real rotor subjected to a sequence of limits:

- the thickness and chord length of the blades vanish to zero, so the blades become lifting lines
- the number of lifting lines increases to infinity, while at the same time the bound vorticity of each line goes to zero; the torque produced by the load on the lifting

lines is kept constant in this limit; the rotor has become a permeable disc covered with bound vorticity

- the angular speed of this disc increases to infinity, keeping the converted power constant and decreasing the torque by means of decreasing the strength of the vorticity; then the angular momentum of the wake vanishes, and only axial and radial flow velocities remain.

In this thesis we do not work out the mathematical description of this sequence of limits, but restrict ourselves to a comparison of the force field of a rotor blade with the actuator disc force field. We will show that an important physical feature of Froude's actuator disc theory is not valid in case of a real rotor flow. In Froude's disc model the entire axial load performs work: the load connected to the change of axial momentum is the same as the load converting power.

Figure 2.6 shows a possible rotor configuration. The blade is assumed to be a thin, flat plate having zero pitch angle (the leading and trailing edge follow the same path). This assumption will be discussed later on. The blade is a lifting surface covered with a distribution of spanwise and chordwise bound vorticity as shown schematically in the

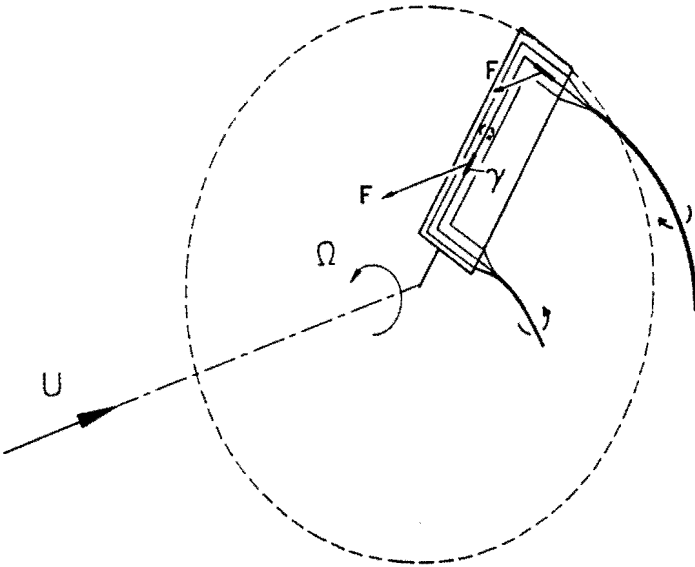


Figure 2.6. The axial force on the bound vorticity of a rotor blade.

figure. This vorticity continues as free vorticity in the wake and rolls up into a strong tip vortex and a weak root vortex. If the velocity component perpendicular to the bound vorticity is non-zero, a force acts on this vorticity. It is perpendicular to the vorticity, so the force on the chordwise vorticity has only radial and axial components. It cannot contribute to the torque, so it cannot perform work. On the other hand it contributes to the axial thrust, as the chordwise bound vorticity experiences non-zero spanwise (radial) velocities.

The direction of the force \underline{F} on the vorticity depends on the local relative velocity \underline{v} and the vorticity strength $\underline{\gamma}$ by $\underline{F} = -\rho \underline{v} \times \underline{\gamma}$. The sign of $\underline{\gamma}$ is as shown in the figure. The chordwise vorticity is concentrated near the tip, where it manifests itself as the tip vortex. The average spanwise velocity experienced by the chordwise bound vorticity is the average of the spanwise velocity on the suction and pressure side of the tip. This average velocity at the tip is directed inboard, resulting in an initially inboard displacement of the tip vortex. In other words, the radial velocity at the tip is always directed towards the axis, so only the sign of the chordwise vorticity determines the sign of the axial force on this vorticity. However, the sign of the spanwise and chordwise vorticity are related uniquely. As a consequence, the orientation of the force on the spanwise and chordwise bound vorticity is always identical, irrespective of the sign of the vorticity: the tip load always increases the total load.

This conclusion is a guideline for improving the actuator disc model. Artificially concentrated rotor flows (by tipvanes or shrouds) show exactly the same property: the load on the shroud or tipvane does not perform work, but contributes to the total load acting upon the flow (van Holten [1981]). This leads to an increased velocity at the rotor disc (increased with respect to Froude's prediction). In the previous section, such an increased velocity was indeed observed for real rotor flows.

For the rotor blade of figure 2.6, the previous argumentation is straightforward. It is limited only by the assumption of a zero pitch angle. If the pitch angle is non-zero, the chordwise bound vorticity contains an axial component. The force on this component contributes to the torque, so does perform work by which the previous analysis becomes more complicated. However, this assumption does not alter the determination of this qualitative difference between a blade load and Froude's actuator disc load. Furthermore, the rotor with zero pitch angle is a realistic one: if the angular speed is sufficiently high, attached flow is obtained and the rotor acts as a wind turbine.

The load due to chordwise bound vorticity is not a purely mathematical phenomenon. It is well known on wings with a small aspect ratio but is also noticeable for moderate

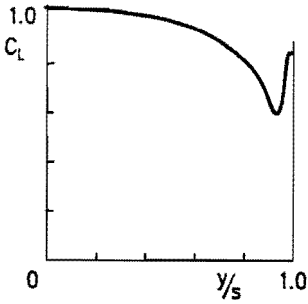


Figure 2.7a

The tip load on the chordwise bound vorticity of a wing (a) with aspect ratio $b/c = 6$, and a rotor blade (b) with aspect ratio $R/c = 4.8$.

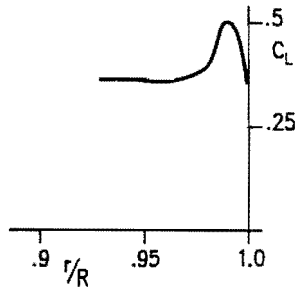


Figure 2.7b

aspect ratio's. Küchemann [1978] shows a measured load distribution of a wing with aspect ratio 6, figure 2.7a: the tip load is clearly recognized. Figure 2.7b shows the measured load on a blade tip of a model rotor in hover, reported by Gray and co-workers [1980]. Again a tip load is present, which supports the previous analysis.

The 2-D equivalent of the actuator disc is the actuator strip. Mathematically it is a distribution of force densities on a 2-D area. Usually it is assumed to be infinitely thin, by which it becomes a line. We explain the physical origin by a similar sequence of limits as was used for the disc at the beginning of this section. Starting from a cascade of finite span wings travelling behind each other, the thickness and chord of each wing are assumed to vanish, meanwhile maintaining the same resultant load. Then the number of wings (which have become lifting lines) is increased to infinity while the vorticity strength and the load on each line are decreased. This is done in such a way that the resulting force in travelling direction per unit of length of the cascade remains constant. Finally the speed of the vortex sheet, which is the result of this transition, is increased to infinity, keeping the converted power constant by diminishing the strength of and the load on the vortex sheet. Then the velocities induced in travelling direction become zero, and the flow has become two dimensional in each plane perpendicular to this direction. The remainder of the original wing load is the distribution of a force field on a slit in the 2-D plane: the actuator strip.

It is clear that the analysis regarding disc loads increasing momentum but not doing work, is valid for wing loads as well: assume a flat-plate wing, travelling in its own plane in an oblique parallel flow. The force on the (tip) chordwise vorticity contributes to the normal force, so to the change of downward momentum of the flow. It does not

contribute to the force in travelling direction. Consequently it does not contribute to the work done by the wing.

The results of this section show that the tip flow and tip load are not modeled satisfactorily in Froude's concept of the actuator disc. In the previous section we showed that Froude's prediction of the velocity through the rotor is too low in all rotor flow states. The subject of the remaining chapters is to investigate the relation between both observations. This problem is not new at all: Lanchester was the first to discuss this as is clear from the next section. However, our proposed extension of Froude's concept is new: the addition of edge forces improves both the prediction of the velocity through the rotor as well as the representation of the rotor blade tip load.

2.4. The actuator disc concept extended with edge forces

Lanchester [1915] was aware of some shortcomings of the actuator disc concept. In his article he discusses this concept proposed by Froude. Although he finally agrees with this concept, he clearly defines the weak points as may be seen from the following two quotations:

Page 103:

"We may conceive the actuator as defined by a circle, whose center is situated on the line of thrust and whose plane is normal to the direction of motion. There is no real need that the boundary of the imaginary plane constituting the "actuator" should be circular, but it is better to think of some definite form; also it is tacitly understood that the actuator is a hypothetical simplification, and as such is a stepping-stone to the study of the screw propeller.

Speaking academically, the weak point of the whole conception is that there is no proof offered that either the work done (i.e., energy expended) or the momentum communicated, is strictly confined to the column of fluid passing through the actuator, and there is, in fact, nothing to restrict or confine the fluid as in the case of efflux theory, by which the problem is rendered really definite. It is, as I understand it, quite candidly admitted by Mr. Froude that the regime contemplated by his theory is not capable of exact expression. This, however, is no obstacle to the application of any theory in real hydrodynamics; if it were necessary for the

engineer to await the pleasure of the pure mathematician in these matters, the subject would have made scarcely perceptible progress since the time of Noah. In such a case as the present, if the method of treatment contains 80 per cent. or 90 per cent. of truth, it may demand acceptance."

Page 108/109:

"Having said this much, the writer would like to add that there remain many difficulties in the theory of Mr. Froude's actuator of a detail kind. The admitted difficulty relating to the edge of the actuator is probably more apparent than real; it is mainly due to attempting to juggle with infinities. Thus the actuator is supposed to be of zero thickness; it is, in fact, a surface. In spite of this it is presumed to impart a uniform degree of acceleration to the fluid right up to its edge. Now, at the edge it is manifestly impossible to maintain any finite pressure difference between the front and rear faces; hence, even if the actuator have infinitesimal thickness in its central part, it must run to a finite thickness at the edge; or, if it is finite in the middle, its thickness must become infinite at the edge. Obviously, with the conditions given, difficulties of regime are bound to arise: the rate of communication of acceleration (if one really must visualize the scheme in detail) requires to fade away at the edges of the actuator, and the vortex sheet will become a stratum containing rotation.

As a matter of fact, the difficulties largely disappear, and at the same time we more nearly approach the conditions of practice, if we modify the original conception in the manner already indicated — namely, if we substitute an intermittently operating actuator for the continuously operating version, and substitute for the uniformly moving slip stream a wake consisting of a series of vortex rings. The action of an impulse distributed uniformly over an area of circular form is well understood; it gives rise to a vortex ring, the stream lines of which have been ascertained by the unimpeachable methods of mathematical analysis. However, as in the case of Mr. Froude's device, there is the same little difficulty relating to the edge of the area over which the impulse is given, we have to suppose in rigid theory that the impulse region is cut off at its periphery by a filament or core of some kind. Strictly speaking, there must be a boundary surface rendering the region one of double connectivity. This difficulty is overcome in reality by the fact that (just as in the preceding discussion) the edge of the actuator becomes the seat of rotation and the vortex motion proper is built up around the core so produced.

Now it may be at once observed, as already stated, that the conditions proper to the original Froude actuator no longer apply; a considerable proportion of the energy representing the work done by the actuator is in the outer portions of the vortex rings emitted, only a part of the energy, in fact, remains in the fluid whose rearward momentum represents the thrust reaction. Thus, in our fundamental equation, we have: ²

$$\begin{aligned} \text{Work done per second greater than} & \quad \frac{m (U_o^2 - u_w^2)}{2} \\ \text{and momentum per second as before,} & \quad m (U_o - u_w) \\ \text{and velocity } u, \text{ where force acts} & \quad > \frac{U_o^2 - u_w^2}{2 (U_o - u_w)} \\ \text{or} & \quad > \frac{U_o + u_w}{2}. \quad " \end{aligned}$$

Lanchester's prediction for the 'intermittently operating actuator' agrees qualitatively with the performance of rotors, figure 2.4, with the numerical results for actuator strips, figure 2.5, and with the results of the strip experiments of Lee & Greenberg [1984] and Castro [1971]. The determination of an invalid assumption in the momentum theory applied to rotors (previous section: not the entire thrust but only a part of it contributes to the conversion of power), the systematic deviation of experimental results from the classical prediction (section 2.2), and Lanchester's considerations suggest an extension of Froude's actuator disc concept by edge forces. The momentum theory based on this concept has been developed for rotors with shrouds or tipvanes. These devices increase the mass flow through the rotor in an artificial way: figure 2.4 gives rise to think of a natural concentrator effect to be present. The momentum theory for discs with edge forces meets the considerations mentioned above. Therefore the starting point for the following chapters is the actuator disc with edge forces.

² Notations according to figure 2.8; m denotes the mass of fluid passing the disc per second, according to Froude's hypothesis.

Figures 2.8 and 2.9 show the differences between the Froude's actuator disc concept, and the one including edge forces. The improvement of the performance prediction for rotors using this extended concept is investigated in Part I, by discussing the actuator disc momentum theory accounting for the edge forces (Chapter 3) and by performing an experiment on a model rotor in hover and trying to interpret the results with this momentum theory. Part II analyses the force and flow field of actuator discs and strips, as the previous line of thoughts raises the question whether Froude's concept is correct in representing the edge flow. This investigation is done by a numerical as well as an analytical approach (Chapter 6 and 7/8 respectively) after having established the appropriate equation of motion (Chapter 5).

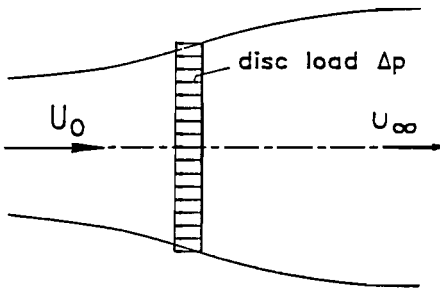


Figure 2.8. The classical actuator disc concept.

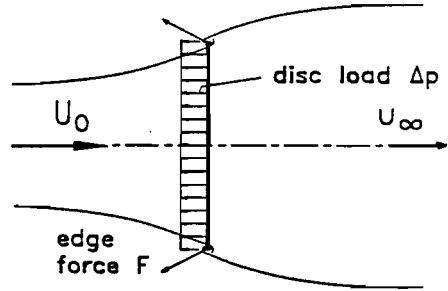


Figure 2.9. The concept including edge forces.

Part I : The representation of a rotor by an actuator disc

Chapter 3

THE USE OF THE ACTUATOR SURFACE WITH EDGE FORCES IN THE AXIAL MOMENTUM THEORY

The axial momentum theory and the actuator disc or strip are closely coupled in the context of performance prediction. The adjective axial denotes that only the change of momentum in the direction of the normal on the surface is considered. The axial momentum theory does not account for changes in angular momentum resulting from the applied torque.

The momentum theory treated here concerns only the actuator strip or disc discussed in section 2.4: a surface covered with a distribution of constant, axial load together with edge forces. The momentum theory which deals with such a force distribution is already available, as it has been developed for augmented rotors (rotors with shrouds or tip vanes) by van Holten [1981]. Therefore only a brief survey is given here.

3.1. Momentum theory including edge forces

The momentum theory including edge forces is not different from Froude's classical theory in applying the conservation laws of mass, momentum and energy, but differs in the assumed force distribution. In the classical theory the total axial force, which of course is balanced by the change of axial momentum of the flow, equals the force doing work; in the present theory, there is a distinction between these terms, as a part of the force distribution is normal to the local flow (so does not perform work) but still has an axial component.

Figure 3.1 shows the stream tube being used as control volume. At the cross section A_0 the flow is supposed to be undisturbed. The cross section A_w is chosen far enough downstream, so that the wake contraction or divergence is completed. The bounding streamlines are the downstream vortex sheets separating the wake from the outer

flow, and the upstream streamlines enclosing the same mass flow. The circumference of the surface is denoted by S : in 3-D this equals $2\pi R$, while in 2-D this becomes $2L$ for a strip of length L in the direction normal to the 2-D plane. So per unit of length the 2-D "circumference" S equals 2. T is introduced as total thrust. In 3-D, the dimensions of T and A are [N] and [m²]; in 2-D the respective dimensions are [N/m] and [m]. The momentum balance reads:

$$T = F_{\Delta H} A_d + \bar{F}_{\perp \Psi, ax} S = \rho u_w (u_w - U_0) A_w, \quad (3-1)$$

where $\bar{F}_{\perp \Psi, ax}$ is the axial component of the edge force, and $F_{\Delta H}$ the normal surface load changing the Bernoulli constant $H = p + 1/2 \rho v \cdot v$. The contribution of the pressure on the boundary of the control volume is zero, as proved by Glauert [1935]. His proof proceeds from a disc placed in a wind tunnel. By drawing the momentum balance for the region between the walls and the streamtube passing through the disc, the limiting condition of a tunnel of a very large radius shows that the contribution of the pressure to this balance vanishes. Since the pressure contributes equally but with a different sign to the momentum balance for the streamtube passing the disc, the pressure term is absent also in the latter balance. Glauert's proof requires no specification of the force field, so it is valid as well for surfaces with edge forces. Consequently the pressure term does not enter the momentum balance (3-1).

On each streamline which passes the actuator surface we apply Bernoulli's law separately upstream and downstream of the surface:

$$F_{\Delta H} = \Delta H = \frac{1}{2} \rho (u_w^2 - U_0^2). \quad (3-2)$$

Equation (3-2) is straightforward for a streamline which passes the actuator surface once. Near the edge the streamlines can have a spiralling shape, by which they pass the surface more than once. However, by continuity considerations it is clear that such streamlines pass the surface one time more in downstream direction than in upstream direction, by which a resultant jump ΔH remains. Streamlines outside the wake have passed the actuator surface not at all or equally in both directions, so do not experience a final change of H . Therefore (3-2) is valid for all streamlines inside the control volume of figure 3.1.

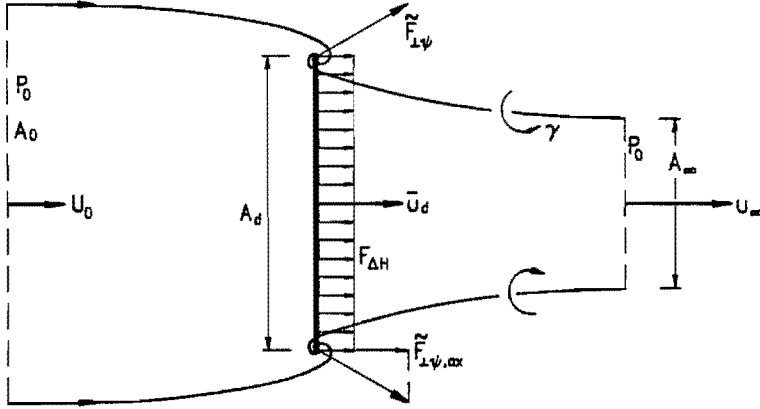


Figure 3.1. The control volume of the momentum theory

The mass balance simply is:

$$\bar{u}_d = u_w \frac{A_w}{A_d} \quad (3-3)$$

The bar above \bar{u}_d denotes that it is the average velocity. Since u_w is constant by (3-2), the average value equals the value on each streamline. The combination of (3-1) to (3-3) with $\bar{F}_{\perp \Psi} = 0$ gives the well-known classical result $\bar{u}_d = \frac{1}{2} (U_0 + u_w)$. The deviation from this classical value is denoted by $\delta \bar{u}_d$, so:

$$\bar{u}_d = \frac{1}{2} (U_0 + u_w) + \delta \bar{u}_d \quad (3-4)$$

With $T_{\Delta H} = F_{\Delta H} A_d$, $T_{\perp \Psi} = \bar{F}_{\perp \Psi, ax} S$ the total thrust is $T = T_{\Delta H} + T_{\perp \Psi}$. By manipulation of (3-1) through (3-4) the "new" term $\delta \bar{u}_d$ appears to be connected to the edge forces:

$$\delta \bar{u}_d = \frac{T_{\perp \Psi}}{\rho A_d} \frac{1}{(u_w - U_0)} = \frac{T_{\perp \Psi}}{T_{\Delta H}} \frac{(u_w + U_0)}{2} \quad (3-5)$$

so:

$$\begin{aligned}\bar{u}_d &= \frac{T}{\rho A_d} \frac{1}{(u_w - U_o)} = T \frac{T}{\Delta H} \frac{(u_w + U_o)}{2} = \\ &= T \frac{T}{\Delta H} \left[\frac{U_o}{2} + \frac{1}{2} \sqrt{U_o^2 + \frac{2T \Delta H}{\rho A_d}} \right].\end{aligned}\quad (3-6)$$

The power is:

$$P = T \Delta H \bar{u}_d. \quad (3-7)$$

The increase of velocity $\delta \bar{u}_d$ is determined by the axial component of the edge force, $\tilde{F}_{\perp \Psi, ax}$, and by the surface load $F_{\Delta H}$. This jump itself is not affected by $\tilde{F}_{\perp \Psi}$: by (3-2) the work done per unit mass of flow remains the same, but the amount of mass is changed by assuming $\tilde{F}_{\perp \Psi} \neq 0$. A positive $\delta \bar{u}_d$ supposes the axial component of $\tilde{F}_{\perp \Psi}$ to have the same direction as $F_{\Delta H}$.

The momentum theory including edge forces does not give a closed solution, since the ratio $T_{\perp \Psi}/T_{\Delta H}$ is still unknown. This ratio cannot be provided by the mass, energy and momentum balance, as it depends on the local velocity distribution near the edge, instead of resultant distributions. On the other hand, suppose the flow field of an actuator surface is known. Then the momentum theory extended with a radial momentum balance, provides the determination of $\tilde{F}_{\perp \Psi}$. This radial balance is very simple in the 2-D flow situation with $U_o = 0$. With the upper half plane of the flow field as control volume, this balance reads:

$$\tilde{F}_{\perp \Psi, rad} = - \int_{-\infty}^{+\infty} (p - p_o) dx_{\text{centerline}}. \quad (3-8)$$

The momentum itself does not enter the balance, as the transport in y -direction is zero: outside the wake at a large distance r , $|v|$ varies as r^{-1} due to the conservation of mass. The momentum vanishes for increasing r as r^{-2} and the momentum transport as r^{-1} . In section 6.1.2 (3-8) is elaborated using the data of the actuator strip calculations of Lee & Greenberg [1984]: indeed a non-zero value of $\tilde{F}_{\perp \Psi}$ is found.

3.2. Typical results for the actuator disc as the ideal wind turbine and propeller

The equations (3-2), (3-6) and (3-7) are sufficient to provide qualitative expressions for the induced velocity and power for the ideal rotor in hover. With $U_0=0$, the velocity at the disc \bar{u}_d equals the induced velocity \bar{u}_i , which is:

$$\bar{u}_d = \sqrt{\frac{T_{\Delta H}}{2\rho A_d} \frac{T}{T_{\Delta H}}} = \left[\bar{u}_d \right]_{\text{classical theory}} \frac{T}{T_{\Delta H}} \quad (3-9)$$

The power is:

$$P = \sqrt{\frac{T^2 T_{\Delta H}}{2\rho A_d}} = \sqrt{\frac{T_{\Delta H}^3}{2\rho A_d} \frac{T}{T_{\Delta H}}} = \left[P \right]_{\text{classical theory}} \frac{T}{T_{\Delta H}} \quad (3-10)$$

In (3-9) and (3-10) the classical expressions are related to $T_{\Delta H}$. This seems quite arbitrary as $T = T_{\Delta H}$ in the classical theory. However, the notation used in (3-9) and (3-10) expresses most clearly the change of the induced power and velocity if $T_{\perp\Psi}$ is increased while $T_{\Delta H}$ is constant. This is what happens when a rotor without edge forces having a certain $T = T_{\Delta H}$, is provided with edge forces. The notation 'classical theory' then refers to the situation without edge forces, and is independent of the change of total thrust. If the classical expressions were related to T instead of $T_{\Delta H}$ the values of $[]_{\text{classical theory}}$ were not independent of the increase of T , so could not be used as reference values.

The factor $T/T_{\Delta H}$ determines the shift of the results compared to the classical predictions: an increase of mass flow and of converted power. The same is true for the actuator disc as the ideal windturbine. It is convenient to express the results in dimensionless coefficients:

$$\left. \begin{aligned} C_P &= \frac{|P|}{\frac{1}{2}\rho U_o^2 A_d} \\ C_T &= \frac{|T|}{\frac{1}{2}\rho U_o^2 A_d} \\ C_{T\Delta H} &= \frac{|F_{\Delta H}|}{\frac{1}{2}\rho U_o^2} \end{aligned} \right\} \quad (3-11)$$

Substitution of (3-1), (3-2), (3-6) and (3-7) gives:

$$\left. \begin{aligned} \frac{\bar{u}_d}{U_o} &= \frac{1}{2} \left[1 + \sqrt{1 - C_{T\Delta H}} \right] \frac{C_T}{C_{T\Delta H}} \\ C_T &= C_{T\Delta H} + C_{T_{\perp\Psi,ax}} \\ C_P &= \frac{1}{2} \left[1 + \sqrt{1 - C_{T\Delta H}} \right] C_T \end{aligned} \right\} \quad (3-12)$$

The classical results are recovered by equating $C_{T,\Delta H}$ to C_T . If $C_{T,\Delta H}$ is considered as an independent variable, the (yet unknown) relation between C_T and $C_{T,\Delta H}$ provides C_T . $C_{T,\Delta H}$ is a measure of the amount of extracted kinetic energy per unit of mass: as in the classical theory, $C_{T,\Delta H} = 1$ is the maximum value since $u_o = 0$ in that case. This results in $C_{T,\max} > 1$. A first estimate of the maximum C_P is obtained by assuming $C_{T,\Delta H}/C_T$ to be approximately constant. Then C_P is written as:

$$C_P = \frac{1}{2} \left[1 + \sqrt{1 - C_{T\Delta H}} \right] C_{T\Delta H} \frac{C_T}{C_{T\Delta H}}, \quad (3-13)$$

which yields:

$$C_{P_{\max}} \approx \frac{16}{27} \frac{C_T}{C_{T\Delta H}} = \left[C_{P_{\max}} \right]_{\text{classical theory}} \frac{C_T}{C_{T\Delta H}} \quad (3-14)$$

Apparently not only the maximum thrust but also the maximum power output is increased compared to the classical prediction. In the windturbine state, the efficiency of the actuator disc is increased; the opposite is true for the disc in the propeller state: the power needed to establish a certain thrust is higher than classically predicted. In both cases this is due to the increased mass flow through the disc.

The result is that the momentum theory including edge forces indeed predicts a shift of the performance diagram (figures 2.4 and 2.5) towards the observed experimental and numerical values. A prerequisite to this conclusion is that $\underline{F}_{\Delta H}$ and $\underline{\tilde{F}}_{\perp \psi, ax}$ have the same orientation. The physical origin of the edge force is found in forces at the blade tips (section 2.3). The axial component of the edge force then represents the lift force at the chordwise bound vorticity. This extra contribution to the lift on the blade always increases the total lift or, in rotor terms, the total thrust.

A quantitative result cannot be obtained yet, as the ratio of $\underline{F}_{\Delta H}$ to $\underline{\tilde{F}}_{\perp \psi, ax}$ is unknown. Based on the survey of experiments in figure 2.4, a 10% increase of induced power is expected. For a propeller this implies a 10% increase of power loss, for a wind turbine the maximum attainable efficiency then increases from the classical value 0.59 to 0.65.

3.3 The conservation laws for general non uniform load distributions

The load distribution consisting of a constant, normal surface load with edge forces, is a particular non-uniform load distribution: owing to the uniform surface load it is possible to combine the conservation laws for mass, momentum and energy in order to derive explicit expressions for the induced power etc.. For a general non-uniform load distribution a closed-form solution for the converted power is not possible since this requires the distribution of the velocity at the disc or strip to be known. Assume a disc or strip with area A_d covered with a distribution of \underline{F} , which is not specified further. The flow upstream is assumed to have the uniform velocity U_0 . Using the notations of fig. 3.1, the momentum balance reads:

$$T = \int_{A_d} F_x dA = \int_{A_\infty} \rho u_\infty (u_\infty - U_0) dA . \quad (3-15)$$

As explained in section 3.1, the pressure term does not enter momentum balance. The power converted to or from the flow is determined by:

$$P = \int_{A_d} \underline{F} \cdot \underline{v} dA = \int_{A_\infty} u_\infty H_\infty dA - \int_{A_0} U_0 H_0 dA , \quad (3-16)$$

and the conservation of mass in the streamtube passing through the surface is expressed by:

$$\int_{A_\infty} u_\infty dA = U_0 A_0 . \quad (3-17)$$

If the load is uniform and normal, as in the classical momentum theory, the integrals are easily evaluated since also u and H are constant in the far wake. The power then becomes $P = F \int u dA = T \bar{u}_d$, where $T = FA$ is the thrust and \bar{u}_d the average velocity through the disc. Substitution of (3-15) into (3-16) yields the well-known classical results. For any non-uniform distribution of F or u_d it is clear that $P \neq T \bar{u}_d$, and the results of the classical theory do not apply.

It is clear that a real rotor has a non-uniform load. The distribution with edge forces is a particular non-uniform distribution; as shown in the previous section, the induced power then exceeds the classical prediction of induced power if $C_T > C_{T,\Delta H}$. In chapter 2 we showed that for a real rotor the thrust converting power is smaller than the total thrust, by which $C_T > C_{T,\Delta H}$, while at the same time an increase of induced power compared with the classical prediction was observed. Therefore it is expected that the constant surface load with edge forces is a better representation of the non-uniform rotor load than the constant load in Froude's concept. This is investigated in the next chapter, in the interpretation of measurements on a rotor.

Chapter 4

EXPERIMENTAL VERIFICATION OF THE MOMENTUM THEORY INCLUDING EDGE FORCES ON A MODEL ROTOR IN HOVER

This is the only chapter concerning a rotor with a finite number of blades.

A real rotor differs from an actuator disc in some important features: the finite number of blades, the load on the blades which is not constant and the increase of angular momentum of the wake. The classical momentum theory tries to predict rotor performance by direct application of the actuator disc results and ignoring all differences between the physical rotor and the mathematical disc. Therefore the 10–15% discrepancy mentioned in Chapter 2 is not too surprising. The same procedure is followed now. The momentum theory based on the actuator disc concept with edge forces, which is referred to as the modified momentum theory, is applied in a straightforward manner to a real rotor in hover. The performance prediction is compared with the measured performance. Again a perfect agreement is not expected due to the important differences between rotor and disc, but a significant improvement should be the result. The first section discusses the interpretation of the momentum theory for real rotors. Then the main features of the experimental method are explained; the details are found in appendix E. Finally the results are presented. The installation of the rotor model and equipment, the preparation of the measurements and preliminary results have been reported in Dutch in Beekman [1985], van der Hoek & Pel [1987] and van Schijndel [1987].

4.1. The momentum theory for real rotors

In Chapter 3 the actuator disc momentum theory including edge forces has been described. Application of this theory to a real rotor situation necessitates an adapted

interpretation of the results. The mass- and momentum balances underlying this method are integral balances: the total amount of axial momentum and mass flow in the wake is coupled to the total thrust at and the total mass flow through the rotor. The distribution of the velocity at the rotor does not appear in the results. Both balances have to be satisfied exactly; that is to say: within the accuracy of the measurements.

The momentum balance has been the subject of experiments reported by Vermeulen [1979]. He measured the total thrust on a wind turbine model (2 blades, $R = .36$ m, tip speed ratio $\Omega R/U_0 = 6.6$) placed in a windtunnel (cross-section 3.18 m²). At a downstream distance of 1.67 diameter the velocity, static pressure and turbulence profiles were measured. The change of momentum determined in this way differed only $\sim 1,3\%$ from the measured thrust, which is the order of the measurement accuracy.

The way of applying the energy equation is the weak point in the momentum theory, since here the distribution of the force and flow field at the disc is important. The application of the momentum theory including edge forces on a real rotor in fact implies that the thrust can be divided into two parts: the load doing work, distributed uniformly on the rotor disc, and the load not doing work, located at the disc edge. It is this assumption that is to be validated by the experiment.

The thrust doing work is denoted by T_{work} , which is equivalent to $T_{\Delta H}$ in chapter 3. The energy balance (3-2) is valid in an average sense since u_w , the velocity in the far wake, is not constant across the wake. Therefore the disc load $F_{\Delta H}$ is replaced by $T_{\text{work}}/\pi R^2$, and u_w by \bar{u}_w , being the value averaged on the wake cross section. The combination of (3-2) and (3-6) then yields for a rotor in hover ($U_0 = 0$):

$$\bar{u}_d = \sqrt{\frac{T_{\text{work}}}{2\rho A_d}} \frac{T_{\text{total}}}{T_{\text{work}}} = \frac{1}{2} \bar{u}_w \frac{T_{\text{total}}}{T_{\text{work}}}, \quad (4-1)$$

where \bar{u}_d is the average velocity through the rotor. The thrust component T_{work} is defined as the effective thrust doing work:

$$T_{\text{work}} = \frac{P}{\bar{u}_d}, \quad (4-2)$$

where P is the power. The average mass flow through the rotor defines \bar{u}_d which is determined by the mass balance:

$$\bar{u}_d = \iint_{A_{\text{wake}}} u \frac{dA}{\pi R^2} \quad (4-3)$$

where A_{wake} is a plane perpendicular to the rotor axis sufficiently far downstream: the contraction of the wake must be completed to ensure that the net mass flow through the wake boundary is zero. Figure 4.1 shows schematically the tip vortex trajectories for a 2-bladed rotor, with the expected axial velocity distribution in the plane A_{wake} : Figure 4.2 shows the vortex sheet. If T_{total} , P and \bar{u}_d are known, (4-1) predicts \bar{u}_∞ which should equal $\bar{u}_{A_{\text{wake}}}$. The word "should" is used as two difficulties are encountered in equating \bar{u}_∞ to $\bar{u}_{A_{\text{wake}}}$. First it is difficult to choose the downstream distance of A sufficiently large, as the diffusion of the vortices and vortex sheets increases rapidly. From literature (Kocurek & Tangler [1977]) it is known that for a 2-bladed rotor, 4 complete windings of the spiraling tip vortices are visible in smoke pictures. Further downstream the vortices dissolve and one cannot distinguish a wake structure anymore. The second problem is to define the wake cross-section area on which $\bar{u}_{A_{\text{wake}}}$ is averaged. This is quite arbitrary, but it is common to define the radial distance of the tip vortex kernel as the radius of the wake. This necessitates a clearly distinguishable tip vortex position. In the experiment a downstream distance $x = \frac{1}{2}R$ is chosen. In the discussion on the results we will see whether this was acceptable.

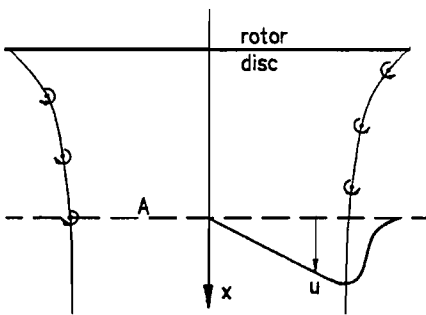


Figure 4.1
Tip vortex trajectories for a 2-bladed rotor

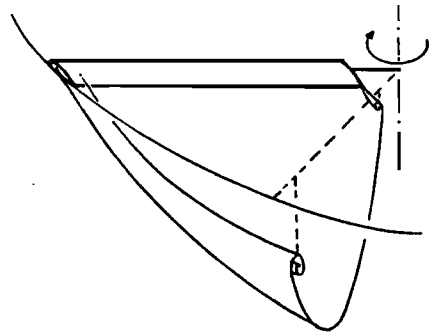


Figure 4.2
The vortex sheet.

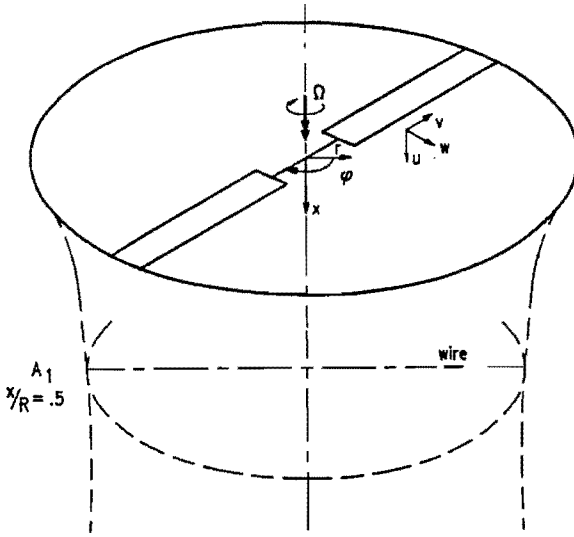


Figure 4.3. Survey of symbols and sign conventions.

4.2. The determination of the power

In the remainder of this chapter we use the cylindrical coordinate system (x, r, φ) having its origin at the rotor center. The downstream direction is taken as positive, see figure 4.3. The corresponding velocity components are u , v , and w respectively. Figure 4.4 shows the integration volume G , with surface A . This surface is divided into two parts: A_1 being the plane perpendicular to the x -axis, at $x = .5R$, and A_0 being the surface of a semi-sphere with an infinite radius.

In the inertial frame of reference the flow is unsteady but periodic. The power is determined by the dot product of \underline{f} and \underline{v} , using the unsteady Euler equation (5-5):

$$\begin{aligned}
 P &= \iiint_G \underline{f} \cdot \underline{v} \, dG = \iiint_G \left[\underline{v} \cdot \underline{\nabla} H + \rho \underline{v} \cdot \frac{\partial \underline{v}}{\partial t} \right] dG \\
 &= \iiint_G \underline{v} \cdot \underline{\nabla} H \, dG + \frac{\partial}{\partial t} \iiint_G \frac{1}{2} \rho \underline{v} \cdot \underline{v} \, dG \quad (4-4)
 \end{aligned}$$

The last term in the right-hand side of (4-4) expresses the time derivative of the

amount of kinetic energy in control volume G . Since G is spherical and the flow is periodical, this amount is constant in time by which the last term in (4-4) becomes zero. Then P is rewritten as a surface integration using Gauss' divergence theorem, and the continuity equation $\nabla \cdot \underline{v} = 0$:

$$\begin{aligned}
 P &= \iiint_G \underline{v} \cdot \nabla H \, dG = \iiint_G \left[\nabla \cdot (\underline{v} H) - H \nabla \cdot \underline{v} \right] dG \\
 &= \iint_A v_n H \, dA \quad (4-5)
 \end{aligned}$$

Here A is the surface of the integration volume G , consisting of $A_0 + A_1$. Far upstream, so at A_0 , \underline{v} tends to zero and the Bernoulli constant is $H_0 = p_0$. Since by conservation of mass

$$\iint_A v_n H_0 \, dA = 0 \quad (4-6)$$

H_0 may be subtracted from the integrand of (4-5) yielding $v_n(H - H_0)$. At A_0 H equals H_0 , so the expression for P becomes:

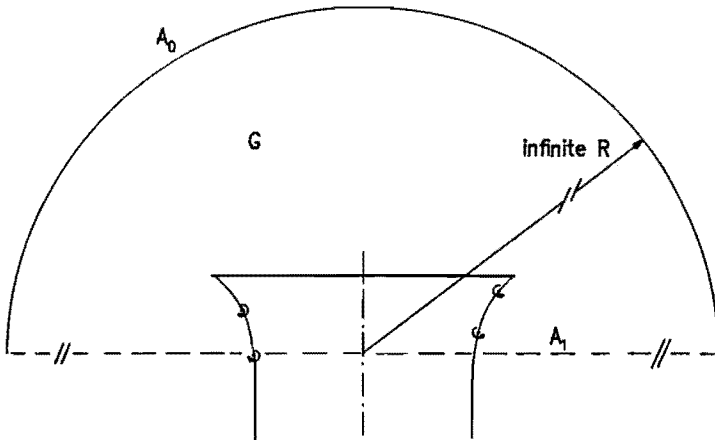


Figure 4.4. Definition of the integration volume G with surface A .

$$P = \iint_{A_1} v_n (H - H_0) dA = \iint_{A_1} u (H - H_0) dA \quad (4-7)$$

The change of H in the wake is connected to the azimuthal velocity component w , by the relation:

$$H - H_0 = \rho w \Omega r, \quad (4-8)$$

which has been obtained by Thwaites [1960, p. 473] and de Vries [1979, p. B2]. Substitution of (4-11) yields:

$$P = \iint_{A_1} \rho u w \Omega r dA_1 \quad (4-9)$$

Since $P = Q \Omega$ where Q is the torque on the rotor axis, the right-hand side of (4-9) divided by Ω expresses the increase of the angular momentum of the flow. (4-7) and (4-9) are equivalent. In the following we will use (4-7). Equation (4-8) is used to determine the azimuthal velocity in the wake.

4.3. The measuring devices

The model itself is described in appendix E. The main features are repeated here:

- 2 straight untwisted blades
 - chord $c = 1/10 R$; $R = 0.51$ m
 - blade-pitch angle 8°
 - $\Omega = 18\pi$ radians per second (9 Hz)
 - rigid blade mounting.
- (4-10)

The measuring devices are: a hot wire, a balance, a pitot-static tube and a total pressure tube.

The balance is used for the thrust measurement. During this measurement, the model has been mounted on a hinge; the thrust was compensated by the balance force. The rotor was in exactly the same position as during the other measurements where the hub was fixed.

The hot wire is 5 mm long ($l/R = 0.01$), and the diameter to length ratio is $1/1000$. This provides an independence of the hot wire signal with respect to the tangential velocity component. This is calibrated, see appendix E. The wire is situated in plane A_1 , see figures 4.3 and 4.5. Since it is directed radially, the wire measures $\sqrt{u^2 + w^2}$. The sampling frequency of the digital recording system is chosen in such a way that 222 measuring points per revolution are taken. The position of a one-per-revolution trigger pulse is known, so the time dependency can be transferred to a φ -dependency. Three series of 9 revolutions are recorded at each wire position.

The same wire is used to determine the position of the tip vortex core in plane A_1 . Now the wire has a tangential direction, measuring $\sqrt{u^2 + v^2}$. In the core itself this velocity is almost zero, while it is very large just outside the core. If the tip vortex core passes the wire, the wire signal shows a sharp discontinuity. By traversing the wire radially until this discontinuity appears, the radial position of the tip vortex is determined.

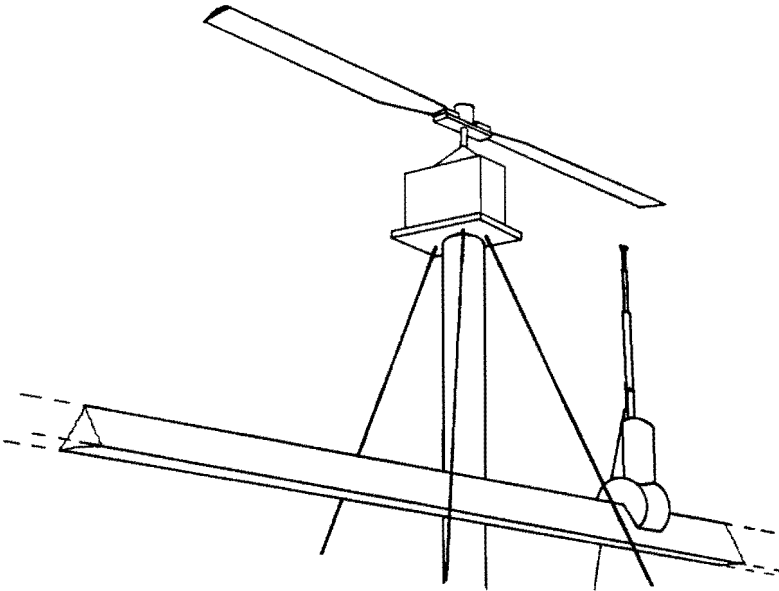


Figure 4.5. The position of the hot wire

A pitot-static tube is used to measure the average kinematical pressure for $r/R \leq 0.4$. Close to the rotor axis the hot-wire measurements are not possible, and the average velocity is extrapolated to $r = 0$. The pitot-tube measurements are used as confirmation of this extrapolation, not for quantitative values.

A common total-pressure tube is used to determine the average total pressure. The dimensions of the tube itself and of the connecting flexible hoses are chosen such that a non-linear response of the Betz-manometer is avoided, yielding as result the true average total pressure.

The sensitivity of the total-pressure tube to misalignment of the flow is calibrated (see appendix E, a misalignment of 15° is not felt by the tube). At each radial position, the tube was aligned to the averaged flow direction known from preliminary measurements.

Not really a measuring device, but a necessary tool for the study of the flow system is stroboscopic photography of smoke injected in the flow. The smoke jet is traversed radially, and the phase delay between trigger pulse and stroboscopic flash is adjusted to have pictures every 10° of φ .

4.4. The elaboration of the measurements

The following data are the result of measurements:

- the total thrust
- in plane A_1 , $x/R = .5$:
 - the local values of $\sqrt{u^2 + w^2}$ for $.4 \leq r \leq 1$
 - average values of the total pressure H for $.4 \leq r/R \leq 1$
 - the position of the tip vortex core
- the air density ρ .

By (4-8) the total pressure data $\overline{H(r) - H_0}$ also provide the velocity component $\overline{w}(r)$, where the bar denotes averaging on the azimuthal position φ . The combination of the hot wire and total pressure data yields an approximation for the axial velocity $\overline{u}(r)$:

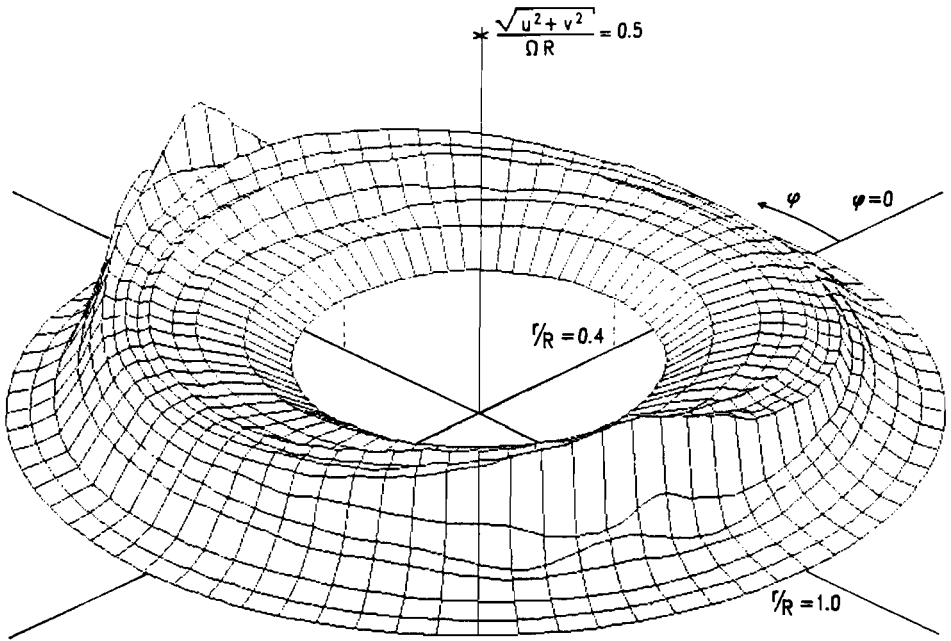


Figure 4.6. $\sqrt{u^2 + w^2}$ in plane A_1 , $x/R = 0.5$, shown in a co-rotating frame of reference. The grid consists of lines with constant r/R and constant φ . The increment of φ is 5° . The positions $\varphi = 0^\circ$ and 180° are the blade positions.

$$\bar{u}(r) = \sqrt{u^2(r) + w^2(r)} - \left[\frac{H(r) - H_0}{\rho \Omega r} \right]^2. \quad (4-11)$$

Figure 4.6 shows $\sqrt{u^2 + w^2}$ as measured with the hot wire in plane A_1 : the distribution with respect to φ is fairly uniform except at the tip vortex positions ($\varphi \sim 90^\circ$ and $\varphi \sim 270^\circ$). Since this concerns only a small region of the rotor disc, the error made by the approximation (4-11) is assumed to be small. In the same way equation (4-7) for the power P is approximated by:

$$P = 2\pi \int_{A_1} \bar{u}(r) \left[H(r) - H_0 \right] \Omega r \, r dr. \quad (4-12)$$

In section 4.6 this will be discussed. The distributions of $\bar{u}(r)$ and $H(r) - H_0$ are shown in figures 4.8 and 4.9 respectively.

The air density ρ is the only variable not free to choose. It varied 2% during the measurements. A dimension analysis shows that this variation can be canceled by introducing a non-dimensional representation. The reference velocity is usually taken to be the average wake velocity u_w which is not known yet. Therefore only a partial non-dimensional representation is used: all relevant quantities are divided by the air density ρ at the time of the measurement.

Before the results are presented, we summarize all steps necessary to obtain the ratio T_{work}/T , with reference to the equations used:

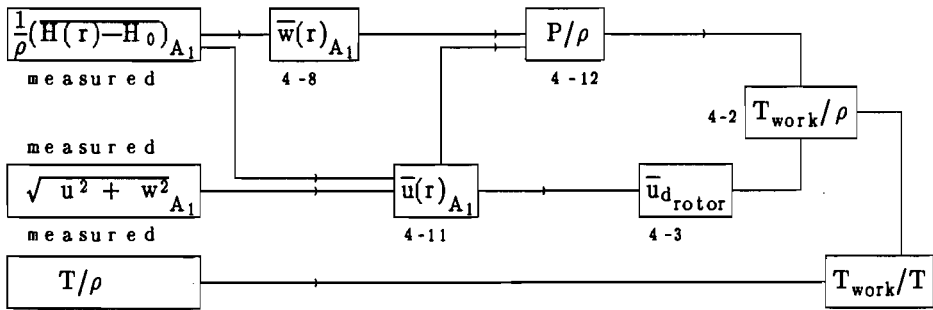


Figure 4.7. Schematic of the power, thrust and velocity measurements.

The average flow through the rotor is determined by (4-3) in plane A_1 at $x/R = 0.5$:

$$\overline{u}_d = \iint_{A_1} u \frac{dA}{\pi R^2} = \int_{A_1} \overline{u}(r) d\left[\frac{r}{R}\right]^2 = 2.21 \quad \text{m/s.} \quad (4-13)$$

The power of the rotor is given by (4-12):

$$\frac{1}{\rho} P = 2\pi \int_{A_1} \overline{u}(r) \left[\frac{\overline{H(r)} - H_0}{\rho} \right] \Omega r \, r dr = 9.08 \quad \text{m}^5/\text{s}^3. \quad (4-14)$$

The interpolation of the measured data for $0 \leq r/R \leq 0.4$ is a linear one; at $r = 0$, \overline{u} and \overline{H} are assumed to be zero. This is confirmed by the measurement of the kinematical energy $\frac{1}{2} \rho \underline{v} \cdot \underline{v}$ by a standard pitot-static tube.

The total thrust is:

$$\frac{1}{\rho} T = 4.98 \quad \text{m}^4/\text{s}^2. \quad (4-15)$$

With (4-2), the component of the thrust doing work T_{work} is determined:

$$\frac{1}{\rho} T_{\text{work}} = \frac{1}{\rho} \frac{P}{\bar{u}_d} = 4.12 \quad \text{m}^4/\text{s}^2. \quad (4-16)$$

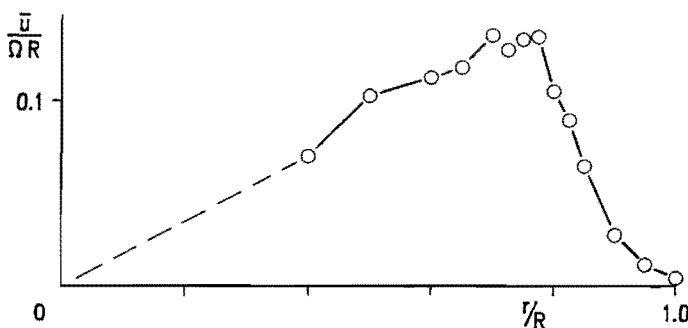


Figure 4.8. The distribution of the azimuthally averaged axial velocity $\bar{u}(r)$ in plane A_1 .

The results (4-12) through (4-16) are required to predict the ultimate wake contraction R_w/R by the momentum theory. The experimental determination of R_w for this model is only approximate. Figure 4.10 shows the tip vortex trajectory: the wake contraction is not completed in plane A_1 at $x/R = 0.5$, so $R_1 > R_w$, where R_1 is the radius of the tip vortex as measured by the hot wire:

$$\frac{R_1}{R} \approx 0.8. \quad (4-17)$$

Based on figure 4.6 and on a study of the smoke pictures in figure 4.10, R_1 is also determined as $\approx 0.8 R$. A separate measurement of R_∞ at a position $x > 0.5R$ is not possible. Figure 4.10 shows that the vortex cores are not visible any more as the vortex structure has desintegrated. The smoke pictures indicate a small contraction for $x > 0.5R$, but a quantitative estimate is difficult. A reasonable estimate is:

$$\left[\frac{R_\infty}{R} \right]_{\text{estimated}} \approx 0.77 \pm 0.01. \quad (4-18)$$

This agrees with the common experimental value which is about 0.74 to 0.77.

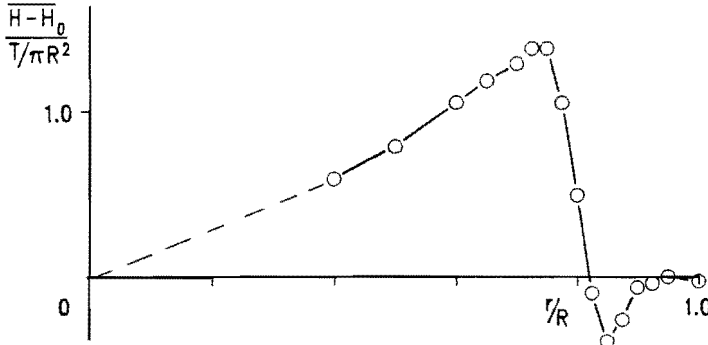


Figure 4.8. The distribution of the azimuthally averaged $\overline{H(r) - H_0}$ in plane A_1 .

4.5. Comparison with momentum theory results

Using (4-15) and (4-16) the ratio $T_{\text{total}}/T_{\text{work}}$ is:

$$\frac{T_{\text{total}}}{T_{\text{work}}} = 1.21, \quad (4-19)$$

or: only 83% of the thrust is effective in doing work. Substitution of (4-19) in (4-1) gives as prediction for \bar{u}_d/\bar{u}_∞ :

$$\frac{\bar{u}_d}{\bar{u}_\infty} = \frac{1}{2} \frac{T_{\text{total}}}{T_{\text{work}}} = 0.61. \quad (4-20)$$

Since $\bar{u}_d R^2 = \bar{u}_\infty R_\infty^2$ this implies:

$$\left[\frac{R_\infty}{R} \right]_{\text{predicted}} = 0.78, \quad (4-21)$$

which agrees very well with the experimental value 0.77 of (4-18). The classical momentum theory predicts $R_{\infty}/R = \sqrt{2} = 0.707$.

Equations (4-20) and (4-21) concern relative values. An absolute prediction of the average velocity through the rotor \bar{u}_d is provided by (4-1), which becomes using (4-19):

$$\bar{u}_d = 1.92 \quad \text{m/s}, \quad (4-22)$$

which is 13% lower than the measured value 2.21 m/s. This should be compared with the prediction by the classical momentum theory $\bar{u}_d = \sqrt{T/2\rho A_d} = 1.74$ m/s, which is 21% lower than the measured value.

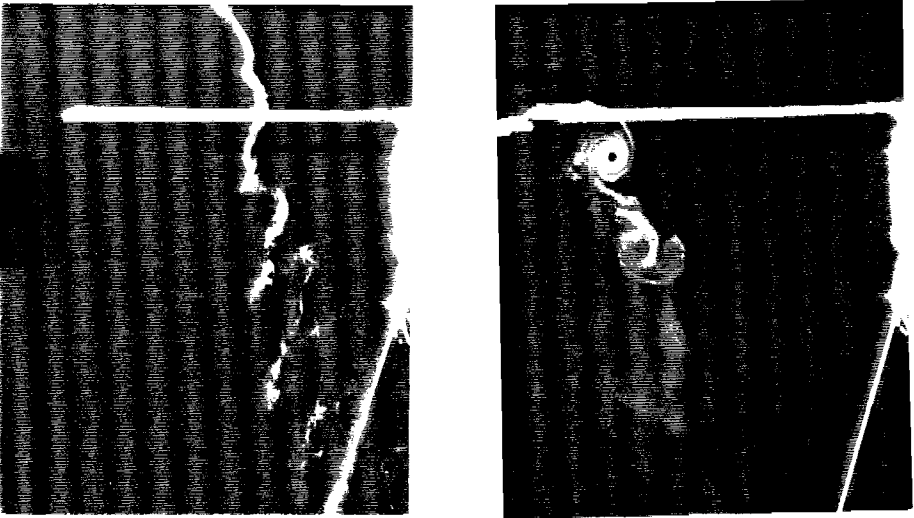


Figure 4.10. Flow visualization by stroboscopic photography of smoke filaments. The left photograph shows a cross-section through the vortex sheet, while the right one shows the tip-vortex, both at $\varphi = 160^\circ$.

4.6. The accuracy of the experiment

The accuracy of the results is determined by the accuracy of the measurements, and by the (propagation of) errors in the subsequent steps shown in figure 4.7.

The experimental sources of inaccuracy are the model and its surroundings, and the measurements themselves. In the subsequent steps the determination of $\bar{u}(r)$ by (4-11) and the approximation (4-12) for the power expression (4-7) introduce the largest errors. The other equations denoted in figure 4.7 do not generate errors: $\bar{w}(r)$ is determined by (4-8) which expresses an identity; the determination of \bar{u}_d by (4-3) is exact, and T_{work} is given by the definition (4-2). Therefore the weak point in the scheme of figure 4.7 are equations (4-11/12). This equation is exact if $u(r)$ and $w(r)$ are distributed uniformly with respect to the azimuthal coordinate φ . Since the distribution of $\sqrt{u^2 + v^2}$ in plane A_1 is fairly uniform, see figure 4.6, also the distributions of u and w are expected to be so. The determination of the inaccuracy of (4-11) is covered by an overall check of the accuracy which is presented below. From trial calculations we expect a maximum of 5% inaccuracy to be present in (4-12).

The sources of inaccuracy inherent to the measurement equipment are the following. The hot wire does not yield the local value of the velocity, but a value averaged over the wire length (1% of the radius R). The calibration of the wires is accurate up to 1% (see appendix E). As all measurements are averaged on at least 25 revolutions, while the angular speed is kept constant within 0.5%, the velocity measurements are assumed to be very accurate. The traversing mechanism used to vary the radial position of the wire and the total pressure tube is adjusted by hand. The estimated accuracy of this radial position is 1% of the radius R . The reading of the Betz manometer is averaged on at least 50 revolutions, and is assumed to be accurate up to 5%. Finally we have the measurements of the thrust T and the air density ρ : the accuracy of these steady measurements is determined by the accuracy of the equipment, which is better than 1%.

The draught in the hall where the model was installed together with the instability of the vortex break down and possibly some recirculation via the surroundings caused the averaged flow field in plane A_1 to swing slightly around the position $r = 0$. Furthermore the velocity distribution in plane A_1 shows some asymmetry, as shown by figure 4.6. This can be the result of a dissimilar development of the two tip vortices if their strengths are not perfectly equal owing to model inaccuracies. Nevertheless, the pattern is very regular which indicates that the swinging of the wake still results in a well-defined average mass flow.

The effect of the latter phenomena: model inaccuracies, draught and influence of walls, floor and ceiling, prohibits a formal estimate of the final accuracy. As an overall check which covers all sources of inaccuracy except the use of (4-12) instead of (4-7), the axial momentum balance has been checked. This balance is written as:

$$\frac{1}{\rho} T_{\text{tot}} = \iint_{A_1} u^2 dA + \frac{1}{\rho} \iint_{A_1} (p - p_0) dA \quad (4-23)$$

The first term on the right-hand side is the momentum flux, the second term accounts for the static pressure in the wake. The first term equals $5.40 \text{ m}^4/\text{s}^2$, being 1.08 times the left-hand side. The static pressure has not been measured but is approximated by the difference of $\bar{H}(r)$, measured by the total pressure tube, and $\frac{1}{2}\rho(u^2 + w^2) + \frac{1}{2}\rho v^2$. The first term of the kinematical pressure has been measured by the hot wire, the second will be estimated. The radial velocity v reaches significant values near the boundary of the wake formed by the tip vortices. By comparing the distribution of $\bar{u}(r)$ in figure 4.8, we assume that $|v|$ in plane A_1 is non-zero only for $0.7 \leq r/R \leq 0.84$, with a maximum of $0.05u/\Omega R$ at $r/R = 0.77$. A linear distribution is assumed between the positions $0.7R$, $0.77R$ and $0.84R$. Then the contribution of $\frac{1}{2}v^2$ to the thrust balance amounts $-0.29 \text{ m}^4/\text{s}^2$. This yields for the pressure term in (4-23):

$$\begin{aligned} \frac{1}{\rho} \iint_{A_1} (p - p_0) dA &\approx \int_A \left[\frac{1}{\rho} \bar{H} - \frac{1}{2} \overline{(u^2 + w^2)} - \frac{1}{2} \overline{v^2} \right] r dr \\ &\approx -0.045 - 0.29 = -0.335 \quad \text{m}^4/\text{s}^2. \end{aligned} \quad (4-24)$$

Substitution in (4-23) shows that the momentum balance is satisfied within 1.7%. However it should be noted that the pressure is determined by a very inaccurate method, since it is obtained by subtraction of two quantities of nearly equal magnitude. A conservative conclusion is that the momentum balance is satisfied with a margin $< 5\%$ of the total thrust. As the measured difference between T_{work} and T_{total} amounts 17%, this difference is considered to be significant.

4.7. Discussion and conclusion

The main result is that the effective part of the thrust, defined as the thrust doing work, is only 83% of the total thrust. Using this ratio in the momentum theory with edge forces, the prediction of the wake diameter equals the experimental wake diameter, while the classical theory prediction is 8% too low. The prediction of the

average velocity through the rotor plane is worse: the momentum theory of chapter 3 yields a result which is 13% too low. A clear improvement is present with respect to the classical prediction, which is 21% too low. Nevertheless the deviation from the experimental value is not satisfactory. The origin of this deviation must be sought in the use of the energy balance (3-2), as we will show.

As discussed in chapter 3, the average velocity in the far wake is determined by the energy balance alone, while the prediction of the average velocity through the rotor is the result of a combined application of the balances of mass, momentum and energy. Now the velocities \bar{u}_w and \bar{u}_d appear to exhibit similar deviations between measured and predicted values, which indicates that the application of (3-2) is the source of the discrepancy in the prediction of the velocities. For a rotor in hover (3-2) reads with $F_{\Delta H} = T_{\text{work}}/\pi R^2$:

$$\frac{T_{\text{work}}}{\pi R^2} = \frac{1}{2} \rho u_w^2, \quad (4-25)$$

so using (4-16) the predicted value is:

$$\bar{u}_w^{\text{predicted}} = 3.175 \quad \text{m/s}, \quad (4-26)$$

while

$$\bar{u}_w^{\text{measured}} = \iint_{A_1} \frac{u}{\pi R^2} dA = 3.72 \quad \text{m/s}, \quad (4-27)$$

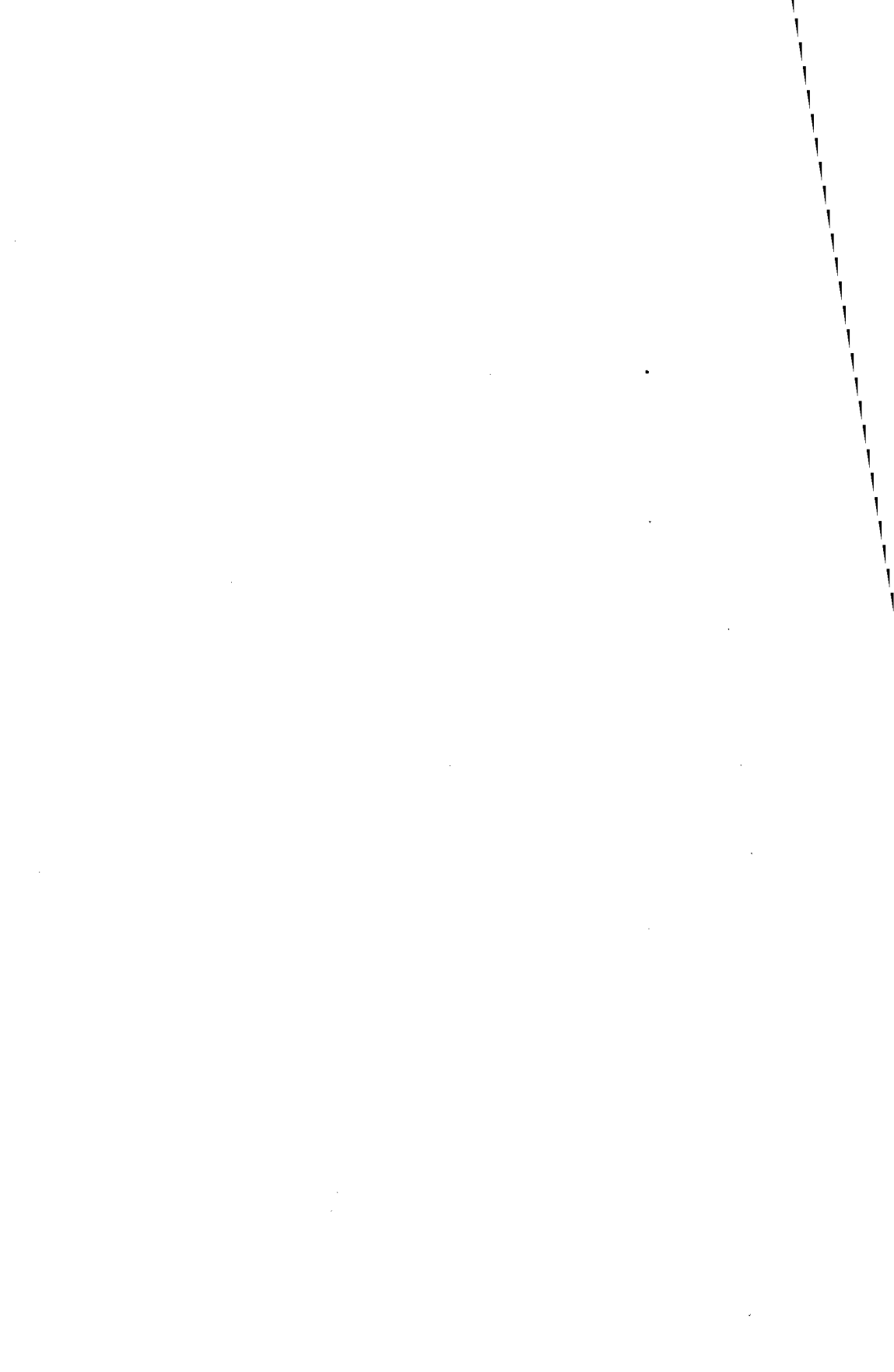
where we have used (4-13) and (4-18). The large difference between (4-26) and (4-27) shows that (3-2), which was derived for a disc with a uniform load is unable to predict \bar{u}_w for a rotor accurately. This is not too surprising: (3-2) represents the application of Bernoulli's law on a single streamline. Only because $F_{\Delta H}$ is constant for the disc in chapter 3, it is allowed to write $F_{\Delta H} = T_{\Delta H}/\pi R^2 = 1/2 \rho u_w^2$. The condition of constant $F_{\Delta H}$ is certainly not satisfied in the rotor flow, by which (4-25) is doubtful.

The aim of the experiment was to compare measured results with values predicted by the momentum theory in which the rotor load is represented by a specific non-uniform load, namely the disc with constant surface load and discrete edge forces, instead of a uniform load as assumed by Froude. Therefore an essential step is the replacement of the real load distribution by an equivalent artificial distribution. This is done in

section 4.1, based on two criteria: the total thrust on the disc $T = T_{\text{surface}} + T_{\text{edge}}$ equals the rotor thrust, and the thrust originating from the disc surface load is $T_{\text{surface}} = T_{\text{work}} = P/\bar{u}_d$. The latter relation is a definition of T_{work} and replaces the energy balance (3-2) in case of real rotor flows. Apparently this interpretation of the energy balance is appropriate as far as it concerns momentum theory expressions which depend on T and T_{work} such as (4-1). T and T_{work} are integrated load distributions; as soon as the local value of the load is concerned, as is in (3-2), this interpretation of the energy balance is not allowed.

The final conclusion is that the momentum theory including edge forces together with the definition (4-2) of the effective thrust improve the performance prediction significantly compared with respect to the classical momentum theory. The effective thrust, defined as the part of the total thrust which converts power to the flow, is only 83% of the total thrust. Using this ratio, the wake contraction is predicted very accurately. The prediction of the absolute value of the velocity through the rotor shows a clear improvement compared with the classical prediction, but is still 13% below the measured value. The improvement of this prediction requires an analytical model for the rotor which accounts for a more detailed non-uniform load distribution than the specific non-uniform model of chapter 3: a uniform distribution on the disc surface with discrete forces on the disc edge.

Part II : The force and flow field of the actuator surface



Chapter 5

THE EQUATION OF MOTION

This chapter is an introduction to the numerical analysis of the 2-D actuator strip flow in chapter 6, and the analytical analysis of the actuator strip and disc in chapters 7 and 8. The actuator disc and strip are distributions of a force density over a surface and the problem is to determine the flow induced by these force density distributions. Kinematically the flow is determined by the vorticity shed from the actuator strip or disc. Therefore we discuss in the first section the appropriate equation of motion describing the generation of vorticity by force density distributions. The specific force field of an actuator strip or disc is defined in the second section, while a dimensional analysis determines the region of validity of possible flow solutions in the third section. If the distinction between the actuator strip and disc is of no importance, we use the notation actuator surface.

5.1. The equation of motion including the force field term

We assume the fluid to be incompressible, homogeneous and inviscid. Inviscid flow is defined here as the result of viscous flow in the limit $Re \rightarrow \infty$, where Re is the Reynolds number defined in section 5.3. The force density distributions represent the action of bodies on the flow, and are confined to a limited region: force fields acting throughout space such as gravity fields are excluded. In case of the actuator surface flow the origin of the force field is explained in section 2.3. There the sequence of limit operations is listed which transforms the force field of a rotor blade to the force field of an actuator disc. Such an actuator disc is permeable and occupies no space: the body, in this particular case the rotor blade, has disappeared during this sequence of limits. The externally applied force density is denoted by f_{ext} defined in section 5.2, and is perpendicular to the surface over which it is distributed.

The equation of motion to describe viscous flows induced by a force density

distribution is the Navier-Stokes equation with the additional term $\underline{f}_{\text{ext}}$:

$$\rho \frac{D\underline{v}}{Dt} = -\underline{\nabla} p + \underline{f}_{\text{ext}} + \mu \nabla^2 \underline{v} \quad (5-1)$$

Since the flow is incompressible the continuity equation is:

$$\underline{\nabla} \cdot \underline{v} = 0 \quad (5-2)$$

These equations suffice to determine the flow for a given $\underline{f}_{\text{ext}}$. If the viscous term in (5-1) is absent, this equation becomes the Euler equation with the force density term added.

Now we submit (5-1) to the limit of increasing Reynolds number. It is convenient to transform the equation using non-dimensional variables to:

$$\frac{D\underline{v}'}{Dt'} = \underline{f}'_{\text{ext}} - \underline{\nabla}' p' + \frac{1}{\text{Re}_L} \nabla'^2 \underline{v}' \quad (5-3)$$

where $\underline{v}' = \underline{v}/U$, $\underline{f}' = \underline{f}/\rho U^2$, $p' = p/\rho U^2$, $t' = Ut/L$ and $\text{Re}_L = \rho UL/\mu$. U and L are the characteristic velocity and length. We assume that it is possible to define such a Reynolds number, which is discussed in section 5.3. The limit $\text{Re}_L \rightarrow \infty$ yields the Euler equation unless $|\nabla'^2 \underline{v}'|$ increases proportional with Re_L at the same time. In section 5.3 we will show that this is the case for actuator surfaces with smooth force distributions, and we cannot a priori assume that the viscous term $\nabla^2 \underline{v}$ in (5-1) vanishes for $\text{Re}_L \rightarrow \infty$. Therefore this shear stress term is maintained in the equation of motion until the order of it is known. As the shear stress is a force density, we denote it as $\underline{f}_{\text{shear stress}}$. The complete distribution of \underline{f} then is:

$$\begin{aligned} \underline{f} &= \underline{f}_{\text{ext}} + \underline{f}_{\text{shear stress}} \\ \underline{f}_{\text{shear stress}} &= \mu \nabla^2 \underline{v} = -\mu \underline{\nabla} \times \underline{\omega} \end{aligned} \quad (5-4)$$

The externally applied force field is free to choose; $\underline{f}_{\text{shear stress}}$ depends on $\underline{f}_{\text{ext}}$ and on the flow itself, and is not known a priori. However, for zero viscosity it is clear that $\underline{f}_{\text{shear stress}}$ can be non-zero only for infinite values of $\nabla^2 \underline{v}$.

Rewriting (5-1) and substitution of (5-4) yields the formulation of the equation of

motion to be used in this chapter and chapters 7 and 8:

$$\underline{\nabla} H = \underline{f} + \rho \underline{v} \times \underline{\omega} - \rho \frac{\partial \underline{v}}{\partial t}, \quad (5-5)$$

where H is the Bernoulli constant $p + \frac{1}{2}\rho \underline{v} \cdot \underline{v}$. The equations (5-1) and (5-4) + (5-5) are equivalent and it depends on the actual flow problem which formulation is most convenient. Suppose the viscous solution is known by solving (5-1). Submitting this solution to the limit $Re \rightarrow \infty$ then yields the required solution including the remainder of the shear stress. The alternative approach is to use (5-5) with the appropriate kinematical boundary conditions. For the actuator disc or strip flow these conditions apply at infinity and, in case of the strip, at the symmetry line (see for example section 6.2.2). Suppose (5-5) can be solved for \underline{f} , then comparison of this solution with (5-4) will show whether a shear stress component of \underline{f} is present or not. In appendix F we have applied both methods to the flow along a solid boundary in order to investigate the equivalence. Now the boundary condition is no-slip and zero normal flow at the solid boundary. The following quotation of Meyer ([1982], page 91, with some adaptations in order to be readable here) indicates that the shear stress is non-zero in case of flows along a solid boundary, although the Reynolds number becomes infinite: "*We must generally anticipate that $|\nabla^2 \underline{v}'| \rightarrow \infty$ somewhere in the fluid as $Re \rightarrow \infty$, for otherwise the term $Re^{-1} \nabla^2 \underline{v}'$ would indeed become negligible in (5-3) so that the solution of (5-3) would tend to a solution of the Euler equation of motion, which has been shown . . . to be usually incompatible with the no-slip condition.*" Indeed the shear stress term in the viscous solution of (5-1), given by Prandtl's boundary layer equations, appears to remain finite for $Re \rightarrow \infty$. The application of (5-5) yields an identical result for the tangential force density, which is the shear stress.

The equation describing the generation of vorticity is given by taking the curl of (5-5):

$$\begin{aligned} \frac{1}{\rho} \underline{\nabla} \times \underline{f} &= \frac{\partial \underline{\omega}}{\partial t} + (\underline{v} \cdot \underline{\nabla}) \underline{\omega} - (\underline{\omega} \cdot \underline{\nabla}) \underline{v} \\ &= \frac{D \underline{\omega}}{Dt} - (\underline{\omega} \cdot \underline{\nabla}) \underline{v} \end{aligned} \quad (5-6)$$

The last term describes changes of already existing vorticity. The generation of vorticity on streamlines which are irrotational before passing the actuator surface is determined by $\nabla \times \underline{f}$.

With \underline{f} interpreted as in (5-4), (5-5) or (5-6) is used in the following chapters as the equation of motion, except in section 6.2 where viscous calculations with increasing Reynolds numbers are based on (5-1). Equation (5-5) is the usual equation of motion in the literature on flows induced by force fields, see e.g. von Karman & Burgers [1935], Wu [1962], Greenberg [1972] and Sparenberg [1985]. In none of these references the distinction between $\underline{f}_{\text{ext}}$ and $\underline{f}_{\text{shear stress}}$ is made: implicitly \underline{f} is assumed to represent the externally applied force density.

5.2 Definition of $\underline{f}_{\text{ext}}$

The specific distributions of $\underline{f}_{\text{ext}}$ on actuator surfaces are described here. As far as the 3-D disc is concerned, the restriction is made that azimuthal force components are absent (except in section 7.1). As a consequence, also the azimuthal velocity component is zero, so the force field and flow field are completely described in a meridional plane through the disc axis. Figure 5.1 shows a cross-section through such a disc, or through a 2-D strip. Also shown is the local cartesian coordinate system (x,y) in the plane of the cross-section. The x -coordinate is normal to the surface. The thickness of the surface is ϵ . The distribution of $\underline{f}_{\text{ext}}$ is assumed to be smooth, with :

$$\begin{aligned} \underline{f}_{\text{ext}} &= \underline{e}_x f_{\text{ext}} & \text{for } |x| < \epsilon/2 \\ \underline{f}_{\text{ext}} &= 0 & \text{for } |x| \geq \epsilon/2 \end{aligned} \quad (5-7)$$

The distribution of \underline{f} is such that $\int \underline{f}_{\text{ext}} dx$ across the surface equals F , irrespective of the thickness ϵ . This implies that the distribution becomes a delta function for $\epsilon \rightarrow 0$:

$$\underline{f}_{\text{ext}} = \underline{e}_x F \delta(x) \quad \text{for } \epsilon \rightarrow 0 \quad (5-8)$$

where $\underline{F} = \underline{e}_x F$ is the normal surface load.

The distribution of \underline{F} along the surface determines the type of flow. A particular distribution is \underline{F} being constant on the surface with a step function at the edges. This is the subject of chapter 8; the other chapters deal with smooth distributions.

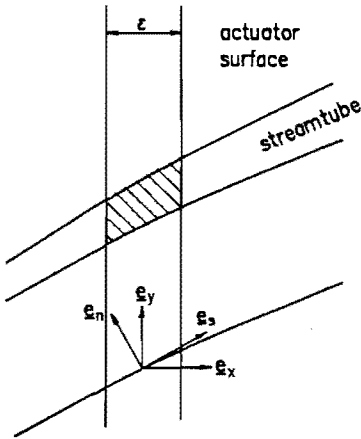


Figure 5.1. Cross section through an actuator surface

5.3 Dimension analysis of actuator surface flow

In section 5.1 the equation of motion (5-5) is considered to be the result of the Navier-Stokes equation for vanishing viscosity, expressed by $Re \rightarrow \infty$, which requires that it is possible to define such a Reynolds number. If we consider infinitely thin surfaces with semi-infinite length, the surface does not have a length scale. Therefore it is not obvious if it is possible to define a Reynolds number for such surfaces.

This problem is treated first.

The semi-infinite actuator strip

Suppose we have a semi-infinite actuator strip having thickness ϵ , loaded with a surface distribution with characteristic strength \underline{F} . The flow is viscous. An undisturbed parallel flow U_0 may be present. The available parameters are: ϵ [m], \underline{F} [kg/ms^2], the fluid density ρ [kg/m^3], the kinematic viscosity ν [m^2/s] and, if present, the velocity U_0 [m/s]. It is always possible to define a second scale:

$$u = \sqrt{\frac{2F}{\rho}} \quad , \quad (5-9)$$

so it is possible to define

$$\text{Re}_\epsilon = \frac{\epsilon}{\nu} \sqrt{\frac{2F}{\rho}} \quad \text{or} \quad \frac{\epsilon}{\nu} U_0 \quad . \quad (5-10)$$

If there is no undisturbed flow U_0 , it is clear that a necessary condition for inviscid flow induced by semi-infinite strips with zero thickness ϵ is that the ratio ϵ/ν becomes infinite if the limits $\epsilon \rightarrow 0$ and $\nu \rightarrow 0$ are taken. Schmidt & Sparenberg [1977, see also section 8.3.1] discuss the flow induced by an infinitely thin actuator strip with semi-infinite length, with $U_0 = 0$. They assume the flow to be inviscid, by which ϵ/ν is implicitly assumed to be infinite. In order to avoid such an implicit assumption we proceed in the remainder of this thesis from a surface having a finite thickness ϵ placed in a fluid with zero kinematic viscosity ν , after which the limit $\epsilon \rightarrow 0$ is taken.

One exception to this treatment is made: in appendix C we discuss the alternative sequence of limits for the flow induced by a semi-infinite strip in absence of an undisturbed flow: the thickness ϵ is assumed to be zero before the limit $\nu \rightarrow 0$ is taken. Then the independent parameters are F [kg/ms²], ρ [kg/m³] and ν [m²/s]. Although the strip does not have a characteristic dimension, still a length scale ℓ is available:

$$\ell = \sqrt{\frac{\rho\nu^2}{2F}} \quad , \quad (5-11)$$

but an independent velocity scale cannot be defined. If the velocity scale (5-9) is used, we do not have an independent length parameter. Therefore it is not possible to define a Reynolds number, by which it is impossible to define inviscid flow.

The viscous solution is presented in appendix C. The generation and diffusion of vorticity is determined by the non-dimensional ratio $r^2/(\nu t)$, where r is the distance from the strip edge and t the time parameter. Letting $\nu \rightarrow 0$ results in a rescaling of the solution: for very small r or very large t the viscous diffusion becomes finite.

The actuator surface with finite dimension

If the actuator surface has a finite dimension L , it is always possible to define a Reynolds number, using the velocity scale (5-9):

$$\text{Re}_L = \frac{L}{\nu} \sqrt{\frac{2F}{\rho}} \quad (5-12)$$

The value of Re_ϵ can be expressed in the shear stress term in the Navier-Stokes equation (5-1). This term is rewritten as $\nu \nabla^2 \underline{v} = -\nu \nabla \times \underline{\omega}$ using the continuity equation (5-2). For streamlines which exhibit a finite increase of vorticity $\Delta \underline{\omega}$ on passing the surface, the average value of $-\nu \nabla \times \underline{\omega}$ is:

$$-\nu \overline{\nabla \times \underline{\omega}} = -\frac{\nu}{\epsilon} \int_{\epsilon} \nabla \times \underline{\omega} \, dx = O\left[\frac{\nu}{\epsilon}\right] = O\left[\text{Re}_\epsilon^{-1}\right], \quad (5-13)$$

where x is the coordinate normal to the surface, see figure 5.1. The necessary conditions for (5-13) to be valid are that the streamlines are not tangent to the surface, and that the increase of vorticity on the streamlines is finite. Then (5-13) shows that the non-viscous term in the Navier-Stokes equation (5-1) is of $O(\nu/\epsilon)$. As a consequence inviscid flow cannot be defined by the limit $\text{Re}_L \rightarrow \infty$ alone if the thickness $\epsilon \rightarrow 0$: then also the ratio ν/ϵ needs to be known.

Equation (5-13) does not determine whether the viscous term is finite or not. This becomes clear only after evaluation of $\underline{f}_{\text{shear stress}}$ for each specific flow case, as we will do in chapters 7 and 8.

Finally the relation between the Reynolds number and the dimensionless thrust coefficient C_T , defined in (3-11), is discussed. We assume an undisturbed velocity U_0 to be present. Using the length scale (5-11) the Reynolds number is defined as $\text{Re}_\ell = \ell U_0/\nu$. Substitution of (5-11) relates this Reynolds number to the thrust coefficient:

$$C_T = \frac{F}{\frac{1}{2}\rho U_0^2} = \frac{1}{\text{Re}_\ell^2} \quad (5-14)$$

Only in the trivial case of $C_T = 0$, Re_ℓ becomes infinite. In all other cases it is finite, which implies that $O(\ell) = O(\nu)$.

Also a second length scale can be defined:

$$\kappa = \frac{\nu}{U_0} \quad (5-15)$$

The thrust coefficient C_T equals the ratio of the square of the two length scales: $C_T = (\kappa/\ell)^2$. It determines the possibility of linearization of the flow equations, which is not treated here.

Chapter 6

NUMERICAL ANALYSIS OF THE ACTUATOR STRIP FLOW

This chapter consists of two parts: the numerical methods and results found in literature are discussed briefly, and calculations performed within the framework of this thesis are presented. All methods concern 2-D flows. The only 3-D, non-linear calculations known to the author have been carried out by Greenberg [1972]. The results for the actuator disc with constant, normal load show the same features, qualitatively as well as quantitatively, as the 2-D results of Lee & Greenberg [1984] which are discussed here.

The methods of Madsen [1985,1988], Lee & Greenberg [1984] and Schouten [1983] have in common that the flow is treated as inviscid, and that the surface is infinitely thin; the results are plotted in figure 2.5. Our calculations are reported in detail in Peters [1989] and concern flows with a finite Reynolds number, while the surface has a non-zero thickness. By increasing the Reynolds number and decreasing the thickness it is attempted to establish the inviscid limit for infinitely thin surfaces.

6.1. Inviscid calculations

6.1.1 The actuator cylinder of Madsen [1985,1988]

Madsen calculated the 2-D flow through an actuator cylinder (see section 2.2). He assumes a normal force density distribution on a circle, in such a way that no discontinuities are present. As singularities are avoided by doing so, the problem is suitable for an iterative solution on a orthogonal grid.

Madsen introduces the perturbation velocity \underline{y}^* which is related to the undisturbed velocity \underline{U}_0 in x -direction and the local velocity \underline{y} by:

$$\underline{v}^* = \underline{v} - \underline{U}_0 \quad (6-1)$$

The equation of motion (5-5) then becomes:

$$\rho U_0 \frac{\partial \underline{v}^*}{\partial x} = -\underline{\nabla} p + \underline{f} - \rho (\underline{v}^* \cdot \underline{\nabla}) \underline{v}^* \quad (6-2)$$

According to von Karman & Burgers [1935] the last term is interpreted as the induced or second-order force \underline{g} . The divergence of (6-2) combined with the conservation of mass (5-2) yields a Poisson-equation for p :

$$\nabla^2 p = \underline{\nabla} \cdot \underline{f} + \underline{\nabla} \cdot \underline{g} \quad (6-3)$$

Since this equation is linear it is equivalent with:

$$\begin{aligned} p &= p_f + p_g \\ \nabla^2 p_f &= \underline{\nabla} \cdot \underline{f} \\ \nabla^2 p_g &= \underline{\nabla} \cdot \underline{g} \end{aligned} \quad (6-4)$$

The linear solution p_f is obtained easily if the distribution of \underline{f} is known. This linear solution is used for the first approximation of \underline{v}^* , with which \underline{g} is known, and a second approximation can be made, etc.

A drawback of this method is that convergence problems are encountered if the

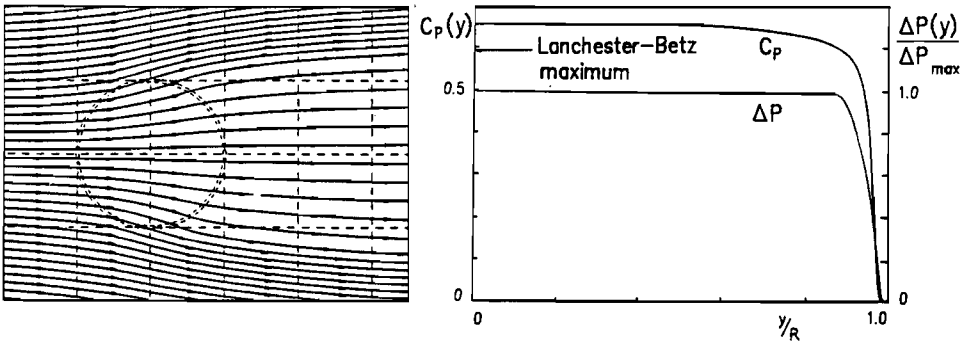


Figure 6.1. The resultant load distribution and the flow field of Madsen's actuator cylinder.

gradients of the force field distribution are steep. Figure 6.1 shows the maximum attainable force distribution which yielded a convergent solution. The distribution shown is the resultant distribution in undisturbed flow direction, being the summation of the upstream and downstream side of the cylinder. The results exceed the classical momentum theory results for constant distributions: the power coefficient $C_P = 0.616$ is higher than the maximum value (0.593) predicted by this theory. The thrust coefficient $C_T = 0.98$, while the average flow through the cylinder $\bar{u}/U_0 \approx 0.63$. The accuracy of the computation is indicated by Madsen in terms of deviation of the mass balance (0.20%) and the axial momentum balance (0.57%). Nothing is said about numerical dispersion. If this should be significant, it can be considered as a numerical viscosity.

6.1.2 The actuator strip of Lee & Greenberg [1984]

The strip of Lee & Greenberg induces an acceleration of the flow. Emphasis will be given to the hover case, for which the undisturbed flow is zero. The equation to be solved numerically is (8–18) in section 8.3.2. In this section also the built-in edge singularity is discussed. The strip has a constant, normal load, so each strip edge sheds a vortex sheet into the flow. The strength and shape of the sheet are the unknowns. The boundary conditions are: the sheet has to be a streamline (a kinematical

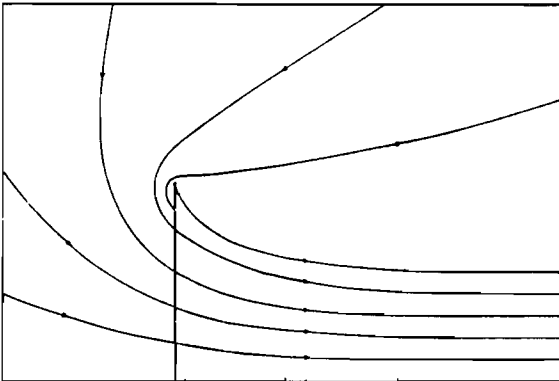


Figure 6.2. The actuator strip flow in hover, Lee & Greenberg [1984]

condition), and the pressure jump across the sheet must be zero (a dynamical one). By assuming a set of suitable chosen basic functions describing the strength and shape of the sheet, and applying the boundary conditions at several collocation points, the coefficients of these functions are calculated iteratively. One of the strength functions contains the square-root edge singularity. Figure 6.2 shows the resulting flow field for the hover case. The accuracy is specified by the deviation from the two boundary conditions. Both are said to be satisfied "at a large number of x-points" within 0.1%.

As we will show in section 8.3.2, the square root singularity is not correct: it cannot satisfy the dynamical boundary condition. However, as this singularity is integrable, the far-field effect will be the same as that of a discrete vortex which is the type of singularity we propose in section 8.1. Except in the region close to the edge, the flow field remains the same whether the edge singularity is such a discrete vortex or a vortex sheet square root singularity with an equivalent strength. In Lee & Greenberg's calculations the boundary conditions are satisfied except close to the edge, so the strength of the singularity is considered to be appropriate. The square root singularity is always connected with a suction force which, in case of the actuator strip, manifests itself as an edge force. Therefore we can perform a quantitative check of the momentum theory including edge forces, using the data of Lee & Greenberg for the hover case ($U_0 = 0$). These data are sufficient to determine the edge force. Having done this, the momentum theory of chapter 3 provides a prediction of the velocity in the far wake, which can be compared with the numerical result of Lee & Greenberg.

They calculate the ratio of the average velocity through the strip \bar{u}_{strip} to the average velocity in the far wake \bar{u}_∞ to be 0.5535, while the prediction of the classical momentum theory amounts 0.5. The prediction of this ratio by the momentum theory including edge forces is given by (3-9), which is rewritten as:

$$\frac{\bar{u}_{\text{strip}}}{\bar{u}_\infty} = 0.5 \frac{T}{T_{\Delta H}} = 0.5 \left[1 + \frac{\bar{F}_{\perp \psi, ax}}{\Delta p R} \right]. \quad (6-5)$$

Here Δp is the pressure jump across the strip. T is the total thrust in x-direction, and $T_{\Delta H} = \Delta p 2R$ the total thrust minus the contribution of the edge forces $\bar{F}_{\perp \psi, ax}$. The length of the strip is $2R$. The radial component of the edge force is known by substituting the data of Lee & Greenberg (see figure 6.3) in (3-8): $\bar{F}_{\perp \psi, rad}/(\Delta p R) = -0.205$. Since the direction of the vortex sheet near the edge is given by Lee & Greenberg, the ratio of the axial and radial components of $\bar{F}_{\perp \psi}$ is known: the suction force at a square root singularity is tangent to the sheet.

Then $\bar{F}_{\perp\psi,ax}$ is known and (6-5) predicts $\bar{u}_{strip}/u_{\infty}$ to be 0.5454, which agrees very well with the numerical result 0.5535. Therefore the discrepancy, mentioned by Lee & Greenberg, between their numerical result and the momentum theory result is only apparent: the use of a square root singularity implies the presence of edge forces, which on its turn implies that the momentum theory accounting for these forces should be used to compare with, instead of the classical theory. As shown above, this comparison does not show a discrepancy.

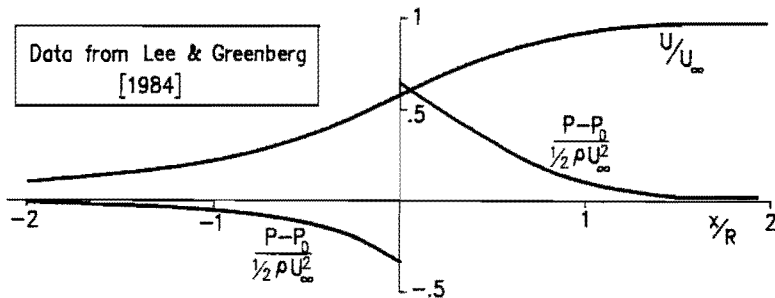


Figure 6.3. Velocity and pressure on the symmetry line of the actuator strip.

6.1.3 The actuator strip of Schouten [1983]

Schouten performed a calculation including an undisturbed flow U_0 with a strip load $\Delta p = 2\rho U_0^2$, using a method similar to the one of the previous section. An important difference is the choice of the edge singularity: Schouten assumes the Schmidt & Sparenberg spiral, discussed in section 8.3.1. In the calculations it is replaced by a discrete vortex, merely as a convenient representation of this semi-infinite spiral. The result is shown in figure 6.4. The classical momentum theory predicts $R_w/R = 0.6$. Schouten finds 0.6094; the deviations by ongoing iterations are 6×10^{-6} . Schouten's result can be interpreted only if edge forces are assumed to be present, unless numerical inaccuracies cause the difference with the classical result. This is suggested by Schouten himself.

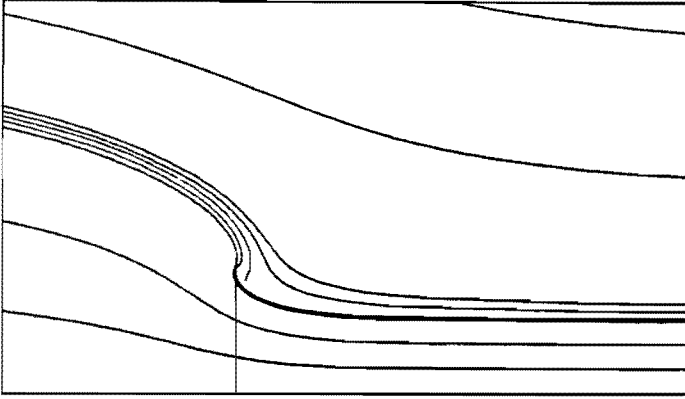


Figure 6.4. The actuator strip according to Schouten [1983]

6.2. Viscous calculations (Peters [1989])

Peters' numerical analysis of the actuator strip and disc flow proceeds from a different starting point: a standard finite element computer code (SEPRAN) is used to calculate the flow induced by smooth distributions of \underline{f} on a surface with finite thickness ϵ . By increasing the Reynolds number and the gradient of \underline{f} near the edge, and decreasing the thickness as far as the code permits, the inviscid, infinitely thin surface is approached. The equation of motion is (5-1), the Navier-Stokes equation with the force density term $\underline{f}_{\text{ext}}$ added. The force field $\underline{f}_{\text{ext}}$ is defined by (5-7) and (5-8). The undisturbed flow is zero: $U_0 = 0$. The method is illustrated using the strip calculations; the disc results reported in Peters [1989] show the same features.

6.2.1 The force distribution and the definition of the Reynolds number.

Figure 6.5 shows the (x,y) coordinate system. The width of the strip is $L = 1$; by reasons of symmetry, all figures show the upper half plane, in which $y = L/2$ denotes the strip edge. The distribution of $\underline{f}_{\text{ext}}$ is given by:

$$f_{\text{ext}} = e_x F \left[g(x), h(y) \right]$$

with
$$g(x) = \frac{m}{2 \cosh^2(mx/L)} \tag{6-6}$$

$$h(y) = \frac{1}{2} \left[1 - \tanh \left[\left| \frac{y}{L} \right| - \frac{1}{2} \right] \right] .$$

The distribution functions g and h are shown in figure 6.6 for $m = 17$. m is called the steepness parameter. For $m \rightarrow \infty$, $h \rightarrow 1$ for $y \leq L/2$ and $h \rightarrow 0$ for $y > L/2$. For all m the same resultant force is obtained: with A as the area on which f is distributed:

$$\iint_A f_x dA = F L \quad \text{for all } m . \tag{6-7}$$

For finite m , the definition of the strip length is not unambiguous. Included in (6-6) is a definition of L independent of m : $L/2$ equals the y value of the point where $h(y)=0.5$. The thickness ϵ of the strip is defined in an analogous way: it is the distance in x -direction between the points where $g(x) = 0.5 g(0)$:

$$\frac{\epsilon}{L} = \frac{2}{m} \operatorname{arccosh}(\sqrt{2}) . \tag{6-8}$$

For infinite m , the thickness ϵ becomes zero and the distribution function g becomes

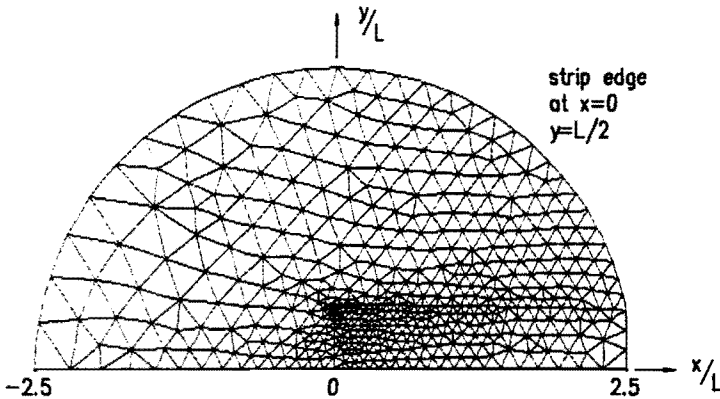


Figure 6.5 The computational grid used for $m = 17$, $Re_L = 2594$

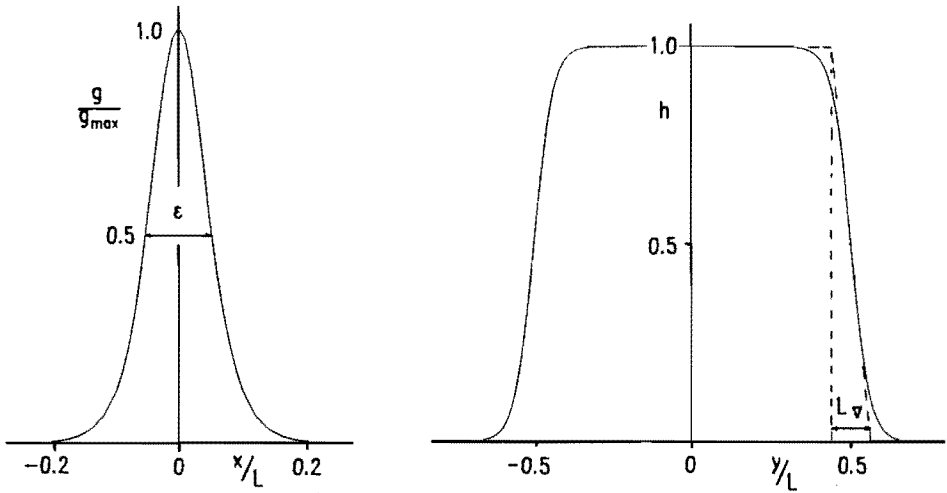


Figure 6.6 The force density distribution in x -direction (left) and y -direction (right) for $m = 17$

an approximation of a delta function. In this way, m determines the gradients of the distribution and the strip thickness at the same time: for increasing m , ϵ equals the "gradient length" L_v shown in figure 6.6. The ratio L_v/L is :

$$\frac{L_v}{L} = \frac{2}{m} \quad (6-9)$$

The Reynolds numbers defined in section 5.3 are:

$$\begin{aligned} \text{Re}_L &= \frac{u_\infty L}{\nu} \\ \text{Re}_\epsilon &= \frac{u_\infty \epsilon}{\nu} = \frac{2}{m} \text{arccosh}(\sqrt{2}) \text{Re}_L \end{aligned} \quad (6-10)$$

where u_∞ is the ultimate slipstream velocity at the strip centerline in inviscid theory. Using Bernoulli's law it is clear that $u_\infty = \sqrt{(2F/\rho)}$, by which u_∞ is seen to coincide with the velocity scale (5-9) in the dimension analysis of section 5.3.

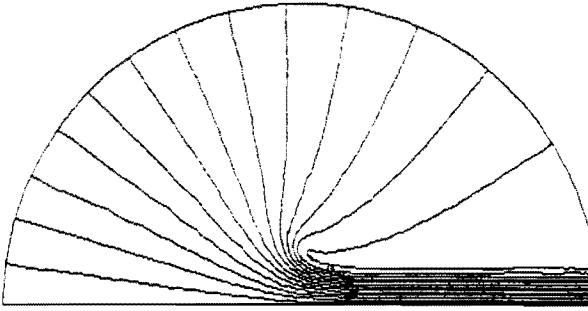


Figure 6.7 The flow for $m = 17$, $Re_L = 2594$

6.2.2 The computational method

Making the velocity dimensionless with u_w , the pressure with ρu_w^2 , and the force density with $\rho u_w^2/L$, the Navier Stokes equation becomes:

$$(\underline{v} \cdot \nabla) \underline{v} = \underline{f} - \nabla p + \frac{1}{Re_L} \nabla^2 \underline{v} , \tag{6-11}$$

where all variables are to be interpreted as dimensionless. The method of solving (6-11) is an iterative one: the n -th approximation $(\underline{v})_n$ of the flow field is determined using the previous approximation $(\underline{v})_{n-1}$. The non-linear convective term in (6-11) is linearized using the so-called Newton iteration. As starting solution $(\underline{v})_0$ the convective term is put zero. The iteration is stopped when the relative error $(\underline{v}_n - \underline{v}_{n-1})/\underline{v}_n$ is smaller than 10^{-6} . In order to achieve a high Reynolds numbers solution, the converged solution of a lower Reynolds number is used as starting solution. For each value of m and the desired Reynolds number, also a series of solutions is found for different Reynolds numbers, all smaller than the desired one. The highest attainable values of m and Re_L are 17 and 2600 respectively. For higher Re-numbers instabilities were encountered.

Figure 6.5 shows the computational domain and the finest grid used. The radius of the circle is chosen as $2.5L$, since the wake is expected to be fully developed then. The boundary conditions are: at the circular boundary, the velocity component tangential

to the circle is zero; at the line of symmetry, the normal component v and the derivative $\partial u/\partial y$ are zero.

The method uses Crouzeix-Raviart elements with 1 calculation point for the pressure and 7 for the velocity on each element. The equations for the pressure and velocity are disconnected by means of a penalty function method. The pressure is calculated afterwards from the velocity field (Segal [1987]).

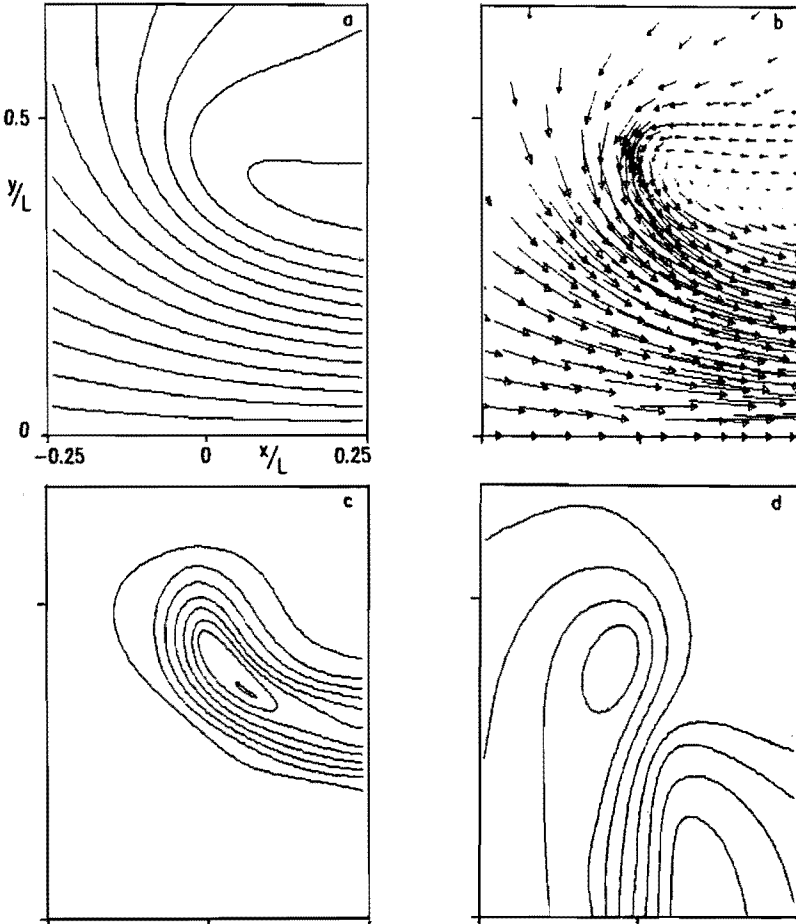


Figure 6.8 Details of the flow for $m = 17$, $Re_L = 2594$. a: streamlines b: velocity vectors
c: lines with constant vorticity d: lines with constant pressure

6.2.3 Results for $m=17$, $Re_L \rightarrow \infty$

Figure 6.6 shows the force distribution for $m = 17$. The thickness ϵ is $\approx 0.1 L$. The grid used is shown in figure 6.5. The Reynolds number Re_L is 2594, by which $Re_\epsilon = 269$.

Figure 6.7 shows the streamlines; enlarged sketches of details near the strip are shown in figures 6.8a through d. The momentum balance in x direction is satisfied within 0.3% of the total thrust; the balance in y direction shows errors of 1%. The mass balance is satisfied within $10^{-4}\%$.

The power P , needed to accelerate the flow, is obtained by calculating $\iint \underline{f} \cdot \underline{y} \, dx dy$, and compared with the power predicted by the classical momentum theory, $P_{classical}$.

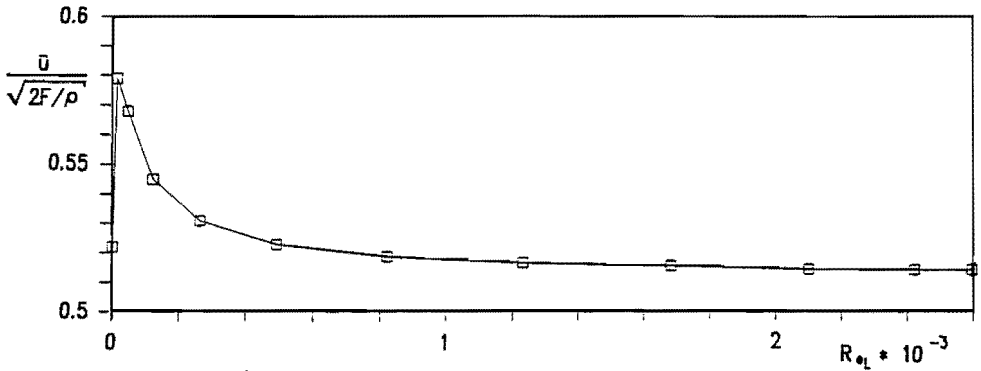


Figure 6.9 Average velocity at the strip, for $m = 17$ as a function of Re_L

The influence of Re_L is shown in figure 6.9: for $Re_L > 1000$ the value of average strip velocity is practically independent of the Reynolds number. Figures 6.10a/b support this conclusion: the distribution of vorticity is hardly affected by doubling Re_L . The value of $P / P_{classical}$ for infinite Re_L is obtained by plotting $P / P_{classical}$ against Re_L^{-1} , see figure 6.11. Linear extrapolation then yields: $P / P_{classical} = 0.9901$ for $m = 17$ and $Re_L \rightarrow \infty$.

6.2.4 Extrapolation towards infinite m

Figure 6.12 shows a survey of all values of $P / P_{classical}$ as a function of m and the grid used. The values shown are the extrapolated values for $Re_L \rightarrow \infty$. Grid 1 is the roughest grid, grid 3 is the finest grid which is shown in figure 6.5. It is clear that increasing m requires a finer grid in order to avoid numerical dispersion; below a

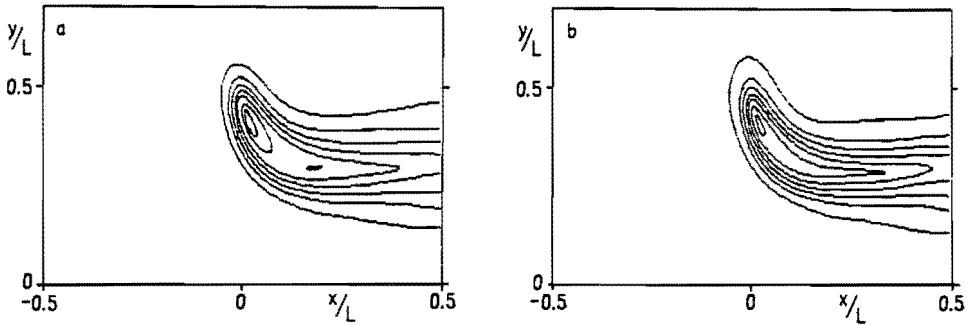


Figure 6.10 Vorticity distribution for $m = 17$, $Re_L = 1231$ (a) and $Re_L = 2594$ (b)

certain m , there is no need to use a refined grid: for $m < 7$ grid 1 and 2 yield the same results, as do grid 2 and 3 for $7 \leq m \leq 12$.

The data of the $Re_L \rightarrow \infty$ extrapolations for $m = 10, 13, 15$ and 17 on grid 3 are used to obtain an extrapolation for $m \rightarrow \infty$. A curve fit using $P / P_{\text{classical}} = c_1 \exp(c_2/m)$ then yields 1.02 as the probable value for infinite m . The accuracy of this extrapolation is limited by several effects. Variation of the grid size R for $m = 10$ showed a 0.7% decrease of power if R / L is increased from 2.5 to 4. Furthermore the data for the m

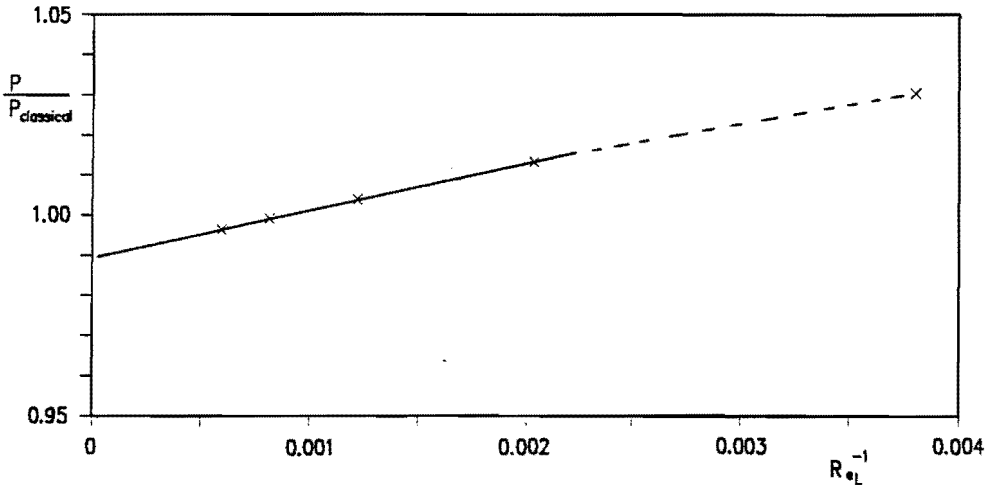


Figure 6.11 Extrapolation of the power P , $m = 17$, for $Re_L \rightarrow \infty$

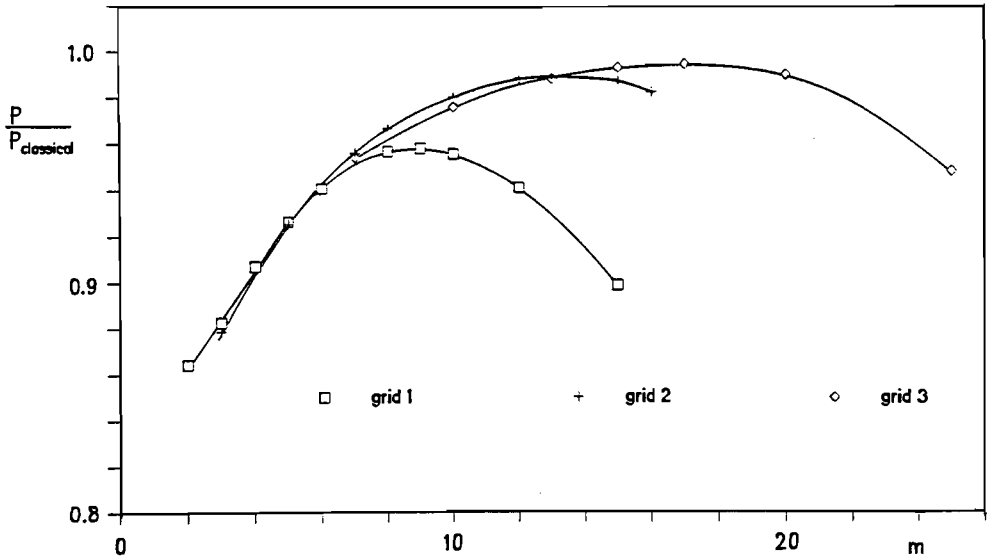


Figure 6.12 P/P_{cl} for all m , extrapolated for $Re \rightarrow \infty$

values used may be sensitive for the grid itself. For $m = 17$ the distribution and the size of the grid cells near the edge were refined. This decreased the result about 1%. Using the available data, the best possible extrapolation for infinite m and Re_L leads to the following estimation:

$$P/P_{\text{classical}} = 1.01 \pm 0.02 \quad (6-12)$$

The main drawback of this extrapolation is the limited number of data points. Of all numerical methods discussed in the previous section, the method of Madsen comes closest to the present one, as the distribution of F is smooth. Madsen finds for his actuator cylinder $P / P_{\text{classical}} \approx 1.05$ which is not compatible with (6-12). Apart from differences in flow state (Madsen's flow is decelerating instead of accelerating; a cylinder is used instead of a strip) an explanation may be found in the equivalent m value of Madsen's calculation. His distribution function is shown in figure 6.1, and is given in Madsen [1985]. The maximum of $d(F/F_{\text{max}})/dy$ is ≈ 16.9 . Referred to the same scale as used in figure 6.6a, where $y \approx 0.7$ agrees with $y = 1.0$ of figure 6.1, this maximum derivative is about 2.8 times the maximum derivative for $m = 17$ in our method. As this derivative is proportional with m according to (6-9), the equivalent m

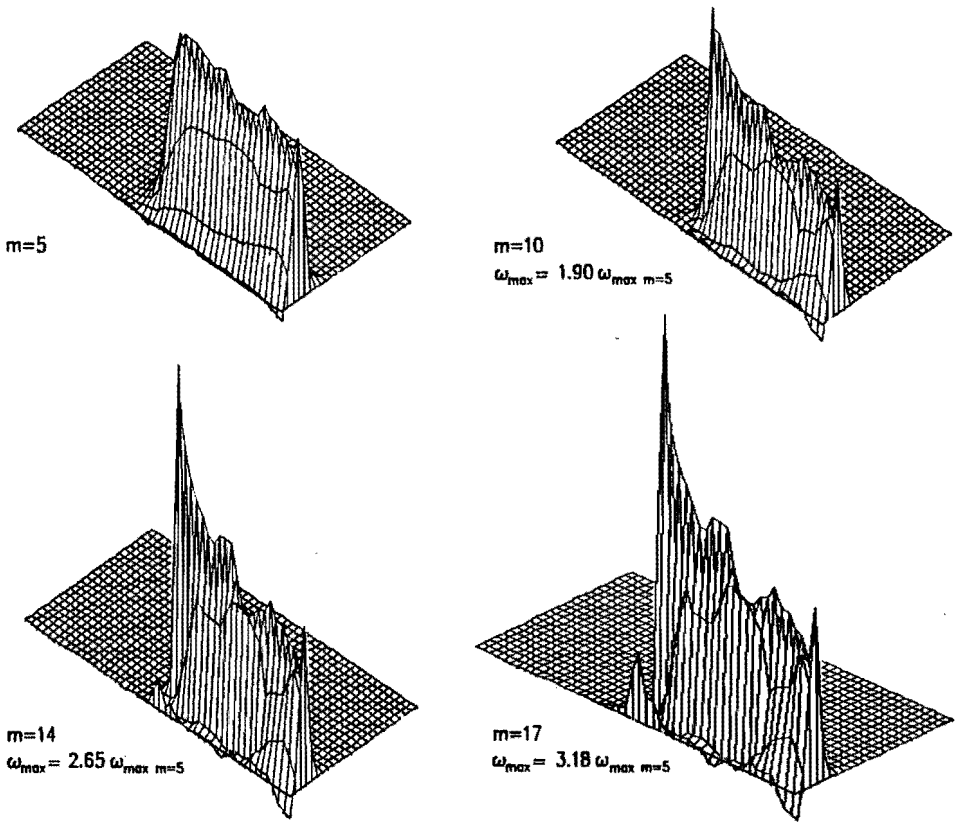


Figure 6.13 Vorticity distribution for different values of m

of Madsen's distribution is approximately 46. This may explain the differences in results of both methods; at the same time this confirms the restricted value of (6-12). Finally the change in vorticity distribution as a function of m is shown in figure 6.13. The maximum vorticity increases 300% in passing from $m = 5$ to $m = 17$. For $m = 17$, the location of the point with maximum vorticity is $x \approx 0$, $y \approx 0.4$ while for smaller m this location is downstream of the strip. A singularity at the strip edge in case of infinite m , which is expected according to chapter 8, is compatible with the tendency of figure 6.13.

6.2.5 The interpretation of the strip experiment of Lee & Greenberg [1984]

As already mentioned in section 2.2, Lee & Greenberg performed an actuator strip experiment without undisturbed flow: $U_0 = 0$. The general description is given there;

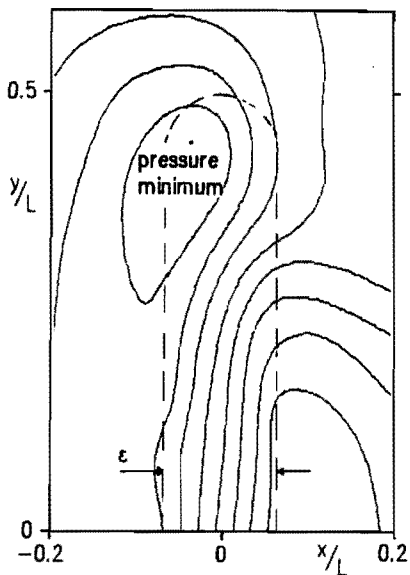


Figure 6.14 Isobars for $m = 14$, $Re_L = 2594$

the interpretation of the results is presented here. The typical Reynolds number $\frac{L}{\nu} \sqrt{2F/\rho}$ was of order 10^5 , where L is the strip length. The equivalent thickness of the strip corresponds with the 'merging length' of the jets: the length in which the momentum is transferred to the ambient flow by diffusion of the jets. According to Lee & Greenberg this length is about $0.4L$. We compared our numerical results for $m = 14$ and $Re_L = 2600$ with these experiments. For $m = 14$ the thickness of the strip is $\approx 0.13L$ according to (6-8). Lee & Greenberg observed pressure minima at the location: $L/30$ downstream of the injection line and $L/20$ inboard of the edge. Peters found this minimum pressure to occur at $L/40$ downstream of the upstream side of the strip and $L/20$ inboard of the edge (figure 6-14). The flow field at the strip itself is compared in figure 6-15, which show a much better agreement than Lee & Greenberg's numerical result. The average velocity through the strip is 3.5% higher than the value .5, expected by the classical momentum theory.

Comparison at a downstream distance L shows large discrepancies which, as noted by Lee & Greenberg, are probably due to turbulence.

The conclusion of this numerical interpretation of the strip experiments is that calculations with a finite thickness and a smooth force distribution improve the agreement with the experimental data considerably. Although the experiment was intended to simulate a strip with constant load, probably a more gradual distribution is realized physically which explains this improved correlation. Lee & Greenberg's conclusion that the position of the pressure minima determine an effective strip length of about $0.9L$ is unnecessary. Their main reason for introducing this reduced length was to remove the 10% discrepancy between their numerical results and momentum theory results. As already noted in section 6.1.2, this discrepancy has its origin in comparing with a momentum theory excluding the presence of edge forces, while their numerical model introduces edge forces.

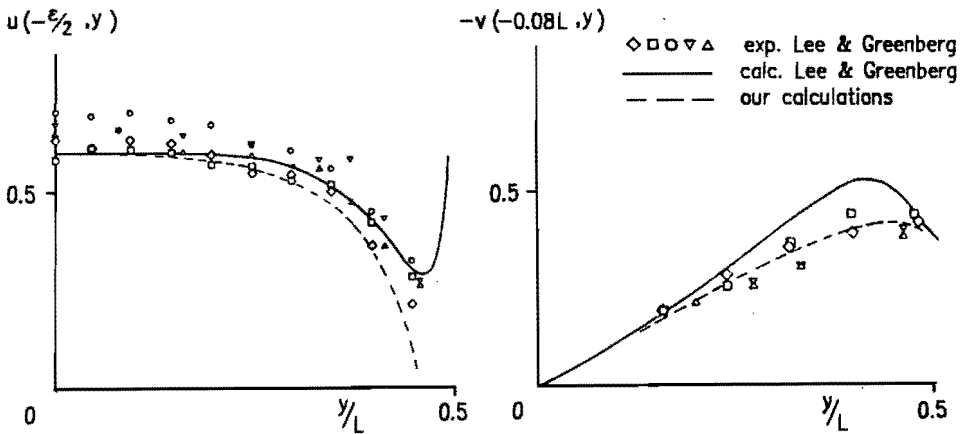


Figure 6.15 Comparison of the experimental and numerical results of Lee & Greenberg with the results for $m = 14$, $Re_L = 2594$.

Chapter 7

THE GENERATION OF VORTICITY BY FORCE FIELDS

This chapter contains the first part of our analytical study towards the actuator strip/disc flow. The second part is presented in Chapter 8. From a kinematical point of view, the main feature of such a flow is the generation of vorticity by the strip/disc load, and we derive the relation between force and flow field for two specific cases: the flow through an actuator disc which is derived as an exact solution of Wu's [1962] equation, and the flow through an actuator surface with a smooth load distribution. The equation of motion is the steady version of (5-5):

$$\nabla H = \underline{f} + \rho \underline{v} \times \underline{\omega} \quad (7-1)$$

and the continuity equation (5-2). The distribution of the force density satisfies (5-4), where f_{ext} is the externally applied force density (5-7/8), and $f_{\text{shear-stress}}$ the force density resulting from viscosity. This term is unknown a priori. As in Chapter 5 we use the word surface to denote a strip or disc if the distinction is of no importance.

7.1. The force density f in Wu's equation illustrated by an exact solution

The actuator disc problem is treated thoroughly by Wu [1962]. He considers actuator discs placed normal to the undisturbed flow U_0 , having an axisymmetric but otherwise arbitrary load distribution. The angular velocity of the disc is Ω . The coordinate system is the cylindrical system (x, r, φ) with the origin at the disc center. The flow field induced by the force field is also axisymmetric, so it is possible to use the 3-D Stokes streamfunction ψ . This is the vector potential of \underline{v}_s , the velocity in a meridional plane (each plane containing the axis $r = 0$), so $\underline{v}_s = \nabla \times \underline{e}_\varphi \psi / r$ (see e.g. Batchelor [1970], page 79). Together with the azimuthal velocity component v_φ , ψ describes the

flow field completely. Using the definition for the circulation $\Gamma = 2\pi r v_\varphi$ instead of v_φ itself, Wu's equation describing the flow through an actuator disc is:

$$\frac{\partial^2 \psi}{dx^2} + \frac{\partial^2 \psi}{\partial r^2} - \frac{1}{r} \frac{\partial \psi}{\partial r} = \frac{\partial \Gamma / 2\pi}{\partial \psi} (\Omega r^2 - \frac{\Gamma}{2\pi}) - \frac{r}{\rho} \frac{f_{\perp} \psi}{v_s} \quad (7-2)$$

The last term contains $f_{\perp} \psi$, which is the force density component normal to the streamtube. The derivation of (7-2) is repeated here.

The vorticity ω_φ is expressed in two ways. The first relation uses the kinematical relationship $\omega_\varphi = \mathbf{e}_\varphi \cdot (\nabla \times \mathbf{v}) = \mathbf{e}_\varphi \cdot (\nabla \times \nabla \times \mathbf{e}_\varphi \psi / r)$, which becomes after evaluation:

$$\begin{aligned} \omega_\varphi &= -\frac{\partial}{\partial r} \left(\frac{1}{r} \frac{\partial \psi}{\partial r} \right) - \frac{1}{r} \frac{\partial^2 \psi}{\partial x^2} \\ &= -\frac{1}{r} \left(\frac{\partial^2 \psi}{\partial x^2} + \frac{\partial^2 \psi}{\partial r^2} - \frac{1}{r} \frac{\partial \psi}{\partial r} \right) \end{aligned} \quad (7-3)$$

The second relation is obtained using the component of (7-1) which lies in the meridional plane, and is normal to the streamtube. We use a local cartesian coordinate system (s,n) in this plane, with s tangential to the streamline and n perpendicular to it. The unit vectors are \mathbf{e}_s and \mathbf{e}_n respectively. Then this component reads:

$$\rho \frac{\partial H}{\partial n} = \mathbf{e}_n \cdot \mathbf{f} - \rho v_s \omega_\varphi + \rho v_\varphi \omega_x \quad (7-4)$$

The terms $\frac{\partial H}{\partial n}$ and ω_x are rewritten as:

$$\begin{aligned} \omega_x &= \frac{1}{r} \frac{\partial (r v_\varphi)}{\partial r} = \frac{1}{r} \frac{\partial \psi}{\partial r} \frac{\partial (r v_\varphi)}{\partial \psi} = u \frac{\partial (r v_\varphi)}{\partial \psi}, \\ \frac{\partial H}{\partial n} &= \frac{\partial H}{\partial \psi} \frac{\partial \psi}{\partial n} = \frac{\partial H}{\partial \psi} r v_s, \end{aligned} \quad (7-5)$$

where we have used $v_s = \mathbf{e}_s \cdot (\nabla \times \mathbf{e}_\varphi \psi / r) = \frac{1}{r} \frac{\partial \psi}{\partial n}$. Substitution of (7-5) into (7-4) yields the second expression for ω_φ . Writing $\mathbf{e}_n \cdot \mathbf{f}$ as $f_{\perp} \psi$ and $v_\varphi r$ as $\Gamma / 2\pi$ this becomes:

$$\omega_{\varphi} = -\frac{r}{\rho} \frac{\partial H}{\partial \psi} + \frac{\Gamma}{2\pi r} \frac{\partial(\Gamma/2\pi)}{\partial \psi} + \frac{1}{\rho} \frac{f_{\perp} \psi}{v_s} . \quad (7-6)$$

Finally H has to be expressed in Γ . The power produced by an element of the actuator disc is $(\underline{f} \cdot \underline{v}) \pi r^2$, which must equal $\Omega dQ = \Omega f_{\varphi} r \pi r^2$. Therefore:

$$\underline{f} \cdot \underline{v} = \Omega r f_{\varphi} . \quad (7-7)$$

The dot product of (7-1) with \underline{v} yields a second expression for $\underline{f} \cdot \underline{v}$:

$$\underline{f} \cdot \underline{v} = (\underline{v} \cdot \underline{\nabla}) H . \quad (7-8)$$

The φ -component of (7-1) reads $f_{\varphi} = -\rho (v_x \omega_r - v_r \omega_x)$. Both vorticity components are a function of v_{φ} : ω_x is given in (7-5), while ω_r equals $-\partial v_{\varphi} / \partial x$. Then f_{φ} becomes:

$$\frac{1}{\rho} f_{\varphi} = \frac{1}{r} (\underline{v} \cdot \underline{\nabla}) (rv_{\varphi}) = \frac{1}{2\pi r} (\underline{v} \cdot \underline{\nabla}) \Gamma . \quad (7-9)$$

The combination of (7-7) through (7-9) yields:

$$\frac{1}{\rho} (H - H_0) = \Omega \frac{\Gamma}{2\pi} , \quad (7-10)$$

with $H = H_0$, $\Gamma = 0$ upstream of the disc, and downstream but outside the wake. The combination of (7-10), (7-3) and (7-6) finally gives Wu's equation (7-2).

The term $f_{\perp} \psi$ is non-zero only at the disc itself. Wu suggests that this force term may be neglected, as it should be the component of the axial force density normal to the streamtube. A significant value of $f_{\perp} \psi$ then requires a large radial velocity component at the disc, which is not present in general. However, we have found an exact solution of Wu's equation including the $f_{\perp} \psi$ term as a purely radial force density.

The exact solution proceeds from a disc with thickness ϵ and radius R. The undisturbed parallel flow U_0 is perpendicular to the disc. The kinematical part of the solution is given in the cylindrical coordinate system (x, r, φ) by:

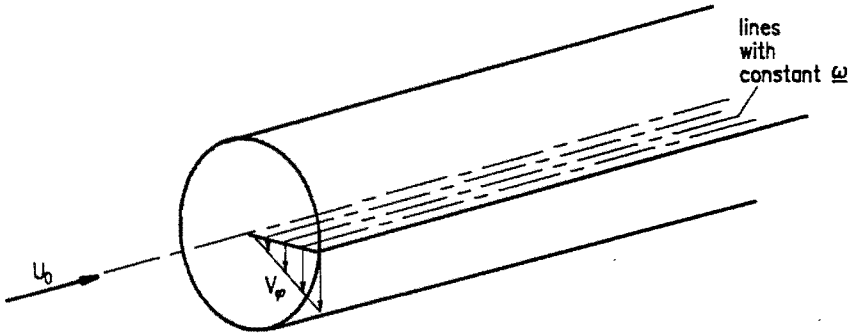


Figure 7.1. An exact solution of Wu's equation: "solid body" rotation of a cylindrical wake.

$$\begin{aligned}
 \psi &= U_0 \pi r^2 \\
 v_\varphi &= \Omega r & r \leq R & \quad x \geq \epsilon/2, \\
 &= \frac{x + \epsilon/2}{\epsilon} \Omega r & r > R & \quad -\epsilon/2 \leq x \leq +\epsilon/2 \\
 &= 0 & & \quad \text{elsewhere.}
 \end{aligned} \tag{7-11}$$

The flow defined by (7-11) is sketched in figure 7.1 for ϵ being zero: it is a solid body rotation of the wake. The wake is the region $x \geq \epsilon/2$, $r \leq R$. Now $\psi = U_0 \pi r^2$ everywhere. Outside the wake and disc $\Gamma = 0$; inside the wake $\Gamma/2\pi = \Omega r^2$. Since $f_{\perp\psi} \neq 0$ only at the disc, substitution of these expressions in (7-2) shows that (7-11) satisfies (7-2) everywhere outside the disc. At the disc Wu's equation simplifies to:

$$\frac{1}{rU_0} \frac{\partial(v_\varphi r)}{\partial r} (\Omega r^2 - v_\varphi r) = \frac{r}{\rho} \frac{f_{\perp\psi}}{U_0} \tag{7-12}$$

where $\Gamma = 2\pi v_\varphi r$, $v_s = U_0$ and $\partial/\partial\psi = (rU_0)^{-1} \partial/\partial r$ have been substituted. It is clear that $f_{\perp\psi}$ is purely radial, so $f_{\perp\psi} \equiv f_r$. With the swirl velocity v_φ given by (7-11), f_r is evaluated as:

$$f_r = \frac{\rho}{2} \Omega^2 r \left[1 - \left(\frac{x}{\epsilon/2} \right)^2 \right] \tag{7-13}$$

Equations (7-11) and (7-13) present an exact solution of Wu's equation (7-2).

The other components of \underline{f} are determined by (7-8) and (7-9). Substitution of (7-10) and (7-11) yields:

$$f_{\varphi} = \frac{(\underline{v} \cdot \nabla) H}{\Omega r} = \rho U_0 \frac{\Omega r}{\epsilon}, \quad (7-14)$$

$$f_x = \frac{1}{U_0} \left[(\underline{v} \cdot \nabla) H - f_{\varphi} v_{\varphi} \right] = \rho \frac{(\Omega r)^2}{\epsilon} \left[\frac{1}{2} - \frac{x}{\epsilon} \right]. \quad (7-15)$$

The resultant expressions for the disc load \underline{F} are obtained by integration of \underline{f} across the disc thickness ϵ :

$$F_{\perp\psi} = F_r = \frac{\rho}{3} \Omega^2 r \epsilon, \quad (7-16)$$

$$F_{\varphi} = \rho U_0 \Omega r, \quad (7-17)$$

$$F_x = \frac{\rho}{2} (\Omega r)^2. \quad (7-18)$$

For $\epsilon \rightarrow 0$ only F_{φ} and F_x remain: F_r is $O(\epsilon)$. The swirl v_{φ} is discontinuous across the disc for $\epsilon \rightarrow 0$, so the disc is a vortex sheet with strength $\gamma = -\underline{e}_{\varphi} v_{\varphi} = -\underline{e}_{\varphi} \Omega r$. Now let $v_{\varphi, \text{disc}}$ denote the average swirl velocity at the disc, which equals $\frac{1}{2} \Omega r$ by (7-11). Then $\underline{v}_{\text{disc}} = \underline{e}_x U_0 + \underline{e}_{\varphi} \frac{1}{2} \Omega r$ by which we see that (7-17/18) represent the two components of $\underline{F} = -\rho \underline{v}_{\text{disc}} \times \underline{\gamma}$.

From the physical point of view the exact solution of Wu's equation presented here may be considered as a trivial actuator disc flow. However, it clearly shows that $f_{\perp\psi}$ can have its origin in radial force densities: it is not merely a component of f_x normal to the streamtube. Finally this solution shows the only actuator disc flow with $v_x = \text{constant}$ at the disc. This is an assumption often made in performance prediction methods. The results of these methods can be considered as the first order solution, with the flow of figure 7.1 as the zero'th order. Van der Spek [1986] has set up a numerical iterative method to solve Wu's equation and a first order solution is obtained.

The most remarkable feature of this solution is the presence of f_x . For a finite thickness

even a radial surface load F_r results; for the infinitely thin disc the radial force density does not yield a surface load. The question arises whether this radial force density is a necessary component of the disc load. In other words: is it possible to apply the disc load F_x (7-17) and F_φ (7-18) without the radial f_r or F_r (7-13/16)? In case of the infinitely thin disc indeed f_r appears to be a necessary component as we will show. For $\epsilon \neq 0$ this is not known.

Assume (7-17) and (7-18) to be the disc load, based on the distributions (7-14) and (7-15) respectively. The disc is infinitely thin. The product uv_φ at the downstream side of the disc (denoted by $x = 0^+$) is determined by the increase of angular momentum across the disc. Since $v_\varphi = 0$ upstream of the disc this yields:

$$\rho (uv_\varphi)_{0^+} = F_\varphi . \quad (7-19)$$

The second relation between u and v_φ is found by integration of (7-8) across the disc. Since, by (7-14), f_φ is constant with respect to x , and $\int u f_x dx = u_{x=0} F_x$ for $\epsilon \rightarrow 0$, this integration yields:

$$u F_x + \bar{v}_{\varphi, \text{disc}} F_\varphi = u \Delta H , \quad (7-20)$$

where $\bar{v}_{\varphi, \text{disc}}$ is the value of v_φ averaged on the disc thickness. Since f_φ is constant with respect to x , it is clear that this average value equals $\frac{1}{2} v_{\varphi, 0^+}$. Using (7-10) the right-hand side of (7-20) becomes $\frac{1}{2} \rho \Omega r uv_{\varphi, 0^+}$. Since F_x and F_φ are known, (7-19) and (7-20) can now be solved for u and $v_{\varphi, 0^+}$. The solution is: $u = U_0$ and $v_{\varphi, 0^+} = \Omega r$. The radial velocity is zero by the continuity equation. These are the values at the downstream side of the disc. By (7-20) also H is known, so $\partial p / \partial r$ at $x = 0^+$ can be determined:

$$\frac{1}{\rho} \frac{\partial p}{\partial r} = \frac{v_\varphi^2}{r} . \quad (7-21)$$

Since the pressure gradient and v_φ are in equilibrium, there will be no wake expansion or contraction downstream of the disc. Consequently the velocity is the same at all downstream distances, and the solution is given by $\psi = U_0 \pi r^2$, $v_\varphi = \Omega r$ in the wake and $v_\varphi = 0$ outside the wake. Substitution of this in (7-2) recovers (7-13), the expression for f_r .

This implies that the force field is not free to choose: a prescribed surface force field F has to be supplemented by a tangential force density, which depends on the flow field. The same dependency is found in appendix F for the flow along a solid boundary. There $f_{\text{tangential}}$ was shown to be the remainder of $\nu \nabla^2 \underline{v}$ for infinite Reynolds number, by comparison with the boundary layer solution. Now we compare the force field (7-13/14/15) with the definition of \underline{f} in (5-4): $\underline{f} = \underline{f}_{\text{ext}} + \underline{f}_{\text{shear stress}}$. It is clear that the azimuthal f_φ and axial f_x represent the externally applied force density, while the radial f_r is the shear stress force density. According to the analysis in section 5.3, $f_{\text{shear stress}}$ is of the same order as Re_ϵ^{-1} , being the inverse of the thickness based Reynolds number, although the order itself was unknown. By (7-13) this order is known to be $O(1)$ for this specific actuator disc flow. Further discussion on this subject is postponed to Chapter 9.

In the next section, similar relations for the force- and flow field are obtained for discs without azimuthal velocities, and for the 2-D equivalent, the actuator strip. For completeness the simplified versions of Wu's equation for these specific actuator surface flows are derived here.

If the angular velocity Ω is increased to infinity, meanwhile keeping the converted power $\iint \underline{f} \cdot \underline{v} \, dA$ constant, (7-7) and (7-9) show f_φ and $v_\varphi = \Gamma/2\pi$ to vanish like Ω^{-1} . By (7-10) the product $\Omega\Gamma$ remains finite, so Wu's equation (7-2) then becomes:

$$\frac{\partial^2 \psi}{\partial x^2} + \frac{\partial^2 \psi}{\partial r^2} - \frac{1}{r} \frac{\partial^2 \psi}{\partial r} = \frac{r^2}{\rho} \frac{\partial H}{\partial \psi} - \frac{r}{\rho} \frac{f_\perp \psi}{v_s} \quad (7-22)$$

The 2-D equation is derived analogous to the 3-D equation. In a cartesian coordinate system (x,y,z) with x parallel with U_0 , y normal to x in the 2-D plane and z normal to this plane, the streamfunction ψ is defined by $\underline{v} = \underline{\nabla} \times \underline{e}_z \psi$. Analogous to (7-3) the kinematical relation between ω and ψ is:

$$\omega = - \left[\frac{\partial^2 \psi}{\partial x^2} + \frac{\partial^2 \psi}{\partial y^2} \right] \quad (7-23)$$

With n as the coordinate in the 2-D plane normal to a streamline, the relation between $f_\perp \psi$, H and v_s is given by the n -component of (7-1). Analogous to (7-4/5) this reads:

$$v_s \frac{\partial H}{\partial \psi} = f_{\perp} \psi - \rho v_s \omega . \quad (7-24)$$

The combination of (7-23) and (7-24) yields the strip equation, equivalent to (7-22):

$$\frac{\partial^2 \psi}{\partial x^2} + \frac{\partial^2 \psi}{\partial y^2} = \frac{1}{\rho} \frac{\partial H}{\partial \psi} - \frac{1}{\rho} \frac{f_{\perp} \psi}{v_s} . \quad (7-25)$$

The right-hand sides of (7-22) and (7-25) differ by the occurrence of r in (7-22): this is due to ψ having a different dimension in 2-D and 3-D flows. For a constant, normal load, the right-hand side term in both equations is non-zero only at the wake boundary.

7.2. The smooth actuator surface force field.

The actuator surfaces in this section are 2-D strips, or 3-D discs without azimuthal forces and velocities. Then the flow induced by the disc is described completely in the meridional plane. If necessary the distinction between the strip and disc will be denoted, but in general the name actuator surface is used. Figure 7.2 shows a cross section through an actuator surface, thickness ϵ , and the cartesian coordinate system (x,y) and the orthogonal curvilinear system (s,n) , the latter having scale factors h_s and h_n . The x coordinate is normal to the surface while n is normal to the streamline. The unit vectors are denoted by \underline{e} with the appropriate index. The velocity is assumed to be steady and continuous across the strip. The distribution of f_{ext} is given by (5-7/8). The equation of motion is (7-1). For simplicity the undisturbed upstream flow is assumed to be free of vorticity with the Bernoulli constant $H = H_0$.

Application of Stokes' theorem to $\underline{\nabla} \times \underline{f}$ on area A gives:

$$\int_a^b \underline{e}_s \cdot \underline{f} h_s ds - \int_c^d \underline{e}_s \cdot \underline{f} h_s ds = - \rho \int_b^d (\underline{v} \times \underline{\omega}) \cdot \underline{e}_y dy , \quad (7-26)$$

where the positions a through d are shown in figure 7.2. From (7-1) it is clear that:

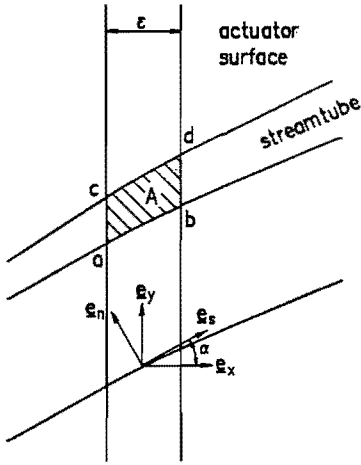


Figure 7.2. Cross section through an actuator surface.

$$\int_{\epsilon} \mathbf{e}_s \cdot \mathbf{f} h_s ds = H_{x=\epsilon/2} - H_0 \quad (7-27)$$

Substitution of (7-27) into (7-26) yields:

$$H_b - H_d = \rho \int_b^d u \omega dy \quad (7-28)$$

or:

$$\left[\frac{\partial H}{\partial y} \right]_{x=\epsilon/2} = \rho (u\omega)_{x=\epsilon/2} \quad (7-29)$$

Expression (7-29) is used to simplify the tangential component of the equation of motion (7-1), which is:

$$f_y = \frac{\partial H}{\partial y} + \rho u \omega \quad (7-30)$$

The tangential surface load F_y is:

$$F_y = \int_{\epsilon} f_y dx = c \left[\frac{\partial H}{\partial y} + \rho u \omega \right]_{x=\epsilon/2} \quad (7-31)$$

where c is a constant depending on the distribution of f_y . Obviously $0 < c < 1$; the values $c = 0$ and 1 are excluded as these imply f_y being singular at $x = 1$ and 0 respectively. This is incompatible with the assumption of smooth distributions.

Substitution of (7-29) now gives:

$$F_y = 2c \epsilon \left[\frac{\partial H}{\partial y} \right]_{x=\epsilon/2} \quad (7-32)$$

This result leads to the conclusion that it is not possible to apply merely a non-constant normal load F_x : assuming such a load distribution yields, by (7-27), a non-zero value for $(\partial H / \partial y)_{x=\epsilon/2}$. Then (7-32) shows that F_y is non-zero.

For $\epsilon \rightarrow 0$, the average tangential force density is easily expressed in the normal load distribution. Integration of the x -component of (7-1) across the thickness ϵ yields:

$$F_x = \int_{\epsilon} f_x dx = (H_{x=\epsilon/2} - H_0) - \int_{\epsilon} \rho v \omega dx \quad (7-33)$$

Since only smooth distributions of F_x are assumed, $v\omega$ remains finite for $\epsilon \rightarrow 0$. For an infinitely thin disc F_x then becomes:

$$F_x = \Delta H = H_{\epsilon/2} - H_0 \quad \text{for } \epsilon \rightarrow 0 \quad (7-34)$$

The average value of the force density \bar{F} equals F/ϵ , so using (7-31/32/33):

$$\bar{F}_x = \frac{\Delta H}{\epsilon} - \rho \overline{v\omega} \quad (7-35)$$

and

$$\bar{F}_y = \frac{\partial H}{\partial y} + \overline{\rho u \omega} = 2c \left[\frac{\partial H}{\partial y} \right]_{x=\epsilon/2} \quad (7-36)$$

Substitution of (7-34) yields an alternative expression for \bar{F}_y :

$$\bar{f}_y = 2c \frac{dF_x}{dy} \quad (7-37)$$

If f_y is distributed symmetrically, $c = \frac{1}{2}$ by which (7-37) becomes identical to (F-8) in appendix F. As in the previous section and in appendix F, again a relation is found between the externally applied surface load F and a resulting tangential force density f_y . The explanation of this is the same as in the previous section, where the solution of Wu's actuator disc equation was discussed: f_y represents the shear stress.

For the actuator surfaces discussed here the conclusion is that it is not possible to apply an arbitrary normal actuator surface load F without accepting a dependent tangential force density f . This conclusion is valid for actuator surfaces with a smooth distribution of the normal force as long as the streamlines are not tangent to the surface. It does not depend on the thickness of the surface. If the thickness is non-zero, this tangential force density results in a tangential surface load.

For infinitely thin surfaces, this tangential force density is of mathematical interest only: since force densities, not resulting in surface- or discrete loads, do not change the momentum or energy of the flow, only $F_x = \Delta H$ is important in the determination of the flow induced by the force field. However, this may be different for surface load distributions which show discontinuities. Such a discontinuity is present at the edge of an actuator surface with constant, normal surface load, which is the subject of the next chapter.

Chapter 8

THE EDGE SINGULARITY OF AN ACTUATOR SURFACE WITH A CONSTANT NORMAL LOAD

Froude's concept of the actuator disc and strip assumes a constant pressure jump $e_x \Delta P = \int f_{\text{ext}} dx$, where the integration is performed across the thickness ϵ of the strip or disc. In this expression e_x is the unit normal vector, while f_{ext} is the externally applied force density defined in (5-7/8). Now we draw a closed contour C lying in the 2-D plane (in case of the strip), or in a plane intersecting the disc, see figure 8.1. If one edge is enclosed by the contour, the integral $\oint \underline{f} \cdot \underline{dc}$ is non-zero; in all other cases it is zero. Since this contour can be made arbitrarily small, as long as the edge is enclosed, this implies that $\nabla \times \underline{f} \neq 0$ at the edge. Therefore non-conservative force densities, defined as not being a gradient of a scalar, must be present at the edge. The surface distribution f_{ext} itself is conservative.

The aim of this chapter is to investigate the character of the edge singularity and to find out whether non-conservative force densities at the edge are the resultant of it. The equation of motion is (5-5), and the force field f_{ext} satisfies (5-7/8). The actuator surface is the 2-D strip or 3-D disc without azimuthal forces and velocities, as in section 7.2.

8.1. A discrete vortex as edge singularity

Figure 8.1 shows an actuator strip or cross-section through a disc in a meridional plane, which is a plane containing the disc axis. The area of the cross-section is denoted by S and A is the edge area, being a part of S . The cartesian coordinate system (x,y,z) and the cylindrical system (r,θ,z) have a common origin in the center of A . The direction of z is normal to the plane; x is normal to the symmetry line of the surface and y is normal to z and x . The force density distribution is defined by:

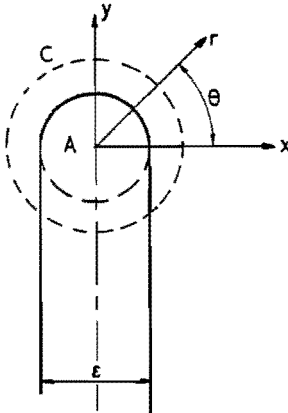


Figure 8.1. The edge of the actuator surface

$$\begin{aligned}
 \nabla \times \underline{f} &= \underline{e}_z g(r, \Theta) && \text{at } A, r \leq \epsilon/2, 0 \leq \Theta \leq 2\pi \\
 \underline{f} &= \underline{e}_x f(x) && \text{at remainder of } S \\
 \text{with } \underline{f} &= \underline{0} && \text{for } r = \frac{1}{2}\epsilon, 0 \leq \Theta \leq \pi \text{ and } |x| = \epsilon/2 \quad (8-1) \\
 \underline{f} &= \underline{e}_x f(x) && \text{for } r = \frac{1}{2}\epsilon, \pi \leq \Theta \leq 2\pi \\
 f(x) &= F \delta(x) && \text{for } \epsilon \rightarrow 0,
 \end{aligned}$$

while:

$$\int_{\epsilon/2}^{\epsilon/2} f(x) dx = F \quad \text{for all } \epsilon. \quad (8-2)$$

F is the surface load which is constant outside the edge area A. Outside A, no vorticity is shed into the flow according to (5-6) since $\nabla \times \underline{f} = 0$ for constant F. Then F equals the jump in the Bernoulli constant ΔH as is clear from (7-33). Far upstream we assume the flow to be undisturbed with the Bernoulli constant equal to H_0 . Then $H = H_0 + F$ on all streamlines which have passed the surface in the region $S - A$. These streamlines constitute the wake. At the edge A $\nabla \times \underline{f} \neq 0$, so vorticity is shed into the flow forming a vortex sheet. This sheet separates the wake flow from the flow not having passed the surface, and exhibits a constant jump ΔH in the Bernoulli constant.

The functions $f(x)$ and $g(r, \Theta)$ are free to be chosen as long as (8-1) and (8-2) are satisfied. For given functions the boundary conditions and the right-hand side of the

differential equation $\nabla \times \underline{f} = \underline{e}_z g(r, \Theta)$ are known. This determines the distribution of \underline{f} at A uniquely provided that there is no non-trivial solution of $\nabla \times \underline{f} = 0$. The curl of the equation of motion, given by (5-6) with $(\underline{\omega} \cdot \nabla) \underline{v} = 0$, provides the expression for $\nabla \times \underline{f}$:

$$\nabla \times \underline{f} = \rho \frac{\partial \underline{\omega}}{\partial t} + (\underline{v} \cdot \nabla) \underline{\omega} = \frac{D \underline{\omega}}{Dt} . \quad (8-3)$$

If $\nabla \times \underline{f} = 0$ no vorticity is generated, so the force field does not influence the kinematics of the flow. In the context of this chapter such a distribution is trivial, and is ignored. Therefore for given functions $f(x)$ and $g(r, \Theta)$ the force density field is determined completely.

The curl of \underline{f} gets order ϵ^{-2} for $\epsilon \rightarrow 0$, as we will show. Assume a closed curve C , enclosing the edge region A completely. The index c denotes the component along C , and dc is an element of C . Then Stokes' theorem combined with (8-2) yields:

$$\underline{e}_z \cdot \iint_A \nabla \times \underline{f} dA = \int_C f_c dc = F . \quad (8-4)$$

For $\epsilon \rightarrow 0$

$$\underline{e}_z \cdot (\nabla \times \underline{f}) = \frac{F}{A} = O(\epsilon^{-2}) \quad \text{for } \epsilon \rightarrow 0 . \quad (8-5)$$

Since $\nabla \times \underline{f} = 0$ outside A the left-hand side integration can be extended beyond the contour C . The combination of (8-4) and (8-5) then shows that $\nabla \times \underline{f} = F \delta(x) \delta(y)$ for $\epsilon \rightarrow 0$. According to van de Pol & Bremmers [1964], page 316/317, this two dimensional delta function can be written as a delta function in r , by which:

$$\underline{e}_z \cdot (\nabla \times \underline{f}) = 2 \delta(r) F \quad \text{for } \epsilon \rightarrow 0 . \quad (8-6)$$

For $\epsilon \rightarrow 0$, (8-5) shows that $D\underline{\omega}/Dt$ becomes $O(\epsilon^{-2})$ which implies singular flow. Furthermore by (8-6) $D\underline{\omega}/Dt$ becomes independent of Θ .

Equation (8-3) describes the generation of vorticity by the force density fields. If the convective term in (8-3) is zero, all vorticity remains at the edge area A , and an unsteady flow results. On the other hand, a steady solution requires that the vorticity is transported away from the edge. We discuss both solutions separately; in general the

flow may be a combination of both.

First the flow with $(\underline{v} \cdot \underline{\nabla}) \underline{\omega} = 0$ is treated. We apply Stokes' theorem on (8-3), with the circle C defined by $r > \epsilon/2$ as path of integration, and use (8-4):

$$F = \oint_C f_c \, dc = \frac{\partial}{\partial t} \oint_C v_c \, dc = \frac{\partial \Gamma}{\partial t} . \quad (8-7)$$

For $\epsilon \rightarrow 0$, region A becomes a singular point, carrying a discrete vortex Γ which increases linearly in time. The situation with $(\underline{v} \cdot \underline{\nabla}) \underline{\omega} = 0$ will occur if the force field is put on at time $t = 0$ in a flow field which was at rest for $t < 0$. At $t = 0$ a vortex will be generated by the force field according to (8-7). During the initial phase the edge flow is characterized by self-induced velocities only, since the velocity induced by vorticity generated elsewhere is negligible. After a while this velocity induced by other vorticity becomes significant, by which $(\underline{v} \cdot \underline{\nabla}) \underline{\omega}$ becomes non-zero at the edge. The vorticity generated at the edges will be transported downstream instead of being accumulated at the edge. After a sufficiently large time a steady flow will be obtained, in which the generation of vorticity at the edge is in equilibrium with the transportation of it downstream. According to this interpretation, (8-7) describes the generation of the starting vortex pair (2-D flow) or ring (3-D flow) of the actuator surface.

Now we assume the flow to be steady, and (8-3) is written as:

$$\frac{1}{\rho} \underline{e}_z \cdot \underline{\nabla} \times \underline{f} = v_s \frac{\partial \omega}{\partial s} , \quad (8-8)$$

where v_s is the velocity at the streamline s , and $\partial/\partial s$ denotes differentiation along the streamline. For $\epsilon \rightarrow 0$, the left-hand side gets order ϵ^{-2} and becomes circular symmetric, due to (8-5/6). In this limit, $\partial\omega/\partial s$ becomes $O(\Delta\omega/\epsilon)$, where $\Delta\omega$ is the increase of the vorticity on the streamline while passing the surface. An infinite value of $\Delta\omega$ implies a discontinuity of the velocity; the demand for circular symmetry of the right-hand side of (8-8) then requires such a discontinuity to occur at each Θ for fixed $r < \epsilon$, which is impossible. Therefore we assume $\Delta\omega$ to remain finite for all ϵ . Then $\partial\omega/\partial s = O(\epsilon^{-1})$ for $\epsilon \rightarrow 0$, so the combination of (8-5) and (8-8) shows:

$$v_s = O(\epsilon^{-1}) \quad \text{for } \epsilon \rightarrow 0 . \quad (8-9)$$

Due to the circular symmetry of the flow dictated by (8-6), $v_s \rightarrow v_\Theta$ and

$$\Gamma = \oint_C v_\Theta r d\Theta = O(1) \text{ for } \epsilon \rightarrow 0 . \quad (8-10)$$

As in the unsteady solution (8-7) we find the discrete vortex as edge singularity. Now the flow is steady, so the generation of vorticity at the edge is in equilibrium with the transport of vorticity downstream; the average velocity \bar{v} at the edge is non-zero. The flow field near the edge is dominated by the singularity, so the vortex sheet which carries the vorticity downstream spirals around the edge with decreasing velocity for increasing radius. This is a well-known connection between a vortex as edge of a vortex sheet, and the sheet itself, e.g. in the case of the roll-up of trailing vorticity of a finite wing.

The combination of the edge vortex and the spirally wound vortex sheet may remove a possible objection against the proposed edge singularity: the velocity induced by a vortex ring (core ϵ , radius R) on itself, is known to be proportional to $\ln(\epsilon/R)$. This self-induced velocity becomes infinite for $\epsilon \rightarrow 0$, which evidently conflicts with the present solution. However, the vorticity distributed on the vortex sheet spiral also induces a velocity field at the vortex core, which can remove this logarithmic singularity. This problem can only be solved analytically if the asymptotic behavior of the vortex sheet spiral is known; if not a numerical analysis with $\epsilon/R \rightarrow 0$ has to provide the answer. In this thesis we restrict ourselves to local considerations, so this problem remains unsolved. For the actuator strip flow this problem does not exist.

Although we do not know the general flow field, we can sketch the flow field around the edge, based on the numerical results of Lee & Greenberg [1984], see section 8.3.2 and 6.1.2. The division between the flow passing through the surface and flowing along it, is formed by the vortex sheet and by the dividing streamline. This streamline ends in a "free" stagnation point at the sheet. The streamlines entering the spiral region pass the surface in downstream direction once more than in upstream direction, so experience a final pressure jump equal to Δp . In case of hover, so with no ambient flow, all streamlines pass the surface so there is no dividing streamline, see figure 6.2.

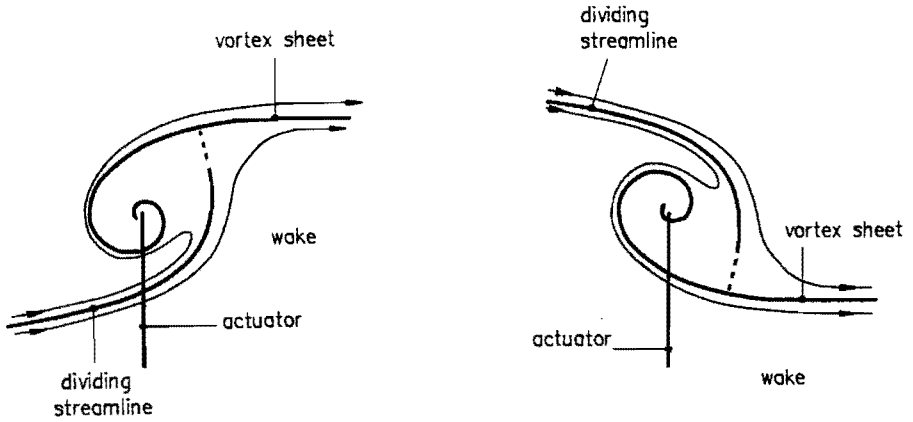


Figure 8.2. Sketch of the flow pattern near the edge, for a decelerating (left) and accelerating (right) flow.

8.2. The possible existence of edge forces

The steady flow around the edge is characterized by a bound vortex at the edge, which is capable of carrying a resultant force $\underline{\bar{F}}$. We start again with a finite value of ϵ . The equation of motion, written in the form (7-1), is integrated on the edge area A , see figure 8.1:

$$\underline{\bar{F}} = \iint_A \left[\underline{\bar{v}} H - \rho (\underline{v} \times \underline{\omega}) \right] dA . \tag{8-11}$$

The Bernoulli constant H is finite everywhere, so the first term between the brackets vanishes in the limit $\epsilon \rightarrow 0$. The flow is steady and the velocity $\underline{\bar{v}}$ averaged on the edge area must be non-zero, so for $\epsilon \rightarrow 0$ (8-11) becomes :

$$\underline{\bar{F}}_{\text{edge}} = -\rho \iint_A \underline{v} \times \underline{\omega} dA = -\rho \underline{\bar{v}} \times \underline{\Gamma} \quad \text{for } \epsilon \rightarrow 0 \tag{8-12}$$

with $\underline{\Gamma} = \iint_A \underline{\omega} dA .$

$\underline{\bar{v}}$ is the average velocity at A induced by the far-field vorticity and/or the undisturbed

flow. The order of magnitude of \bar{v} cannot be derived from local considerations. Only a complete solution, including the far field, can provide this order, which is the order of \tilde{F}_{edge} at the same time. As $\bar{v} \neq 0$ also $\tilde{F}_{\text{edge}} \neq 0$ but we do not know whether it is $o(1)$, so may be infinitesimal small, or $O(1)$ so has a finite value.

In appendix D we present a reduction ad absurdum proof which concludes that the edge force must be finite: this proof proceeds from the limit of an actuator strip for vanishing dimensions, meanwhile keeping the resultant force constant: then a singular force remains. If this force is perpendicular to the undisturbed flow, the well-known vortex flow should be the result. A strip without edge forces cannot yield the vortex flow as the result of this limit, as we show in appendix D. The strip including edge forces is able to do so: if the edge forces are assumed to be $O(1)$, indeed the well-known force on a discrete vortex results. However, the proof has a limited validity: it does not provide the order of the edge forces in a straightforward manner. It only concludes that the edge forces must be finite, in order to yield the desired limit behavior of the strip for vanishing length.

We now can write down the complete force field of an infinitely thin actuator surface with a constant, normal surface load inducing a steady flow. Returning to the introduction of this chapter, we use the distinction conservative and non-conservative:

$$\begin{aligned} \underline{F}_x &= \underline{F}_{\text{cons}} = \underline{e}_x \Delta H \\ \tilde{\underline{F}}_{\perp} \psi &= \tilde{\underline{F}}_{\text{non-cons}} = -\rho (\bar{v} \times \underline{\Gamma})_{\text{edge}} \end{aligned} \quad \text{for } \epsilon \rightarrow 0, \quad (8-13)$$

with:

$$\begin{aligned} \Gamma &= O(1) \\ \bar{v}_{\text{edge}} &\neq 0 \quad \text{but of unknown order.} \end{aligned} \quad (8-14)$$

Here \underline{e}_x is the unit vector normal to the surface, $\tilde{\underline{F}}_{\perp} \psi$ is normal to the stream-tube. The result (8-13) is consistent with section 7.2, equations (7-35/36), where smooth force fields are discussed. Only the term $\overline{\partial H / \partial y}$ in (7-36) does not appear in (8-13): since H is finite, the order of this term for $\epsilon \rightarrow 0$ is ϵ^{-1} . Integration on the edge area A which is $O(\epsilon^2)$ does not yield a finite contribution.

8.3. The comparison with other edge singularity solutions

Greenberg [1972] and Lee & Greenberg [1984] give numerical results for actuator discs and strips, based on the equations of Wu discussed in section 7.1. At the edge, they assume a square root singularity in the vortex sheet strength, based on their integral equations. Schmidt & Sparenberg [1977] present a spiral solution for the flow around the actuator strip edge.

8.3.1 The spiral solution of Schmidt & Sparenberg [1977]¹

This solution is based on a particular property of actuator strips with a constant, normal surface load F , see appendix A: the flow induced by such a force field depends only on the magnitude of F , and on the positions of the edges of the strip. The surface itself may have any position as long as the edges remain the same. The edges of the strip are the leading edges of the vortex sheets. Therefore the flow induced by an infinitely thin actuator strip with a constant, normal load F is identical to the flow induced by 2 semi-infinite, infinitely thin plates, carrying a constant load F and coinciding with the vortex sheets. The load F equals the pressure jump Δp . If the original actuator strip is assumed to be semi-infinite only one vortex sheet remains. If furthermore the undisturbed parallel flow is assumed to be zero, the kinematical problem has become: how to design a semi-infinite, infinitely thin lifting sheet with a constant pressure jump Δp with only self-induced velocities present? This problem can be solved as an irrotational flow problem. Schmidt & Sparenberg use conformal transformation techniques to derive their solution, which is given here briefly in equations (8-15/16) and figure 8.3. The shape of the vortex sheet is an exponential spiral $r = e^{\Theta}$, figure 8.3a. The complex potential is:

$$\begin{aligned} \chi(z) &= cz \frac{1-i}{2} \\ c^2 &= \frac{4\Delta p}{\rho(e^{2\pi}-1)} \end{aligned} \quad (8-15)$$

The vortex sheet is characterized by a constant strength γ and velocity \bar{v} , being the

¹ Also to be found in Sparenberg (1984).

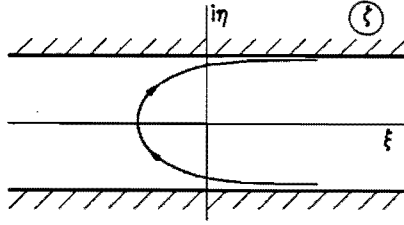
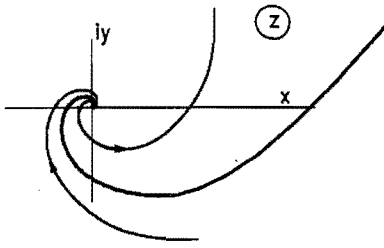


Figure 8.3a. The exponential spiral.

Figure 8.3b. Flow between two walls.

average of the velocity on both sides of the sheet:

$$\begin{aligned} \gamma &= \frac{c}{\sqrt{2}} (e^\pi + 1) \\ \bar{v} &= \frac{\Delta p}{\rho} \frac{1}{\gamma} \end{aligned} \quad (8-16)$$

Schmidt & Sparenberg obtain (8-15) by conformal transformation of the flow between two parallel walls in the ζ -plane, see figure 8.3b, using $z = e^{(1+i)\zeta}$.

The shape of the sheet is equiangular: at each position (r, Θ) at the sheet, the angle between the unit radius vector \mathbf{e}_r and the tangent at the sheet is $\pi/4$. In one revolution the radius of the sheet increases or decreases by a factor $e^{2\pi}$ or $e^{-2\pi}$ respectively. The vortex sheet strength γ and the velocity \bar{v} are constant along the sheet. This implies that we obtain exactly the same flow field if we change the scale of the flow pattern by a factor $e^{2n\pi}$, where n is an integer. In other words: the solution is independent of any length scale.

We compare the original actuator strip force field with the force field on the spiral by evaluating $\nabla \times \mathbf{f}$ on both surfaces. The equivalence of the strip and spiral is based on the assumption that $\nabla \times \mathbf{f}$ is identical for both surfaces, see appendix A. The strip as well as spiral are covered by a normal, constant distribution of \mathbf{f} yielding a pressure jump $\Delta p = F = \int \mathbf{f} \cdot d\mathbf{n}$, with \mathbf{n} normal to the surface and the integral taken across the thickness ϵ of the surface. Since ϵ is assumed to be zero, \mathbf{f} equals $\delta(\mathbf{n})F$. We enclose the edge area A by a circle C , see figure 8.4. Using Stokes' theorem on area A we obtain expression (8-4) for both the strip and the spiral: $\int_C \nabla \times \mathbf{f} \cdot d\mathbf{A} = F$. However, evaluation of $\nabla \times \mathbf{f}$ in a local orthogonal (s, n) coordinate system, with s tangential and n normal to the surface, does not yield the same result for both surfaces. We integrate $\nabla \times \mathbf{f}$ across the infinitely thin thickness ϵ of the surface. Since \mathbf{f} is normal to the

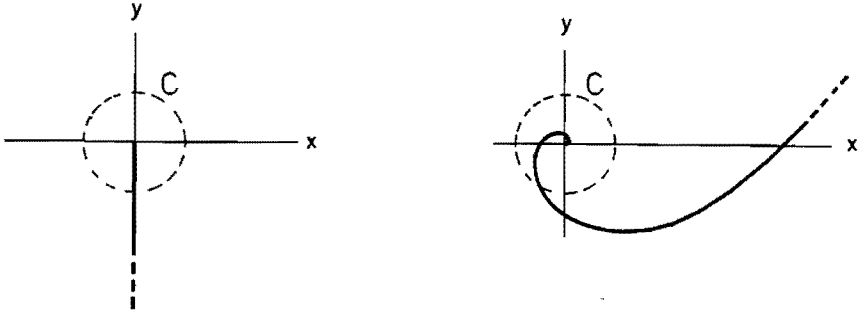


Figure 8.4. The spiral and strip with constant, normal load as equivalent actuator surfaces

surface the integral becomes:

$$\int_{\epsilon} \nabla \times \mathbf{f} \, dn = \int_{\epsilon} \frac{df_n}{ds} \, dn = \frac{dF_n}{ds} \quad (8-17)$$

It is clear that dF_n/ds is infinite at the edge of the strip since the distribution of F is a step function. This implies that dF_n/ds must be infinite at the center of the spiral too. However, $dF_n/ds \equiv 0$ everywhere at the spiral. Furthermore, owing to the absence of any scale in the spiral flow, the edge cannot be defined, and it is not possible to investigate any limit behavior of dF_n/ds for $s \rightarrow 0$.

In order to introduce a scale in the solution of Schmidt & Sparenberg, we have studied in appendix B the flow around an exponential spiral with finite length. This flow is defined on a multi-branched Riemann surface. If the limit towards an infinite length is taken, an infinite spiral is obtained and indeed (8-15) is the result. However, in contrast with the method of Schmidt & Sparenberg, this derivation yields the conditions for the solution at infinity. These imply that the flow cannot be described in the 2-D plane since the equations of motion are not satisfied at infinity: there the streamlines are normal to each other at the branch line.

8.3.2 Greenberg's square root singularity

Greenberg [1972] and Lee & Greenberg [1984] present numerical solutions of Wu's equation (7-2) for the 2-D respectively 3-D flow, especially for the case of constant, normal surface load. Here we discuss the 2-D solution; the 3-D solution is similar. The

physical interpretation of their non-linear integral equation, being the converted Wu-equation, is the following: at each position (x,y) in a cartesian coordinate system, the velocity disturbance is induced by vorticity of yet unknown strength, lying at a streamline of yet unknown shape. The leading edge of the vortex sheet is the strip edge. By assuming a set of suitable chosen basic functions to describe the strength and shape of the vortex sheet, the coefficients of these functions are calculated iteratively. Greenberg argues that one of the functions to describe the vorticity distribution, must contain a square root singularity, as this should be dictated by the kernel of the integral equation:

$$\Psi(x, y) = \int_L \frac{1}{2\pi} \ln r^*(x,y,s) \gamma(s) ds \quad (8-18)$$

where the integration is performed along the vortex sheet L , with s as arc length parameter, and r^* the distance from (x, y) to the position s . Equation (8-18) is exactly the same equation as the one describing the flow around a flat plate edge (Sparenberg [1984]), which indeed results in the square root singularity of γ . A necessary condition for this however, is that with s as distance from the leading edge,

$$\lim_{s \rightarrow 0} (\text{radius of curvature}) \neq 0 \quad (8-19)$$

This is shown by our following analysis. The normal velocity at a steady vortex sheet has to be zero. If the position at the sheet is characterized by s_0 , the normal velocity is given by $\partial\Psi/\partial s_0$. Using (8-18), this condition for zero normal velocity becomes:

$$\int_L \gamma(s) \frac{1}{r} \frac{\partial r^*}{\partial s_0} ds = 0 \quad (8-20)$$

Assume $\partial r^*/\partial s \approx 1$ for $s < \epsilon$ with ϵ measured from the leading edge of the sheet along L . At a certain position $s_0 < \epsilon$, (8-20) may be written as:

$$\int_0^\epsilon \gamma(s) \frac{1}{s-s_0} ds + (\text{contribution of } L \text{ for } s > \epsilon) = 0 \quad (8-21)$$

The second term will be finite, so the first term has to satisfy, with $x = s/s_0$:

$$\int_0^{\epsilon/s_0} \gamma(x) \frac{1}{x-1} dx = O(1) . \quad (8-22)$$

For $s_0 \rightarrow 0$, $\gamma = 1/\sqrt{x}$ is a solution, which appears after substitution:

$$\int_0^{\infty} \frac{1}{\sqrt{x}} \frac{1}{x-1} dx = 2 \int_0^1 \frac{d\sqrt{x}}{x-1} + 2 \int_1^{\infty} \frac{d\sqrt{x}}{x-1} ,$$

and replacing x by $1/y$ in the last term:

$$= 2 \int_0^1 \frac{d\sqrt{x}}{x-1} - 2 \int_0^1 \frac{d\sqrt{y}}{y-1} = 0 . \quad (8-23)$$

The square root singularity indeed is a solution of (8-18), but a necessary condition for this is that $\partial r^*/\partial s \rightarrow 1$ for $s < \epsilon$, where ϵ can be made arbitrarily small.

A spiraling flow which is expected due to the discrete vortex as leading edge, does not satisfy (8-19), so cannot have a square-root singularity. Furthermore, a vortex sheet with such a singularity cannot satisfy the dynamical boundary condition: a constant jump in H . If, by the method of Appendix A, the vortex sheet is considered as a lifting vortex sheet, this condition becomes: the pressure jump Δp must be constant along the sheet. From the flat plate flow with the square root singularity we know that the pressure jump either is zero (if the plate is normal to the undisturbed flow), or infinite. A finite pressure jump is inconsistent with a square-root singularity of γ . Nevertheless, at some distance from the edge, the induced velocity field will be independent of the type of the γ -singularity. Since the square root singularity is integrable, the use of this singularity instead of a discrete vortex singularity will not influence the general flow properties, provided that the magnitudes are correct.

Inherent to Greenberg's method are the edge suction forces connected to the square-root singularity. This explains Greenberg's results, shown in figure 2.5: the discrepancy between the classical actuator disc momentum theory and his numerical results is caused by the fact that this theory does not account for the edge forces. On the other hand, the good correlation with rotor experiments (compare figures 2.4 and

2.5) confirms the qualitative conclusion of Part I, that the actuator disc including edge forces is a better representation of a real rotor than the classical disc.

Chapter 9

DISCUSSION ON THE RESULTS; CONCLUSIONS

This chapter consists of three parts. First an extensive survey of the results is presented; some of the results give reasons for discussions, which are indicated briefly in the second section. The last section formulates the conclusions.

9.1 Survey of the results

9.1.1 Part I: the rotor problem

The momentum theory applied to rotors.

In section 2.2 the performance of rotors in axial flow predicted by the classical actuator disc momentum theory, is compared with experimental results, which reveals a systematic deviation: in all flow states of propellers and wind turbine rotors the measured average velocity at the rotor is higher than predicted.

This momentum theory assumes a real rotor to be represented by a disc with a uniform load. Apart from problems introduced by this crude approximation such as the effect of neglecting the finite number of blades, a main drawback is that the theory appears to proceed from an invalid assumption, if it is applied to rotors: it is assumed that the entire axial thrust converts power to or from the flow. However, for rotor blades having zero pitch, flat plate aerofoils, we have shown that the load on the chordwise bound vorticity yields a contribution to the thrust without contributing to the torque (section 2.3). This implies that the thrust performing work is smaller than the total thrust. This is also true for rotors having a different blade geometry, although the proof then depends on the assumption that the out-of-the-rotor-plane component of the chordwise tip vorticity is negligible. In practical operation of all rotors this is the case.

The momentum theory including edge forces.

Both observations lead to the idea that a 'natural' concentration effect exists, in contrast with artificial concentrators such as tipvanes or shrouds. The representation of such an effect by an actuator disc model is obtained by introducing edge forces, to be added to Froude's concept. These forces do not perform work, since they are perpendicular to the local velocity. The momentum theory accounting for these forces requires the ratio between the total load (surface load + edge load) and surface load alone to be known (chapter 3). For real rotors, this is the ratio between the total thrust and the thrust doing work T/T_{work} . If this ratio exceeds the value 1.0, as indicated above, indeed the performance prediction is improved qualitatively by the introduction of edge forces in the momentum theory. A quantitative result cannot be obtained as the ratio itself is still unknown. However, in order to confine to the experimental data from literature, the predicted converted power should be approximately 10% higher than the value predicted by the momentum theory based on Froude's concept. For a wind turbine this implies that the maximum attainable efficiency is increased from $C_p = 0.59$, which is the classical Lanchester-Betz upper limit, to $C_p \approx 0.65$.

The experiment.

In the experiment (chapter 4) we have used the momentum theory including edge forces to predict the performance of a 1 m diameter rotor model in hover. This requires the ratio T/T_{work} to be known. We have defined T_{work} as the ratio of the power P and the average velocity \bar{u}_d . The thrust T has been measured by a balance, while P and \bar{u}_d are obtained from measurements in the wake. The result is that $T/T_{\text{work}} = 1.21$, so only 83% of the thrust is effective in doing work. Using this value in the momentum theory of chapter 3, the prediction of the rotor wake contraction $R_{\text{far wake}}/R$ becomes 0.78, which agrees very well with the experimental value 0.77. The classical prediction amounts to $\sqrt{2} = 0.707$.

The prediction of \bar{u}_d , the average velocity through the rotor disc, is also improved, although still 13% too low. The classical prediction is 21% too low. The origin of this 13% deviation is to be found in the application of the energy balance in the momentum theory in order to obtain T_{work} . In the actuator disc flow, each streamline passing the disc is de- or accelerated equally. For a real rotor this is certainly not true, for which reason the energy balance is replaced by $T_{\text{work}} = P/\bar{u}_d$. Apparently this interpretation of the energy balance is appropriate as far as it concerns momentum theory expressions, such as the wake contraction, which depends on the resultant loads T and

T_{work} . As soon as the distribution of the load is concerned, as in the prediction of velocities, this interpretation of the energy balance improves the prediction, but still is not accurate enough. Improving this requires a description of the energy balance which accounts for non-uniform distributions.

8.1.2 Part II: The actuator disc problem

Numerical and experimental data from literature.

The uniformly loaded actuator disc exhibits a flow singularity at the edges, the nature of which has to be determined. The theoretical question arises whether this singularity implies edge forces, since numerical and experimental data available in literature seem to indicate such (chapter 2).

Lee & Greenberg [1984] report 2-D actuator strip experiments in a shallow water tank. Although difficult to interpret owing to the limited amount of data, the measurements indicate a deviation of average velocity through the strip ($\approx 4\%$), as compared with the classical prediction. The calculations by the same authors also show a deviation: 10%. Schouten [1983] reports a 2-D calculation similar to those of Lee & Greenberg on a less heavily loaded strip, showing a deviation of 1.6%. Castro [1971] studies the maximum deceleration of a steady air flow by a 2-D screen in a wind tunnel. The classical momentum theory predicts this to occur at a dimensionless load coefficient of 1.0, while Castro finds 1.2. Finally Madsen [1985] describes calculations on a 2-D, decelerating flow through an actuator cylinder. The power converted from the flow exceeds the value of the classical momentum theory by 4%.

Interpretation of these data.

The observations mentioned above suggest the implicit existence of edge forces. An analysis of the numerical methods reveals the following (section 6.1):

Lee & Greenberg postulate that the leading edge of the vortex sheets, which originate at the strip edges, consists of a square root singularity in the vortex sheet strength γ . Such a singularity implies a discrete leading edge suction force, by which their method does not represent an actuator disc with a uniform load, as suggested by the authors. Schouten's method is similar: in his numerical model he uses a discrete vortex to model the leading edge of the vortex sheet. This implies a discrete force to be present if the local velocity at the edge is non-zero. Consequently the results of both methods do not raise the question whether the edge force is inherently connected to the

actuator disc. On the other hand they confirm numerically the statement that adding edge forces improves the modeling of a rotor by an actuator disc.

Concerning the numerical work found in literature, only Madsen's method cannot be interpreted; also the experimental work of Lee & Greenberg and Castro needs to be explained. We will return to this later on.

Our own numerical approach.

A non-linear, viscous finite element calculation has been performed in order to study the flow induced by smooth force fields in absence of an ambient flow (Peters [1989], section 6.2). The actuator disc flow with a uniform surface load is approached by increasing both the Reynolds number and the steepness of the load distribution as far as possible. By systematic variation of the calculation area and of the size and distribution of the grid cells, the influence of the numerical method on the results has been minimized. The calculations have been performed for both a 2-D actuator strip and a 3-D actuator disc. The 3-D results confirm the 2-D results, presented here:

- the Reynolds number is defined on the basis of the strip length L and the centerline velocity far downstream $u_{\text{far wake}} = \sqrt{2F/\rho}$, with F as the strip load at the symmetry line. The maximum Re number used is 2600. The increase of Re above 1500 appears to hardly affect the calculated power and average velocity through the strip. The increase of the steepness of the load distribution near the edges, meanwhile maintaining the same resultant thrust, yields an increase of calculated power; the increase itself becomes smaller and smaller for increasing steepness.
- for each distribution, the limit value of the power $P/P_{\text{classical}}$ for $\text{Re} \rightarrow \infty$ has been determined by extrapolation. These 'inviscid' data are used to extrapolate the value of the power ratio for infinite steepness at the edges: the step function distribution. The value so found is 1.01 ± 0.02 , so no significant deviation from the classical prediction is found.
- the numerical calculations allow an interpretation of the experiments of Lee & Greenberg [1984]: the position of minimum pressure and the velocity profile at the strip are reproduced satisfactorily. This is achieved by assuming a finite thickness of the strip and a non-uniform load distribution. The calculated average velocity through the strip is 3.5% higher than predicted by the classical momentum theory, which agrees with the experimental value which is 4% higher. However, it has to be noted that we did not investigate the significance of this 3.5% deviation as we did in the other calculations described above. Lee & Greenberg assume the strip to be infinitely thin with a uniform load. They need to introduce an 'effective' strip length

in their numerical method to be able to interpret the experiments. Our result indicates that the experimental set-up, although intended to represent a constant load actuator strip, is better represented by a strip with a non-uniform load having a finite thickness.

The latter calculation shows that, using our numerical method, the velocity through a disc or strip with a non-uniform load distribution can exceed the maximum value set by Froude's concept. The explanation for this is that for such a non-uniform load the thrust converting power can be smaller than the total thrust (section 3.3). This depends on the distribution of the velocity which is not known a priori. If $T > T_{\text{work}}$, the disc with a non-uniform load distribution is better represented by a disc with edge forces of appropriate strength, than by a disc according to Froude's concept, since this does not allow the inequality of T and T_{work} .

Comparison of the present numerical work with Madsen's results.

Concerning the numerical work one interpretation problem remains: the extrapolation of our data for increasing steepness are in agreement with the classical momentum theory, while Madsen's result exceeds the classical power prediction by 4%.

The common points in both methods are: both use finite elements, proceeding from a smooth load distribution. The computational domain of both methods has approximately the same size, and increasing the domain yields similar results. The differences are : Madsen's method is inviscid, while the load is distributed on an infinitely thin cylinder. The load decelerates the ambient parallel flow. In our calculations the flow is viscous and induced by a load on a strip with thickness, in absence of an ambient flow. Finally Madsen's resultant load distribution is 2.8 times steeper than the maximum steepness used in the present calculations. Remaining differences may concern numerical dispersion in the method of Madsen, details of which are not known to the author. The discussion on the numerical work is continued in the next section.

The analytical approach: the equation of motion.

This concerns the generation of vorticity by force fields, distributed on 2-D actuator strips and 3-D actuator discs, the latter without azimuthal forces and velocities (except in section 7.2). The equation of motion is (section 5.1):

$$\nabla H = \underline{f} + \rho \underline{v} \times \underline{\omega} - \rho \partial \underline{v} / \partial t \quad , \quad (5-5)$$

and the generation of vorticity is described by the curl of it:

$$\frac{D\omega}{Dt} = \frac{1}{\rho} \nabla \times \mathbf{f} \quad (5-6)$$

where we used $(\omega \cdot \nabla) \mathbf{v} = 0$ since \mathbf{v} has no component in the direction of ω . The usual interpretation of \mathbf{f} is that it represents the externally applied force density, but it may contain the internal force density $\mathbf{f}_{\text{shear stress}} = \mu \nabla^2 \mathbf{v}$ as well: written dimensionlessly and expressed in the vorticity ω , this term equals $\text{Re}_L^{-1} \nabla \times \omega$, which leaves the possibility that it remains finite for $\text{Re}_L \rightarrow \infty$ if $\nabla \times \omega$ becomes infinite. Here L denotes the length or radius of the surface. A sudden increase of ω on a streamline passing an infinitely thin actuator strip yields such an infinite value.

Three examples of steady flow where $D\omega/Dt \neq 0$ indeed show that a tangential (in plane) component of the force density \mathbf{f} is required in order to satisfy (5-5): the flow along a solid wall (where $D\omega/Dt \neq 0$ implies the no-slip condition), an exact solution of Wu's actuator disc equation, namely a solid body rotation of the cylindrical wake, and the flow induced by an actuator surface with a smooth load distribution (appendix F, section 7.1 and 7.2 respectively). In case of the flow along a solid wall, this is verified by performing the limit $\text{Re}_L \rightarrow \infty$ with respect to Prandtl's boundary layer equation's: indeed the shear stress at the surface remains $O(1)$. Since the thickness on which $\mathbf{f}_{\text{shear stress}}$ is distributed is zero for $\text{Re}_L \rightarrow \infty$, it does not contribute to the resultant load. The exact solution of Wu's equation shows the same feature: applying a normal and azimuthal surface load F_x and F_φ respectively, requires a radial force density $f_r = O(1)$ to be present. If the thickness is non-zero, even a radial surface load $F_r = O(\epsilon)$ results. The flow induced by a smooth actuator surface force field also requires a tangential force density f of $O(1)$. Again for a non-zero thickness ϵ this results in a tangential surface load F of $O(\epsilon)$.

The uniform, normal load distribution.

An infinitely thin actuator surface covered with a constant, normal load $F = \int f \, d\mathbf{n}$, where \mathbf{n} is directed normal to the surface and $f = \delta(\mathbf{n}) F$, induces a singular flow at the edge since $\nabla \times \mathbf{f}$ is singular: this singularity is a discrete vortex (section 8.1). If $\bar{\mathbf{v}}$, the velocity averaged on the edge area, is zero, the vorticity generated according to (5-6) accumulates at the edge, and an unsteady flow results. A steady flow requires a non-zero value of $\bar{\mathbf{v}}$ at the singularity; this velocity transports the vorticity downstream along the vortex sheet which emerges from the edge. Since the vortex is

fixed, it carries a force $-\rho \bar{v} \times \Gamma$. The order of magnitude is the order of \bar{v} , which is known to be non-zero in case of a steady flow, but still can be infinitely small. The order cannot be derived by local considerations alone, and awaits an analytical or numerical approach to determine the entire flow field including the singularity.

Comparison with other edge singularity solutions.

In the literature, two edge singularity solutions are known: Greenberg [1972] and Lee & Greenberg [1984] use the square root singularity in the vortex sheet strength γ , and Schmidt & Sparenberg [1977] derive a 2-D spiraling flow as edge flow. The square root singularity is shown to require a non-zero radius of curvature of the sheet near the edge, in order to be a solution of the governing integral equation (section 8.3). Furthermore, such a singularity is connected to either infinite or zero pressure jumps; it is incompatible with a finite pressure jump as at the uniform load surface. The spiral flow of Schmidt & Sparenberg is an analytical solution for a semi-infinite spiralling vortex sheet having its core at the edge of the actuator strip. We have derived the same solution by starting with a finite spiral flow, after which the length is increased to infinity. This yields the flow conditions at infinity, which are unknown in the method of Schmidt & Sparenberg. These conditions show that a 2-D description of the flow is not possible, since the solution requires a multi-branched Riemann surface. Looking at one turn of this surface yields a 2-D description, but then the equation of motion is not satisfied at infinity.

9.2 Discussion on the results

The results presented in the previous section give cause to discussion, and generate questions. These mainly concern the results of Part II: the actuator surface problem.

- In comparing experimental and numerical actuator surface results with the classical performance prediction, interpretation problems remain regarding Castro's strip experiment and the numerical work of Madsen and of ourselves. The interpretation of experiments and numerical work from literature is difficult, so maybe the contradiction is only apparent. Castro's and Madsen's data suggest that the classical prediction is not an upper bound, while our data comply with this prediction. It should be remembered that the classical prediction is based on a uniform load distribution, so surfaces with a non-uniform load may exceed this prediction. The

distribution on Madsen's cylinder is non-uniform; the distribution on the strip in Castro's experiment is not known. The distribution on our strip and disc is also non-uniform, but much smoother than Madsen's distribution. This difference might also explain the different results. This can be verified by performing a calculation with our program using Madsen's distribution. However, this was not possible for several, practical reasons.

The occurrence of an in-plane force density at a surface where vorticity is generated (the solution of Wu's equation, the flow along a solid boundary and the flow induced by a smooth actuator surface force field) is remarkable. For the flow along the solid boundary the origin of this is identified as the remainder of the viscous term in the Navier-Stokes equation for $Re_L \rightarrow \infty$, with L as characteristic length scale. For the actuator surface flows with zero thickness ϵ the same interpretation is possible, since then $\nabla \times \underline{\omega}$ becomes infinite on streamlines experiencing a jump in vorticity while passing the surface. In that case the order of the shear stress at the surface, expressed as $\nu \nabla \times \underline{\omega}$, can remain finite for $Re_L \rightarrow \infty$. This reasoning only offers an explanation, but not a confirmation as was obtained in case of the boundary layer flow. Furthermore this explanation does not hold for surfaces with a non-zero thickness: then $\nabla \times \underline{\omega}$ remains finite so the shear stress $\nu \nabla \times \underline{\omega}$ vanishes anywhere for $\nu \rightarrow 0$. Yet we have found that applying a non-uniform, normal load on an actuator surface requires a non-zero tangential load to be present. We do not have an explanation on solid grounds for this, but only the following hypothesis. The flow through an actuator surface and the boundary layer flow along a solid surface have in common that vorticity is generated by the force field distributed on the surface. For the boundary layer flow it is clear that a finite thickness of the layer is coupled to a finite value of the Reynolds number. Assuming the velocity and length in the Reynolds number to be finite, this implies a finite value of ν . Probably the same is true for actuator surfaces. In our approach the limits of vanishing thickness and vanishing viscosity are uncoupled. If we assume that they are coupled as in the boundary layer flow, a finite thickness of the actuator surface combined with a finite value for ν yields a resultant shear stress load at the surface. If the order of ν is small enough for the diffusion of vorticity to be negligible, we arrive at the situation that the shear stress is negligible everywhere in the flow, except at the actuator surface. This would explain the occurrence of the shear stress load. To make this line of arguments more than an hypothesis, an analytical description of the limits $\epsilon \rightarrow 0$ and $\nu \rightarrow 0$ for the actuator surface flow is required, starting from the Navier-Stokes

equation.

- The derivation of the edge singularity being a vortex is valid for the actuator strip as well as the disc. In the latter case, a discrete vortex ring is present, which is known to have an infinite self-induced velocity. This clearly conflicts the assumption of steady flow for which it has been derived. However, the vortex is the leading edge of a vortex sheet which spirals around the vortex. The velocity induced by the vorticity contained in the spiral may cancel this own-induced velocity. This can be confirmed only by an analytical asymptotic method which accounts for the entire flow field, or by a numerical procedure. Concerning the actuator strip, this problem does not exist.
- In the mathematical proof of the possible existence of a force on the edge of an actuator with constant load one essential step is missing: the determination of the order of magnitude of \bar{v} at the edge. The question whether $\bar{F} = -\rho \bar{v} \times \Gamma = O(1)$, so has a finite magnitude, or $o(1)$, so can be infinitely small, cannot be solved by local considerations alone. The answer awaits either an analytical approach including the far field, or a new numerical method allowing steeper distributions for the force density.

If the edge force should appear to be an inherent part of the load, the interpretation of it's origin is not complete. It is obvious to look at the shear stress as in case of smooth distributions of the actuator surface load. However, we do not know the order of the shear stress term $\nu \nabla \times \omega$ in the flow singularity at the edge.

Furthermore, the extrapolation of the data of our numerical work towards a strip with a constant load, confirms the power prediction based on Froude's concept, which excludes edge forces. The question whether this extrapolation changes if more data are accounted for, cannot be answered now since our numerical method does not allow very steep distributions of the force field..

The only indication we have that the edge force has a finite order of magnitude comes from the reduction ad absurdum proof in appendix D. This proof proceeds from an actuator strip, having a resultant thrust T perpendicular to the undisturbed flow U_0 . The assumption is made that the flow induced by this strip must become a vortex flow if the strip is submitted to a limit of vanishing dimensions, meanwhile keeping T constant and perpendicular to U_0 . We showed that Froude's concept can not yield this vortex flow as a result of this limit: the thrust T can be maintained finite in the limit only if an infinite amount of energy is converted to or from the flow. The strip with edge forces submitted to the same limit does yield the

possibility that the required vortex flow results. The weak point of this proof is that it depends on several assumptions. Therefore the question whether the edge force is finite remains unanswered.

9.3 Conclusions

The final conclusions are:

- The representation of a rotor by an actuator disc with edge forces improves the performance prediction significantly. The momentum theory based on Froude's concept proceeds from an invalid assumption if applied to rotors: only a part of the thrust converts power to or from the flow. Both statements are confirmed by the experiment on the model rotor in hover. A general quantitative performance prediction is not possible yet, since the ratio of total thrust to thrust converting power is not known. For a wind turbine the representation of the rotor by the disc with edge forces implies that the maximum attainable efficiency is higher than the classical Lanchester-Betz limit 0.59.
- The experimental result of Castro [1971] and the numerical results of Madsen [1985] cannot be explained by the momentum theory based on Froude's concept. The addition of edge forces to this concept yields a shift of the performance prediction which then allows an interpretation of these experiments.
- The extrapolation of our numerical data of viscous flows through strips with smooth load distributions, towards the inviscid flow induced by an actuator strip with a uniform load complies with the classical results, based on Froude's concept without edge forces. However, this extrapolation can change if more data are accounted for, which was not possible with our method. An indication for this is that Madsen's result exceeds the classical result, which should not be possible according to our extrapolation.
- The experimental data of Lee & Greenberg [1984] are confirmed by our calculations, while an analysis of their edge singularity yields an interpretation of their numerical data. Both subjects were not clarified satisfactorily by the authors.
- The actuator surface force field is not completely free to choose: if the surface is covered with a smooth, normal surface load, an in-plane force density must be present. For surfaces with a non-zero thickness this force density results in a finite in-plane surface load. An exact solution of Wu's actuator disc equation has been

found which confirms these features. For the special case of the generation of vorticity at a solid boundary, also the tangential force density has been found. By comparison with the boundary layer equations at an infinite Reynolds number, this force density is identified as the remainder of the shear stress.

- The edge singularity of an infinitely thin actuator surface with a constant, normal load is determined to be a vortex. If the flow is steady, the vortex experiences a discrete force which is non-zero, but has an unknown order of magnitude.

REFERENCES

- Abramowitz, M., Stegun, I.A., 1965
Handbook of mathematical functions
Dover publications, New York.
- Beekman, P., 1985
Measurements on a helicopter rotor (in Dutch)
Department of Physics, Technical University Eindhoven, Report R 764 S.
- Bergey, K.H., 1979
The Lanchester-Betz limit; Journal of Energy, Volume 3, no. 6, p. 382.
- Betz, A., 1920
Das Maximum der theoretisch möglichen Ausnützung des Windes durch
Windmotoren; Zeitschrift für das gesamte Turbinenwesen, Volume 26, p. 307.
- Bussel, G.J.W. van, Kuik, G.A.M. van, 1985
Rotor aerodynamics of horizontal axis wind turbines, proceedings of a NEWIN
workshop (in Dutch)
Department of Physics, Technical University Eindhoven, Report R 738 D.
- Castro, I.P., 1971
Wake characteristics of two-dimensional perforated plates normal to an
air-stream
Journal of Fluid Mechanics, Volume 46, part 3, p. 599.
- Courant, R., Hilbert, D., 1968
Methoden der mathematischen Physik
Springer Verlag.
- Drzewiecki, S., 1920
Théorie Générale de l'Hélice
Paris.
- Froude, R.E., 1889
On the part played in propulsion by differences of fluid pressure
Transactions of the Institute of Naval Architects, Volume 30, p. 390.
- Glauert, H., 1935
Aerodynamic Theory edited by Durand, Volume IV division C chapter XI,
Springer. Reprinted in 1963 as a Dover edition.
- Gray, R.B., McMahon, H.M., Shenoy, K.R., Hanimer, M.L., 1980:
Surface pressure measurements at two tips of a model helicopter rotor in hover
NACA CR-3281.

- Greenberg, M.D., 1972
Non-linear actuator disc theory
Zeitschrift für Flugwissenschaften, Volume 20, no. 3, p. 90.
- Helden, W. van, 1988
A numerical calculation of the flow through the actuator strip
Department of Physics, Technical University Eindhoven, Report R-898-A.
- Hoerner, S.F., Borst, H.V., 1985
Fluid Dynamic Lift
Hoerner Fluid Dynamics, Brick Town N.Y.
- Hoek, H. van der, Pel, L., 1987
Verification of the momentum theory for rotors by measurements on a model rotor (in Dutch)
Department of Physics, Technical University Eindhoven, Report 840 S.
- Holten, Th. van, 1981
Concentrator systems for wind energy, with emphasis on tip vanes
Wind Engineering, Volume 5, no. 1, p. 29.
- Hütter, U., 1977
Optimum wind energy conversion systems
Annual Review of Fluid Mechanics, Volume 9, p. 399.
- Johnson, W., 1980
Helicopter Theory
Princeton University Press.
- Kármán Th. von, Burgers, J.M., 1935
Aerodynamic Theory edited by Durand, Volume II division E, Springer.
Reprinted in 1963 as a Dover edition.
- Kocurek, J.D., Tangler, J.L., 1977
A prescribed wake lifting surface hover performance analysis
Journal of the American Helicopter Society, Volume 22, no. 1, p. 89.
- Küchemann, D., 1978
The aerodynamic design of aircraft
Pergamon Press.
- Kuik, G.A.M. van, Bussel, G.J.W. van, Kusters, R.M., 1985a
A survey of the aerodynamics of wind turbines: after 100 years still enough to do (in Dutch)
Proceedings of the National Wind Energy Conference, Noordwijkerhout, the Netherlands
- Kuik, G.A.M. van, 1985b
On the improvement of the axial momentum theory for rotors (in Dutch)
Proceedings of the National Wind Energy Conference, Noordwijkerhout, the Netherlands

- Kuik, G.A.M. van, 1986
The physics and mathematical description of the achilles heel of stationary wind turbine aerodynamics: the tip flow
Proceedings of the European Wind Energy Conference, Rome, Italy.
- Kuik, G.A.M. van, 1987
The actuator disc edge singularity; the key to a revised actuator disc concept and momentum theory
Proceedings of the 13th European Rotorcraft Forum, Arles, France.
- Kuik, G.A.M. van, 1988
The performance of an ideal wind turbine (in Dutch)
Proceedings of the National Wind Energy Conference, Noordwijkerhout, the Netherlands.
- Kuik, G.A.M. van, 1989a
On the revision of the actuator disc momentum theory
Proceedings of the European Wind Energy Conference, Glasgow, Scotland.
- Kuik, G.A.M. van, 1989b
Experimental verification of an improved actuator disc concept
Proceedings of the 15th European Rotorcraft Forum, Amsterdam, the Netherlands.
- Lanchester, F.W., 1915
A contribution to the theory of propulsion and the screw propeller
Transactions of the Institution of Naval Architects, Volume 57, p. 98.
- Lee, J.H.W., Greenberg, M.D., 1984
Line momentum source in shallow inviscid fluid
Journal of Fluid Mechanics, Volume 145, p. 287.
- Madsen, H.A., 1985
The actuator cylinder: a flow model for vertical axis wind turbines
Proceedings of the 7th British Wind Energy Conference.
- Madsen, H.A., 1988
Personal communication.
- Meyer, R.E., 1982
Introduction to mathematical fluid dynamics
Dover Publications, a reprint of a John Wiley & Sons publication of 1971.
- Peters, M.C.A.M., 1989
The actuator disc with a uniform, axial load distribution: a critical study on 100 years doctoring on the classical theory (in Dutch)
Department of Physics, Technical University Eindhoven, Report R-982-A.
- Pol, B. van de, Bremmer, H., 1964
Operational Calculus, Cambridge University Press

- Prandtl, L., 1919
Appendix to the paper of A. Betz: Schraubenpropeller mit geringstem Energieverlust,
Göttinger Nachrichten, p.193
- Rankine, W.J.M., 1865
On the mechanical principles of the action of propellers
Transactions of the Institution of Naval Architects, Volume 6, p. 13.
- Schmidt, G.H., Sparenberg, J.A., 1977
On the edge singularity solution of an actuator disk with large constant normal load
Journal of Ship Research, Volume 21, no. 2, p 125.
- Schouten, G., 1983
On the analytical solution of the 2-D actuator surface problem
Department of Aerospace Engineering, Technical University Delft, report LR-311.
- Schijndel, C.M.M., van, 1987
Measurements on a helicopter rotor (in Dutch)
Department of Physics, Technical University Eindhoven, Report R 862 S.
- Sparenberg, J.A., 1984
Elements of hydrodynamic propulsion
Martinus Nijhoff Publishers.
- Segal, G., 1987
SEPRAN introduction, user manual, standard problems, programmers guide
- Spek, A.M. van der, 1986
Linear and non-linear theories of flow through an actuator disk
Department of Physics, Technical University Eindhoven, Report R 803 A.
- Stoddard, F.S., 1977
Momentum theory and flow states for windmills
Wind Technology Journal, Volume 1, no. 1, p. 3.
- Thwaites, B., 1960
Incompressible aerodynamics
Clarendon Press, Oxford
- Vermeulen, P.E.J., 1979
Studies of the wake structure of model wind turbine generators
Netherlands Organization for Applied Scientific Research TNO, Department of Fluid Flow Technology, Report 79-012904/LTN.
- Viterna, L.A., Corrigan, R.D., 1981
Fixed pitch rotor performance of large horizontal axis wind turbine
Proceedings of the workshop Large Horizontal Axis Wind Turbines, NACA CP-2230.

- Vries, O. de, 1979
Fluid dynamic aspects of wind energy conversion
AGARDograph no. 243.
- Wilson, R.E., Lissaman, P.B.S., Walker, S.N., 1976
Aerodynamic performance of wind turbines
Oregon State University.
- Wu, T.Y., 1962
Flow through a heavily loaded actuator disc
Schiffstechnik, Volume 9, no. 47, p. 134.

Appendix A

SPARENBERG'S TRANSLATION THEOREM

Actuator surfaces with constant, normal surface load exhibit a peculiar property (see Sparenberg [1984]): the position of the surface is not important for the flow field generated by the force field, as long as the edge of the surface remains at the same place. Sparenberg derived this theorem for surfaces which are infinitely thin. Here we proceed from surfaces with thickness, after which the limit of vanishing thickness is taken.

Figure A.1 shows two actuator strips (or cross-sections through 3-D actuator discs without azimuthal forces and velocities, see section 7.2) having the same edge, defined by $r \leq \epsilon/2$. The center of the edge is the origin of the cartesian (x,y) coordinate system and the cylindrical (r,θ) coordinate system, see figure A.1. The surfaces have the same constant, normal load outside the edge region:

$$F_1 = F_2 \quad \text{with } \underline{F} = \int_{\epsilon} \underline{e}_x f(x) dx \quad . \quad (A-1)$$

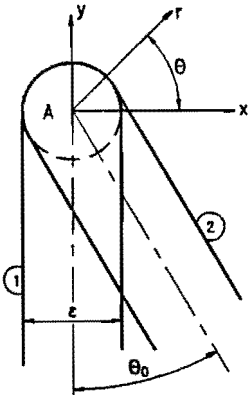


Figure A.1. Two force field distributions, having the same edge.

The distribution function $f(x)$ is the same for both force fields; for $\epsilon \rightarrow 0$ it becomes a delta function: $f(x) = \delta(x) F$. At the edges, the distribution of the force density is not prescribed. However, for all edge distributions (8-4) shows that

$$\iint_{A_1} (\nabla \times \mathbf{f})_1 dA = \iint_{A_2} (\nabla \times \mathbf{f})_2 dA, \quad (\text{A-2})$$

where A_1 and A_2 are the edge areas. Since A_1 equals A_2 , (8-5) shows for $\epsilon \rightarrow 0$:

$$(\nabla \times \mathbf{f})_1 = (\nabla \times \mathbf{f})_2 = O(\epsilon^{-2}), \quad (\text{A-3})$$

so by (8-6):

$$\frac{D\omega_1}{Dt} = \frac{D\omega_2}{Dt}. \quad (\text{A-4})$$

Equation (A-4) results in two identical flow fields, if the start and boundary conditions are equal. By assuming identical undisturbed flows at the start of the action of the force fields, these conditions are satisfied. As far as the pressure field is concerned, this remains the same outside the region enclosed by the two surfaces, and differ F in the enclosed region.

In this way, the flow induced by a plane actuator surface is identical with the flow of an actuator surface aligned with the vortex sheets up to downstream infinity, where the surface crosses the wake, figure A.2. The Bernoulli constant H has the same value throughout the flow field, and the sheets maintain a constant pressure jump Δp . The kinematical problem has been transferred to a potential flow problem of finding the shape of the vortex sheets.

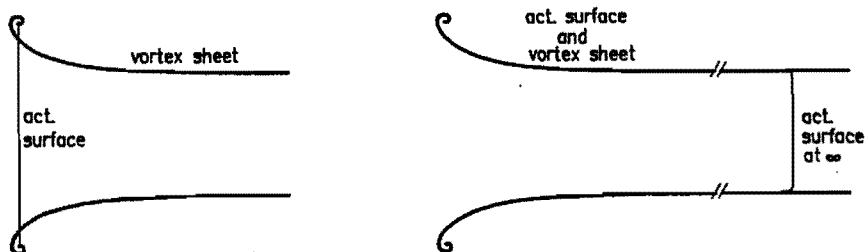


Figure A.2. Two actuator surfaces generating the same flow field.

Appendix B

THE EXPONENTIAL SPIRAL WITH INFINITE LENGTH AS THE LIMIT OF A FINITE LENGTH SPIRAL

In section 8.3.1 the flow around an infinitely long exponential spiral $r = e^\theta$ is described. Schmidt & Sparenberg [1977] found this flow by conformal transformation of the flow of Figure 8.2b.

Schouten [1983] derived this flow by conformal transformation of the flow around a semi-infinite flat plate in the ζ -plane, figure B.1, using the transformation:

$$z^{1-i} = \zeta . \quad (\text{B-1})$$

We try to establish the flow around the semi-infinite spiral by first determining the flow around a finite spiral, after which the length of the spiral is increased to infinity. This finite spiral is obtained by transformation of the finite flat plate flow (figure B.2), using a similar transformation.

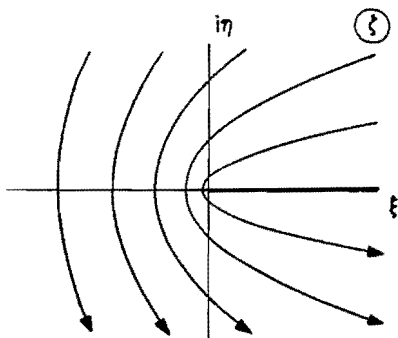


Figure B.1 The flow around a half-infinite plate

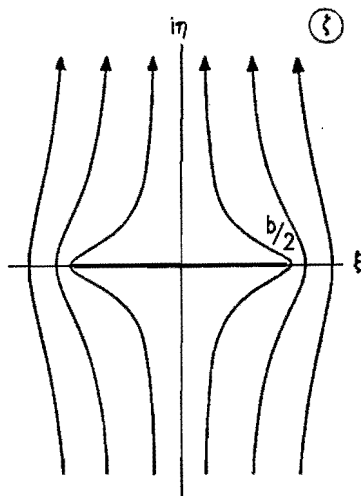


Figure B.2 The flow around a finite plate

After some trial and error we find that the transformation

$$z^{1-i} = \zeta^4 \tag{B-2}$$

maps the flat plate into a finite length spiral, as we will show. With $\zeta = \rho e^{i\varphi}$ and $z = re^{i\Theta}$ (B-2) becomes:

$$re^{\Theta} e^{i(\Theta - \ln r + k_1 2\pi)} = \rho^4 e^{i(4\varphi + k_2 2\pi)},$$

or:

$$re^{\Theta} e^{i(\Theta - \ln r)} = \rho^4 e^{i4(\varphi + k \frac{\pi}{2})}, \tag{B-3}$$

by which:

$$\left. \begin{aligned} \Theta &= 2 \ln \rho + 2 \left(\varphi + k \frac{\pi}{2} \right) \\ \ln r &= 2 \ln \rho - 2 \left(\varphi + k \frac{\pi}{2} \right) \end{aligned} \right\} \tag{B-4}$$

where k , k_1 and k_2 are integers. We choose k to be zero. Then the semi flat plate defined by $\rho \leq b/2$, $\varphi = n \pi$ (n integer) is transformed to a finite length spiral:

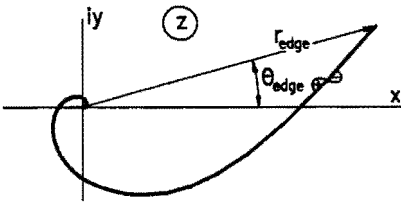


Figure B.3 The exponential spiral with finite length

$$r = e^{\Theta - 4n\pi} = \rho^2 e^{-2n\pi} \quad \rho \leq \frac{b}{2} \quad (B-5)$$

The position of the edge is given by

$$\left. \begin{aligned} r_{\text{edge}} &= \left[\frac{b}{2} \right]^2 e^{-2n\pi} \\ \Theta_{\text{edge}} &= \ln \left[\frac{b}{2} \right]^2 + 2n\pi \end{aligned} \right\} \quad (B-6)$$

and the length ℓ is

$$\ell = \int_{-\infty}^{\Theta_{\text{edge}}} \sqrt{r^2 + \left[\frac{dr}{d\Theta} \right]^2} d\Theta = \sqrt{2} e^{-2n\pi} \left[\frac{b}{2} \right]^2 \quad (B-7)$$

Figure B.3 shows one mapping of the exponential spiral. For increasing b the spiral remains at the same place, but continues itself along the line $r=e^\theta$. The kernel of the spiral is the transformation of the origin of Figure B.2. The mapping (B-2) or (B-4) is multivalued: each period $\Theta_0 \leq \Theta \leq \Theta_0 + 2\pi$ in the z -plane is the transformation of one quadrant of the ζ -plane. Although the flat plate flow is symmetric with respect to the imaginary axis, the spiral flow does not have a periodicity as the scale of the transformation is a function of φ : for example the positions $\rho = b/2$, $\varphi = 0$ respectively 2π in the ζ -plane are mapped to different radial positions in the z -plane, differing $e^{-4\pi}$ as can be seen from (B-6). With k chosen to be zero in (B-4), the mapping of the flat plate flow in the ζ - plane requires four turns of the Riemann surface. Figure B.4 shows the flow in these turns, being the mapping of the flow in the quadrants in the z - plane defined by $-\pi/2 \leq \varphi \leq 0$, $0 \leq \varphi \leq \pi/2$, $\pi/2 \leq \varphi \leq \pi$, $\pi \leq \varphi \leq 3\pi/2$. These quadrants and corresponding turns of the Riemann surface are numbered -1, 1, 2, 3 respectively. The branch line of the Riemann surface coincides with the spiral and its continuation. The spiral flow pattern on turns -1 and 2, and on turns 1 and 3 are identical except for the scale and the direction of the streamlines: for example the scale of turn 3 is $e^{-2\pi} \approx 0.002$ times the scale of turn 1.

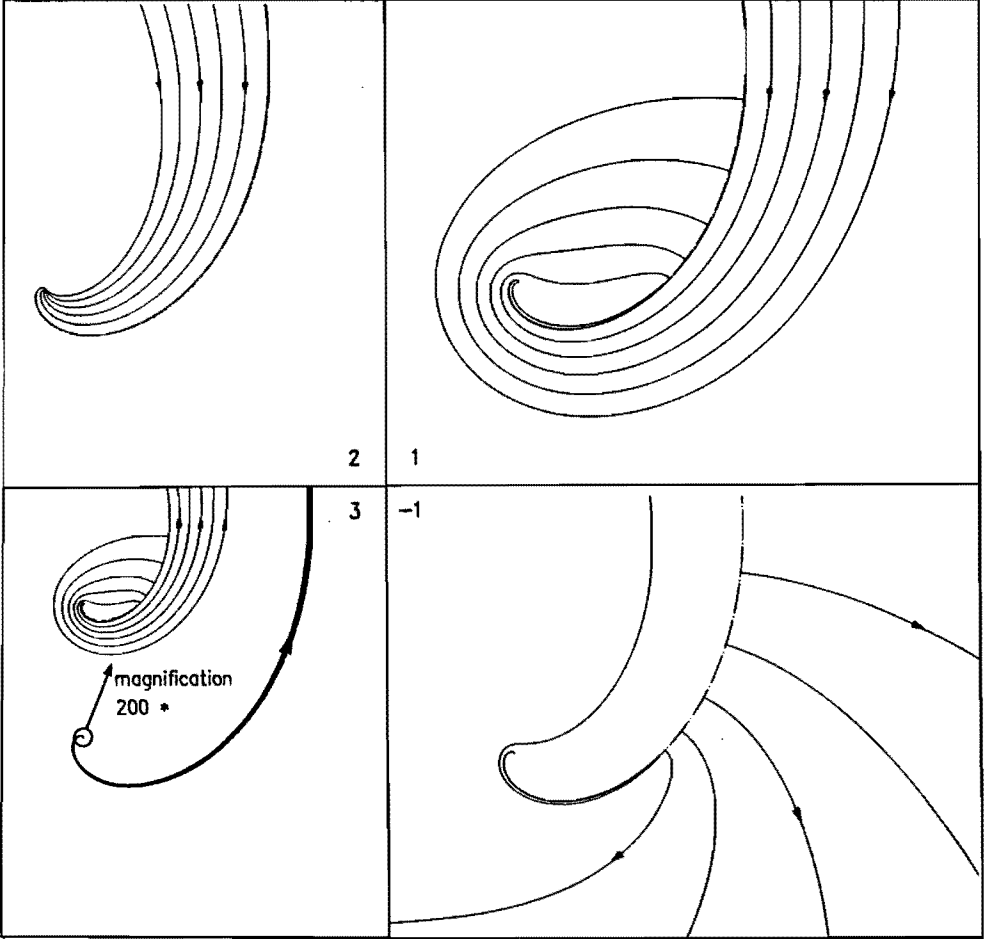


Figure B.4. The flow in the s -plane which is the result of the mapping of the flow of figure B.5. The flow pattern numbered -1 corresponds with the quadrant -1 in figure B.5, and so on. Apart from the scale and the orientation, patterns -1 and 2 are equal, as are patterns 1 and 3. This is illustrated by the magnification of the center of pattern 3. The branch line of the Riemann surface is indicated by - - - - .

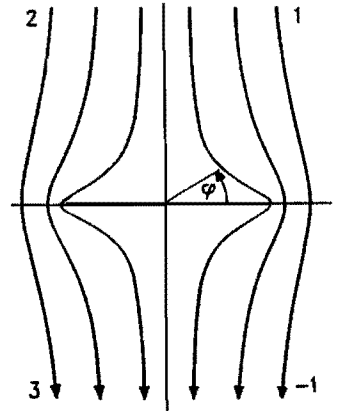


Figure B.5. The flow around the flat plate. The definition of the quadrants is:
 - 1 : $-\pi/2 \leq \varphi \leq 0$
 1 : $0 \leq \varphi \leq \pi/2$
 2 : $\pi/2 \leq \varphi \leq \pi$
 3 : $\pi \leq \varphi \leq 3\pi/2$

The complex potential of the flat plate flow is:

$$\chi(\zeta) = i U_0 \sqrt{\zeta^2 - \left[\frac{b}{2}\right]^2} \tag{B-8}$$

Substitution of the transformation (B-2) yields the complex potential of the spiral flow in the z -plane:

$$\chi(z) = i U_0 \sqrt{z^{\frac{1-i}{2}} - \left[\frac{b}{2}\right]^2} \tag{B-9}$$

The behaviour of the complex potential for $b \rightarrow \infty$ is shown by the Taylor expansion with respect to b^{-1} :

$$\begin{aligned} \chi(z) &= -U_0 \frac{b}{2} \left[1 - \frac{1}{2} \frac{z^{\frac{1-i}{2}}}{\left[\frac{b}{2}\right]^2} + \dots + \dots \right] \\ &= -U_0 \frac{b}{2} + \frac{U_0}{b} z^{\frac{1-i}{2}} - \dots + \dots \end{aligned} \tag{B-10}$$

Apart from the constant term, the first term in (B-10) equals the complex potential (8-15) of the Schmidt & Sparenberg spiral flow. This infinite-spiral-flow appears to be the first relevant term in the series expansion of the finite-spiral-flow with respect to the $(\text{length})^{-1}$. At the same time we have determined the constant c in the solution of Schmidt & Sparenberg: $c = U_0/b$. Only if this ratio is kept constant in the limit for increasing spiral length, a non-trivial flow results. We will elaborate this special case in the following analysis.

We consider the entire Riemann surface instead of one turn with a branch line. Then both sides of the spiral, denoted by $+$ and $-$ according to figure B.3, are characterized by the same r and Θ . Consequently the complex potential χ , the magnitude of the velocity $|d\chi/dz|$ and the pressure do not exhibit a jump across the spiral. This may be different if we consider only one turn, with the branch line coinciding with the spiral as

in figure B.4. Then Θ_+ and Θ_- differ 2π . The complex potential (B-9) is used to determine the velocity and pressure jump across the spiral. The + and - sides of the spiral are defined by:

$$\left. \begin{aligned} r &= e^{\Theta} = r_+ = r_- \\ \Theta_+ &= \Theta \\ \Theta_- &= \Theta + 2\pi \end{aligned} \right\} \quad (\text{B-11})$$

which corresponds with figure B.4, turn 1. The velocity is given by:

$$\frac{d\chi}{dz} = v_x - iv_y = \frac{U_0}{4} (1+i) \frac{z^{\frac{-1-i}{2}}}{\sqrt{z^{\frac{1-i}{2}} - \left[\frac{b}{2}\right]^2}} \quad (\text{B-12})$$

At the + side,

$$\begin{aligned} (v_x - iv_y) &= \frac{U_0}{4} (1+i) \frac{e^{-\frac{\Theta}{2}} (1+i)^2}{\sqrt{e^{\frac{\Theta}{2}} (1+i) (1-i) - \left[\frac{b}{2}\right]^2}} \\ &= \frac{U_0}{4} \frac{e^{\frac{i\pi}{4}}}{\frac{1}{2} \sqrt{2}} \frac{e^{-i\Theta}}{\sqrt{e^{\Theta} - \left[\frac{b}{2}\right]^2}} \\ &= \frac{U_0}{2\sqrt{2}} \frac{\sin\left[\frac{\pi}{4} - \Theta\right] - i \cos\left[\frac{\pi}{4} - \Theta\right]}{\sqrt{\left[\frac{b}{2}\right]^2 - e^{\Theta}}}, \end{aligned} \quad (\text{B-13})$$

so:

$$|v_+| = \frac{U_o}{2\sqrt{2}} \frac{1}{\sqrt{\left[\frac{b}{2}\right]^2 - e^\Theta}} \quad (\text{B-14})$$

In the same way $|v_-|$ is determined with $r_- = r_+$ and $\Theta_- = \Theta_+ + 2\pi$ according to (B-11):

$$|v_-| = \frac{U_o}{2\sqrt{2}} \frac{e^\pi}{\sqrt{\left[\frac{b}{2}\right]^2 + e^\Theta e^{2\pi}}} \quad (\text{B-15})$$

Using (B-14) and (B-15), the pressure jump is:

$$\frac{\Delta p}{\frac{1}{2}\rho U_o^2} = -\frac{1}{8} \left[\frac{1}{\left[\frac{b}{2}\right]^2 - e^\Theta} - \frac{e^{2\pi}}{\left[\frac{b}{2}\right]^2 + e^\Theta e^{2\pi}} \right] \quad (\text{B-16})$$

After substitution of (B-6) this becomes:

$$\frac{\Delta p}{\rho} = -\frac{1}{4} \left[\frac{U_o}{b} \right]^2 \left[\frac{1}{1 - e^{\Theta - \Theta_{\text{edge}} + 2\pi}} - \frac{e^{2\pi}}{1 + e^{\Theta - \Theta_{\text{edge}}}} \right] \quad (\text{B-17})$$

For large negative values of $(\Theta - \Theta_{\text{edge}})$, so for $b \rightarrow \infty$ or $\Theta \rightarrow -\infty$, this simplifies to

$$\frac{\Delta p}{\rho} = -\frac{1}{4} \left[\frac{U_o}{b} \right]^2 (1 - e^{2\pi}), \quad (\text{B-18})$$

and we have recovered expression (8-15) derived by Schmidt & Sparenberg, with $c = U_o/b$. This means that indeed their infinite spiral flow can be obtained from a finite spiral flow by increasing the length of the spiral to infinity. However, the segment of the branch line which does not coincide with the spiral but is the continuation of it, cannot be removed from the flow field. Therefore the flow discontinuity at the branch line B.4 remains. This implies that a description of the flow in the 2-D plane is impossible: at infinity the equations of motion are not satisfied. In Schmidt & Sparenbergs derivation of the spiral flow these conditions at

infinity were not found. By starting with the finite spiral we have been able to complete the solution. The final result is that this solution indeed presents the flow induced by an infinite exponential spiral, but that it requires a multi-branched surface to be described consistently. Therefore it does not represent a 2-D flow induced by such a spiral.

Appendix C

THE VISCOUS SOLUTION OF THE FLOW INDUCED BY A SEMI-INFINITE, INFINITELY THIN ACTUATOR STRIP

In section 5.3 we presented a dimension analysis regarding a semi-infinite, infinitely thin actuator strip with constant, normal load and with no undisturbed flow present. It appeared that an inviscid solution can be obtained only if the ratio ϵ/ν (thickness to kinematic viscosity) is infinite. If the strip is a priori assumed to be infinitely thin, instead of defining a limit $\epsilon \rightarrow 0$, the ratio ϵ/ν is unknown. Assuming that this ratio is finite, only a viscous flow is possible.

The viscous solution is presented in this appendix, which is based on van Helden [1988]. The curl of the Navier-Stokes equation (5-5) for 2-D flows is:

$$\frac{\partial \underline{\omega}}{\partial t} = \frac{1}{\rho} \underline{\nabla} \times \underline{f} + (\underline{v} \cdot \underline{\nabla}) \underline{\omega} + \nu \nabla^2 \underline{\omega} . \quad (C-1)$$

The flow is assumed to start from rest, so at $t = 0$ the non-linear term $(\underline{v} \cdot \underline{\nabla}) \underline{\omega} = 0$. Since $\partial \underline{\omega} / \partial t$ and $\underline{\nabla} \times \underline{f}$ are non-zero only at the edge, and $\nu \nabla^2 \underline{\omega}$ has no preferential direction, the flow will be circular symmetric with respect to the edge and $(\underline{v} \cdot \underline{\nabla}) \underline{\omega}$ remains zero for $t > 0$.

With (r, Θ) as polar coordinates and the edge as origin, (C-1) is written as:

$$\frac{\partial \underline{\omega}}{\partial t} = -\nu \frac{\partial}{r} \frac{\partial}{\partial r} \left(r \frac{\partial \underline{\omega}}{\partial r} \right) + \frac{1}{\rho} \underline{\nabla} \times \underline{f} . \quad (C-2)$$

First $\frac{1}{\rho} \underline{\nabla} \times \underline{f}$ is treated as a unit point source in space and time: it is the result of a pulse at $t = 0$ and $r = 0$. The exact solution of (C-2) for $t > 0$ is:

$$\omega(r, \Theta, t) = \frac{1}{\nu t} e^{-\frac{r^2}{4\nu t}} . \quad (C-3)$$

Now $\nabla \times \underline{f} \neq 0$ for $0 \leq t \leq t_0$. Since (C-2) is linear, the solution is obtained by integration of (C-3):

$$\omega(r, \Theta, t) = \int_0^{t \text{ or } t_0} \frac{1}{\nu(t-\tau)} e^{\frac{-r^2}{4\nu(t-\tau)}} d\tau . \quad (\text{C-4})$$

The upper boundary of integration must be the lowest value of t and t_0 . By substitution of $p = r^2/4\nu(t-\tau)$, (C-4) simplifies to:

$$\omega(r, \Theta, t) = \int_{p_0}^{p_1} \frac{e^{-p}}{p} dp , \quad (\text{C-5})$$

with

$$\begin{aligned} p_0 &= r^2/4\nu t \\ p_1 &= \infty && \text{if } t \leq t_0 \\ &= r^2/4\nu(t-t_0) && \text{if } t > t_0 . \end{aligned}$$

If $t \leq t_0$, the definite integral is known as the exponential integral $E_1(r^2/4\nu t)$, which is tabulated in e.g. Abramowitz & Stegun [1965,p.228]. For $t > t_0$, the solution is the difference of two exponential integrals, so:

$$\begin{aligned} \omega(r, \Theta, t) &= E_1\left[\frac{r^2}{4\nu t}\right] && \text{if } t \leq t_0 \\ &= E_1\left[\frac{r^2}{4\nu t}\right] - E_1\left[\frac{r^2}{4\nu(t-t_0)}\right] && \text{if } t > t_0 . \end{aligned} \quad (\text{C-6})$$

Appendix D

THE FORCE ON A 2-D DISCRETE VORTEX OBTAINED BY AN ACTUATOR STRIP LIMIT

The actuator strip is a distribution of force densities on a 2-D infinitely thin strip. If the length of the strip is also assumed to tend to zero, meanwhile maintaining a resultant load, an isolated, discrete force \bar{F} is the result. If this discrete force is perpendicular to the main flow, the resultant flow should be a vortex flow. We investigate this for both actuator strip concepts which are discussed in the main text: Froude's concept of a strip with a uniform load, and the concept of a strip with a uniform load and edge forces.

We assume the Froude's classical actuator strip concept with the uniform surface load F . The resultant load is $\bar{F} = F\ell$, where ℓ is the strip length. A finite force \bar{F} requires $F \rightarrow \infty$ for $\ell \rightarrow 0$. By applying Bernoulli's law separately upstream and downstream of the strip, as in (3-2), it is clear that $\frac{1}{2}\rho(u_{\infty}^2 - U_0^2)$ is proportional to F , where u_{∞} is the velocity in the fully developed wake. The mass of fluid passing the actuator strip is proportional to $\ell F^{1/2}$, so the power needed to maintain the flow is proportional to $\ell F^{3/2}$ which becomes infinite in this limit. Therefore the classical strip, submitted to the limit of vanishing dimension, cannot yield the 2-D vortex flow as this flow requires no power to be put into the flow.

Now we assume an actuator strip with constant normal load F and two edge forces $\bar{F}_{\perp\psi} = -\rho \bar{v} \times \underline{\Gamma}$ as given by (8-13), placed parallel to the ambient flow \underline{U}_0 (figure D.1). The flow singularity at the edges is assumed to be the vortex singularity as derived in section 8.1.

The edge forces depend only on the local velocity \bar{v} , and vortex strength $\underline{\Gamma}$. Both are determined by the undisturbed velocity U_0 and the load on the strip F . Due to the asymmetry of the flow with respect to the strip symmetry line, the edge vortices will have unequal strength. This does not change if the length of the strip ℓ is changed. The limit $\ell \rightarrow 0$ keeping F constant results in the following changes of the flow:

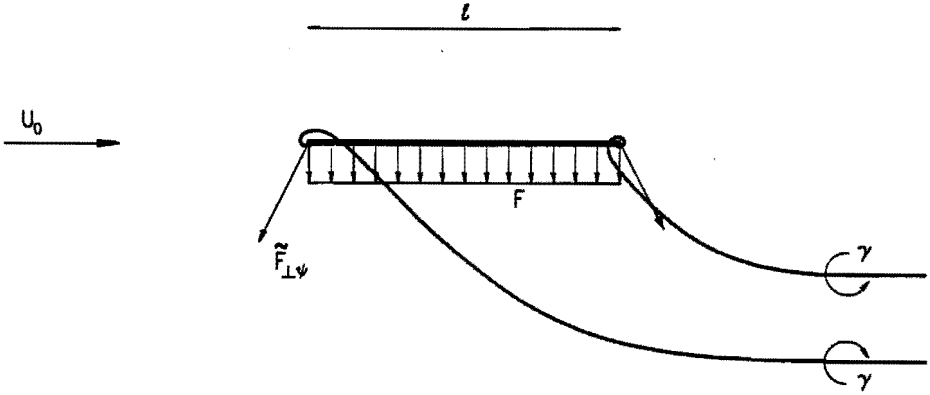


Figure D.1. An actuator strip with asymmetric flow.

- the mass of flow transported in the wake becomes zero: the velocity increase remains finite due to the finite \underline{F} , while the width of the wake becomes zero. The work done by the force field also becomes zero.
- the two vortex sheets cancel each other except at the edges. For $l \rightarrow 0$ this cancellation occurs at an infinitely small distance r . The two edge vortices constitute a vortex doublet. As the strength of the vortices is and remains unequal for $l \rightarrow 0$, one discrete vortex remains with strength $\Gamma \neq 0$, being the difference of the two edge vortices. The order of Γ is not known.
- the velocity induced by a discrete vortex at its own position is zero, so $\underline{\bar{v}} = \underline{U}_0$. The resultant force on the resultant vortex then is:

$$\underline{\tilde{F}}_{\perp\psi} = -\rho \underline{U}_0 \times \underline{\Gamma} , \tag{D-1}$$

so indeed the well-known vortex flow is the result of this limit procedure.

The conclusion of this reduction of absurdum proof is the following: the compression of the strip into a discrete point, meanwhile maintaining a resultant load, does not yield the vortex flow unless edge force are assumed to be present.

Appendix E

JUSTIFICATION OF THE EXPERIMENT

E.1. Model description

The model is a stripped version of the Graupner "sky-Lock EH-1" model helicopter: only the (electrical) drive mechanism and the two blades are used. The blades are untwisted and have a fixed pitch angle Θ_p and a stiff blade root mounting. The pitch angle is measured as the angle between the rotor plane and the flat lower side of the blade profiles. The profile itself is not specified. Figure E.1 shows the blade data. Figure E.2 sketches the experimental set up and the surroundings. Figure 4.4 in chapter 4 shows the model and the hot wire support.

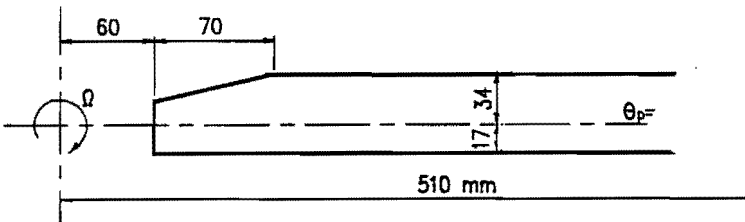


Figure E.1. Rotor blade geometry

E.2. Description and calibration of the measurement devices

The hot wires used are university-made wolfram wires, length 5 mm, thickness 5μ , without coating, mounted normal to the probe axis. The control equipment is also university-made and is based on the constant temperature anemometry. The wires are calibrated in a DISA calibration nozzle in the range $v = 0$ to 12 m/s. King's relation between wire voltage E and velocity v : $E^2 = A + Bv^\alpha$ is used as calibration curve. A numerical curve fit determines the constants A , B and α with an accuracy of $\approx 1\%$. Each day of measuring the calibration is repeated.

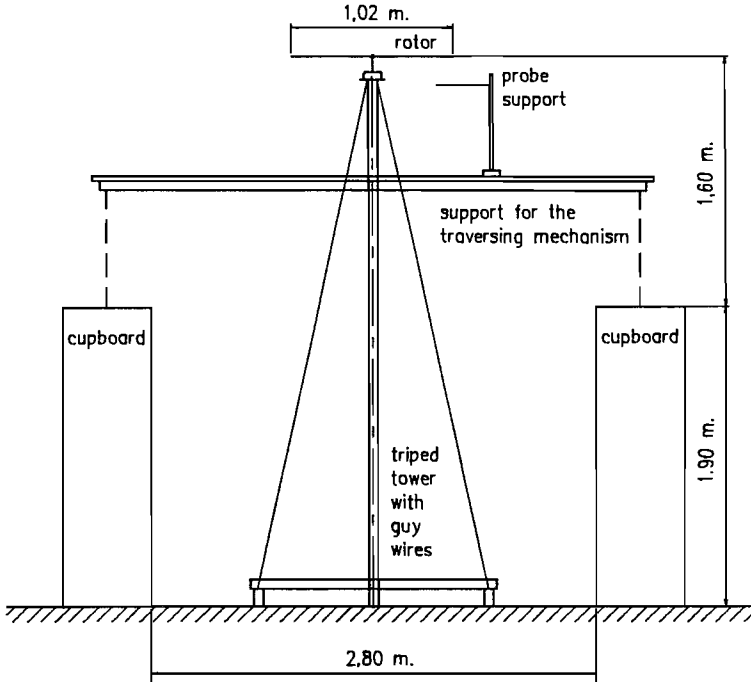


Figure E.2. The experimental set up

The wires are also calibrated for the sensitivity to the velocity component in the direction of the wire. Wires with a very high length-to-diameter ratio should register only the normal component v_n of the velocity \underline{v} , or:

$$v_{\text{measured}} = |\underline{v}| \cos \alpha , \quad (\text{E-1})$$

where α is the angle between \underline{v} and the plane normal to the wire. Figure E.3 shows the calibration. The angle α is varied by rotating the probe around an axis normal to the plane of the wire and wire supports. Indeed (E-1) is satisfied. The deviation for $\alpha \rightarrow 90^\circ$ is due to interference with the wire supports, which is unavoidable.

The total pressure tubes have an inner diameter of 7.5 mm, and an outer diameter of 1.2 mm diameter. This tube is calibrated with respect to misalignment errors. This is done in a closed wind tunnel. With α as the angle between flow direction and tube axis, the relative error is $< 1.5\%$ for $\alpha < 20^\circ$, see figure E-5.

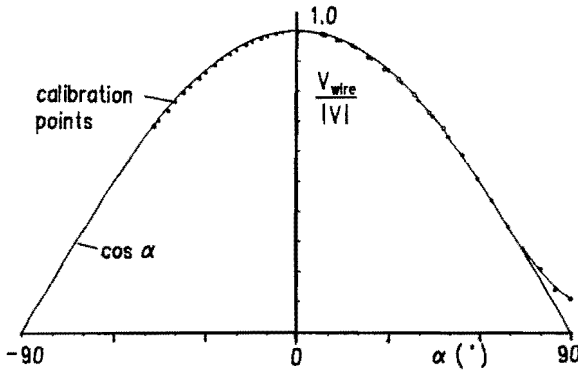


Figure E.3. Calibration of the hot wire with respect to cross wind sensitivity.

E.3. Hot wire data processing

This consists of two parts: data recording and evaluation. The recording is performed using a transient recorder (8 bits accuracy, GOULD Biomation 2805) and a personal computer. The recorders take 2000 data with a sample time of $5 \mu\text{s}$. At the same time the one-per-rev trigger pulse is recorded. These data (covering approximately 9 revolutions) are transmitted to the computer and stored on floppy discs. The software used is university-made. The entire system is calibrated by sampling and storing a known input voltage.

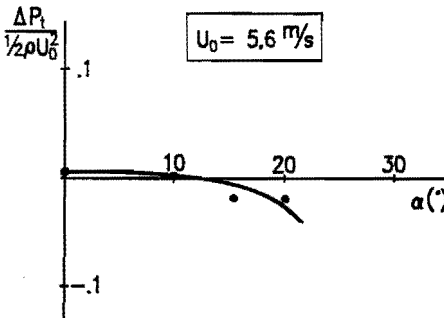


Figure E.4. Calibration of the total pressure tube with respect to misalignment.

The evaluation is described in van der Hoek & Pel [1987, in Dutch]. First the constancy of the rotor rpm is checked: only periods (data blocks between two trigger pulses) having 222 ± 1 data points are admitted. If the block contains 223 data points, number 223 is skipped; if the total is 221 points, number 222 is added being equal to number 221. Then the calibration curve is used to calculate the velocity. Finally all values having the same sequence number (ranging from 1 to 222) are averaged in order to obtain the magnitude of the local velocity component normal to the wire.

Appendix F

THE BOUNDARY LAYER FLOW FOR INFINITE REYNOLDS NUMBERS

In chapter 5 the question was raised whether the non-dimensional viscous term $Re^{-1} \nabla^2 \underline{y}'$ in the Navier-Stokes equation can remain finite if the Reynolds number Re is increased indefinitely. The dash above \underline{y} indicates that it is a non-dimensional term, as in section 5.1. Here we investigate this question for the flow along a solid boundary, using two different methods. The viscous solution is known by a special form of the Navier-Stokes equation: Prandtl's boundary layer equations, which are subjected to the limit $Re \rightarrow \infty$. The second approach is to use (5-5), where the shear stress is included in the force density term \underline{f} , together with the no-slip condition. The Reynolds number is assumed to be infinite. The solution for the force density distribution will show whether a tangential $\underline{f}_{\text{shear stress}}$ is present.

We use the same non-dimensional representation as in (5-3). In a local, 2-D, cartesian x' - y' coordinate system with x' tangent and y' normal to the surface, Prandtl's boundary layer equations read according to Meyer, [1982, page 116]:

$$\begin{aligned} \frac{\partial u'}{\partial x'} + \frac{\partial u'}{\partial y'} &= 0 \\ u' \frac{\partial u'}{\partial x'} + v' \frac{\partial u'}{\partial y'} &= -\frac{\partial p'_e}{\partial x'} + \frac{1}{Re} \frac{\partial^2 u'}{\partial y'^2} \\ \underline{v}' &= 0 \quad \text{for } y' = 0 \\ \lim_{y' Re^{\frac{1}{2}} \rightarrow \infty} u'(x', y') &= u'_e(x', 0) \end{aligned} \quad (F-1)$$

The index e denotes the "potential flow" values just outside the boundary layer. At $y' = 0$ so at the surface itself, the first two equations of (F-1) degenerate into:

$$\frac{\partial p'_e}{\partial x'} = \frac{1}{\text{Re}} \frac{\partial^2 u'}{\partial y'^2} \quad \text{at } y' = 0 \quad (\text{F-2})$$

Since the left-hand side is independent of Re , also $\frac{1}{\text{Re}} \frac{\partial^2 u'}{\partial y'^2}$ remains constant for $\text{Re} \rightarrow \infty$. Returning to the original notation with dimensions, this shows that the viscous stress term $\mu \frac{\partial^2 u}{\partial y^2}$ remains non-zero at a solid surface even if the Reynolds number is infinitely large. This result seems to contradict the well-known statement that the viscous drag of a body in inviscid flow is zero. However, the local drag is $\int \mu \frac{\partial^2 u}{\partial y^2} dy$ integrated across the thickness of the boundary layer. Since the integrand is finite and thickness is infinitely thin for $\text{Re} \rightarrow \infty$, the local drag is zero. Therefore the finite order of magnitude of the viscous term for $\text{Re} \rightarrow \infty$ is of mathematical interest only. This may be different for flows where a singularity is present: the order of the viscous term may be increased then.

Now we try the second approach by using the steady version of (5-5) with \underline{f} defined by (5-4). Figure F.1 shows a solid surface S with the local system (x, y) , with x tangent to the surface and y normal to it. The surface itself is denoted by $y = 0$, while $y = 0_+$ represents the situation just outside the surface. \underline{f} is distributed on S .

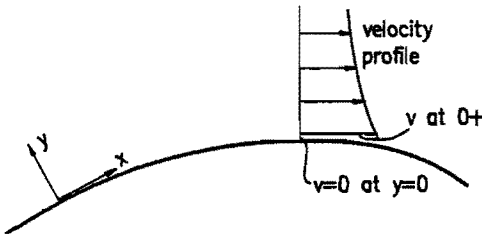


Figure F.1. Flow along a surface S with the no-slip condition

At the surface the no-slip condition gives:

$$\begin{aligned} y_0 &= 0 \\ p_0 &= p_{0+}, \end{aligned} \quad (\text{F-3})$$

so the Bernoulli constant is:

$$H_0 = p_{0_*} \quad (F-4)$$

Using (F-3), (5-5) gives for the tangential derivative of H:

$$f_{\text{tang}} = \frac{\partial}{\partial x} H_0 \quad \text{at } y = 0. \quad (F-5)$$

The combination with (F-4) yields:

$$f_{\text{tang}} = \frac{\partial}{\partial x} p_{0_*} \quad \text{at } y = 0. \quad (F-6)$$

Since:

$$\frac{\partial}{\partial x} p_{0_*} = \frac{\partial}{\partial x} (p_{0_*} - p_0) = \frac{\partial}{\partial x} F_{\text{normal}} \quad (F-7)$$

the relation between tangential and normal force distributions finally becomes:

$$f_{\text{tang}} = \frac{\partial}{\partial x} F_{\text{normal}} \quad (F-8)$$

F_{normal} can be expressed in kinematical terms using the Bernoulli equation for $y = 0_*$:

$$\frac{\partial}{\partial x} \left[p + \frac{1}{2} \rho v^2 \right]_{0_*} = 0 \quad (F-9)$$

The combination of (F-7) and (F-9) then yields:

$$\begin{aligned} F_{\text{normal}} &= e_y \left[-\frac{1}{2} \rho v_{0_*}^2 \right] \\ &= -\rho \bar{v} \times \gamma, \end{aligned} \quad (F-10)$$

with:

$$\left. \begin{aligned} \gamma &= -\mathbf{e}_y \times (\mathbf{v}_{0+} - \mathbf{v}_0) = -\mathbf{e}_y \times \mathbf{v}_{0+} \\ \bar{\mathbf{v}} &= \frac{1}{2}(\mathbf{v}_{0+} + \mathbf{v}_0) = \frac{1}{2}\mathbf{v}_{0+} \end{aligned} \right\} \quad (\text{F-11})$$

Equation (F-11) is a well-known expression. Due to the no-slip condition, the surface is a vortex sheet with strength γ and velocity $\bar{\mathbf{v}}$ on which a force is acting.

Also f_{tang} can be expressed in $\bar{\mathbf{v}}$ and γ :

$$\begin{aligned} f_{\text{tang}} &= \mathbf{e}_x \frac{\partial}{\partial x} F_{\text{normal}} = \mathbf{e}_x \frac{\partial}{\partial x} \left[-\frac{1}{2} \rho v^2 \right]_{y=0+} \\ &= -\rho \left[\left[\underline{\mathbf{v}} \cdot \underline{\nabla} \right] \underline{\mathbf{v}} + \underline{\mathbf{v}} \times \underline{\nabla} \times \underline{\mathbf{v}} \right]_{y=0+} \end{aligned} \quad (\text{F-12})$$

The flow is free of rotation at $y = 0_+$, so this simplifies to:

$$f_{\text{tang}} = -\rho \left[\left[\underline{\mathbf{v}} \cdot \underline{\nabla} \right] \cdot \underline{\mathbf{v}} \right]_{y=0+} \quad (\text{F-13})$$

(F-8), (F-10) and (F-13) constitute the relations between the tangential force density and normal surface force on the one hand and the velocity and vorticity on the other hand. Only for constant, normal surface forces, f_{tang} and the increase of γ are zero. All other distributions require $f_{\text{tang}} \neq 0$, by which the strength of the vortex sheet is increased or decreased. In other words: the generation of a vortex sheet at a solid surface supposes the presence of tangential force densities, which implies a non-constant normal force distribution.

The result (F-6/8) is the same as (F-2), but now obtained without using the boundary layer equations. It is clear that $f_{\text{tang}} = f_{\text{shear-stress}} = \mu \nabla^2 \underline{\mathbf{v}}$, and that both methods are equivalent.

Samenvatting

De remmende/trekkende schijf (actuator disc) is het eerste wiskundige model van een propeller, helikopter- of windturbine rotor, een eeuw geleden door R.E. Froude ontwikkeld. Deze schijf is oneindig dun en heeft een doorlaatbaar oppervlak waarop een uniform krachtveld is aangebracht. Dit krachtveld stelt de kracht van de rotor voor, en versnelt of vertraagt de stroming. Deze wordt verondersteld wrijvingsloos te zijn. De voorspelling van de prestaties van rotoren door middel van de, op dit concept gebaseerde, impulsstheorie is erg eenvoudig en wordt nog veelvuldig toegepast. Echter het vermogen dat rotoren aan de stroming toevoeren of onttrekken is systematisch 10 tot 15% hoger dan het vermogen dat door de impulsstheorie voorspeld wordt. Nu is uit de ontwikkeling van rotoren waarbij op een kunstmatige manier het rotorvermogen is opgevoerd, b.v. door de rotor in een ringvleugel te plaatsen of te voorzien van tipvanen, een tweede schijfmodel bekend: het model van Froude met daaraan krachten op de rand van de schijf toegevoegd. Dit schijfmodel met randkrachten leidt tot hogere waarden van het voorspelde vermogen dan Froude's model. De vraag is nu of het model met randkrachten niet een betere voorstelling is van rotoren, ook zonder ringvleugels of tipvanen, dan Froude's model zonder randkrachten.

Op twee manieren is hierop een bevestigend antwoord gevonden. Een verschil tussen beide schijfmodellen is dat in Froude's model alle krachten die op de schijf werken arbeid verrichten, terwijl dat niet het geval is in het model met randkrachten: deze krachten staan loodrecht op de lokale stroming en verrichten geen arbeid. Uit een analyse van het krachtveld van een rotorblad blijkt dat ook hier slechts een deel van het krachtveld arbeid verricht, zodat het schijfmodel met randkrachten een betere benadering is voor de rotor dan het model zonder randkrachten. Dit is tevens experimenteel bevestigd door metingen uit te voeren aan een schaalmodel van een stilhangende helikopterrotor. Uit de snelheids- en drukmetingen in het zog van deze rotor blijkt dat inderdaad slechts een deel van de totale kracht arbeid verricht. De overeenkomst tussen voorspelde en gemeten prestaties blijkt duidelijk verbeterd te zijn door het toevoegen van de randkrachten aan Froude's model: de kontrakctie van het zog wordt goed voorspelt door de impulsstheorie met randkrachten, maar de voorspelde snelheid door het rotorvlak is nog te laag, al is de overeenkomst met de gemeten waarde duidelijk beter dan bij de voorspelling zonder randkrachten.

In het tweede gedeelte van het proefschrift wordt de vraag gesteld of de randkrachten een inherent onderdeel van de trekkende/remmende schijf zijn, in plaats van een vrij te kiezen toevoeging. Hiervoor is zowel numeriek als analytisch de relatie tussen een

krachtveld en de daardoor geïnduceerde stroming bestudeerd, waarbij dit krachtveld geen relatie met een rotor hoeft te hebben. Uit de literatuur zijn experimentele en numerieke resultaten bekend van stromingen geïnduceerd door krachtvelden op schijven, welke strijdig lijken met Froude's theorie. Ter verifiëring hiervan is een eigen numerieke studie verricht. Deze betreft de viskeuze, twee-dimensionale stroming geïnduceerd door een trekkende schijf met dikte, belegd met een vloeiend verlopemd krachtveld. Vervolgens is, zoveel als het computerprogramma het toeliet, het Reynoldsgetal opgevoerd, de dikte naar nul teruggebracht en de krachtveldverdeling aan de randen steiler gemaakt. Door extrapolatie van de resultaten wordt dan het geïnduceerde vermogen benaderd van de niet-viskeuze stroming door een oneindig dunne schijf met een uniforme krachtverdeling. De uitkomst van deze extrapolatie is gelijk is aan de voorspelling op basis van Froude's model. Tevens geeft deze studie een interretatie van sommige van de genoemde numerieke en experimentele resultaten. Eén experimenteel en één numeriek resultaat uit de literatuur, beide niet in overeenstemming met Froude's model maar wel met het model met randkrachten, kunnen niet verklaard worden.

De analytische studie heeft geresulteerd in een exacte oplossing van de vergelijking van Wu, welke de basis is van alle numerieke methodes ter berekening van de schijfstromingen. Voor niet-uniforme krachtvelden welke twee dimensionaal zijn of drie dimensionaal zonder een azimuthale komponent, is afgeleid dat een verdeling van alleen een normaal krachtveld niet kan bestaan: zo'n verdeling vereist de aanwezigheid van een tangentiaal krachtveld. De verklaring voor het optreden hiervan is nog niet volledig. Een hypothese is dat dit krachtveld de schuifspanning voorstelt welke verbonden is met het opwekken van wervelsterkte. Een voorwaarde hiervoor is dat de orde van deze schuifspanning eindig blijft, ook al gaat het Reynoldsgetal naar oneindig. Voor één bijzonder geval is dit aangetoond. Daarnaast is de stroming op de rand van Froude's schijf bestudeerd. De krachtsverdeling is hier discontinu, en veroorzaakt een singulariteit in de stroming: een wervel. Indien de stroming stationair is draagt deze wervel een kracht. De ordegraote hiervan is de ordegraote van de snelheid ter plaatse van de singulariteit, welke ongelijk nul maar verder onbekend is. De grootte van de randkracht kan dus oneindig klein zijn. Dit is pas bekend na een analytische of numerieke studie betreffende het gehele stromingsveld geïnduceerd door schijven met een uniforme normaalbelasting.

Nawoord

Allereerst wil ik prof. Vossers en Paul Smulders bedanken voor het feit dat zij het initiatief hebben genomen de promotiebaan te creëren, die ik 4 jaar in Eindhoven vervuld heb. Niet gehinderd door enige financiële verantwoording of formele voortgangsrapportages heb ik gewoon kunnen werken, wat in deze tijd van kontraktresearch steeds minder voorkomt. De behoefte aan dit promotiewerk is voortgekomen uit de windenergiegroep o.l.v. Paul Smulders. Door de activiteiten van deze groep heb ik ook het nodige geleerd op waarschijnlijk het moeilijkste toepassingsgebied van windenergie: het oppompen van water door windmolens die het met een minimum aan onderhoud en maximum aan betrouwbaarheid gedurende tientallen jaren moeten doen, zonder enige bewaking of sturing van buitenaf.

Ik ben veel verschuldigd aan mijn kamergenoot en stille stimulans Bram Wijnands. Bovendien waren zijn hulp en adviezen, en ook die van Louis Wasser en Eep Voorthuizen hard nodig bij het experiment.

De discussies over het onderzoek zijn een onmisbaar element van het onderzoek zelf, en hebben vele fouten en slordigheden mijnerzijds blootgelegd. Miko Hirschberg heeft mij meerdere malen het vuur aan de schenen gelegd, uiteindelijk tot beider voldoening. Het bewaken van de grote lijn door prof. Vossers en het nauwgezette commentaar van prof. Schram hebben mij zeer veel geholpen. Paul Smulders wist regelmatig verwarring te scheppen door de vinger op al dan niet vermeende zwakke plekken in de redenering te leggen: dit leidde altijd tot meer helderheid. Tenslotte hebben Gerrit Schouten, Nord-Jan Vermeer en de hoogleraren Dragt en Steketee, allen van de TU-Delft, het nodige bijgedragen ter verbetering van het proefschrift.

Het onderzoek heeft gelukkig ook enige studenten aangesproken: het experiment is mede voorbereid en uitgevoerd door Pieter Beekman, Karin van Schijndel, Hans van der Hoek en Leo Pel. Aan het analytische en numerieke werk hebben Roel Kusters, Alex van der Spek, Wim van Helden en René Peeters meegewerkt.

Het boekje zelf is het laatste loodje. Gelukkig heeft Riet Bedet het meeste typewerk gedaan; toen ik later zelf de tekstverwerker de baas moest worden hebben Irene de Jong en Henk Oldenkamp mij bij nacht en ontij geholpen. De meeste tekeningen zijn gemaakt door Toon Nijman en Martin Lemmen van Stork Product Engineering.

Tot slot: promoveren eindigt vroeg of laat in een aanslag op alle andere activiteiten en op het geduld van je partner. Ik bedank haar ervoor dat dit geduld groot genoeg is gebleken.

Curriculum vitae

- 31 mei 1951 geboren te Mierlo.
- 1969 diploma gymnasium β te Helmond.
- sept. 1969 - jan. 1977 studie aan de Technische Universiteit Delft, faculteit der Luchtvaart- en Ruimtevaarttechniek, afstudeerrichting theoretische stromingsleer.
- jan. 1977 - april 1984 in dienst bij de Technische Universiteit Delft, faculteit der Luchtvaart- en Ruimtevaarttechniek, windenergie groep.
- mei 1984 - mei 1988 in dienst bij de Technische Universiteit Eindhoven, faculteit der Technische Natuurkunde, vakgroep Transportfysica, windenergie groep.
- mei 1988 - in dienst bij Stork Product Engineering, Amsterdam, hoofdtak onderzoek en ontwikkeling van windturbine technologie.

Stellingen behorende bij het proefschrift
"On the limitations of Froude's actuator disc concept"
van G.A.M. van Kuik.

1. Sabinin heeft het maximale rendement van een ideale windmolen analytisch vastgesteld op 69%, hetgeen 1,15 keer het Lanchester-Betz maximum is. Hoewel dit resultaat gestaafd wordt met experimentele gegevens, is de berekening onjuist vanwege de incorrecte voorstelling van het begin van de stroombuis door de rotor: Sabinin laat het begin van het wervelvlak dat deze stroombuis omhult niet oprollen tot een startwervel.

C.N.H. Lock, 1928, A discussion of "The theory of an ideal windmill" by G. Sabinin and a summary of experimental results of windmills, A.R.C. report T.2615.

2. Lighthill heeft een analytisch model ontwikkeld voor de stroming door een tweedimensionale trekkende schijf met uniforme belasting zonder hoofdstroming, door te veronderstellen dat deze stroming equivalent is aan die door Borda's tuit. Een belangrijk argument hiervoor is dat volgens Lighthill het schijfmodel niet consistent is bij de rand. Echter, het drukveld bij de rand van de schijf wordt gekenmerkt door oneindige gradiënten, terwijl deze eindig zijn bij de rand van de tuit. Dit is geen aanleiding om een inconsistentie te veronderstellen in de schijfstroming.

J. Lighthill, 1979, A simple fluid flow model of ground effect on hovering, Journal of Fluid Mechanics, 92, p. 781.

3. De Schmidt & Sparenberg spiraalstroming behoort tot de klasse van oplossingen van Prandtl voor de potentiaalstroming om half-oneindige logaritmische spiralen. Indien deze spiraalstromingen beschouwd worden als zijnde het limietresultaat van stromingen om eindige spiralen, waarvan de lengte naar oneindig gaat zoals beschreven in appendix B, dan geldt voor deze gehele klasse de volgende konklusie: de stroming om de half-oneindige Prandtl spiralen kan niet als een tweedimensionale stroming worden beschouwd omdat op oneindig niet wordt voldaan aan de Laplace vergelijking voor de potentiaal. Dit verklaart waarom er nooit een fysische betekenis voor deze klasse van spiralen gevonden is.

L. Prandtl, 1924, Über die Entstehung von Wirbeln in der idealen Flüssigkeit, mit Anwendung auf die Tragflügeltheorie und andere Aufgaben, uit: Vorträge auf dem Gebiete der Hydro- und Aerodynamik, door von Karman en Levi-Cevita, p. 18, Springer Verlag, 1924, Berlin.

Appendix B van dit proefschrift.

4. In de meeste handboeken voor rotoraerodynamica wordt vermeld dat de optimale circulatie verdeling voor propeller- of helikopterbladen een uniforme verdeling is. Dit is echter alleen aangetoond voor schijven met een continu verdeelde belasting en niet voor rotoren met een eindig aantal bladen. Het is dan ook niet vreemd dat Miller met een numerieke methode vindt dat een niet-uniforme verdeling beter is dan de uniforme verdeling.

R. H. Miller, 1982, A simplified approach to the free wake analysis of a hovering rotor, Vertica, 2, p. 89.

5. In een ideale wrijvingsloze, onsamendrukbare vloeistof Bernoulli's wet voor stationaire stromingen opgevat worden als het equivalent van het behoud van mechanische energie voor ideale massadeeltjes (zie Batchelor). Het drukverschil t.o.v. een vrij te kiezen referentie druk stelt dan de potentiële energie voor. Deze interpretatie van Bernoulli's wet maakt de samenhang tussen vloeistofmechanica en deeltjesmechanica duidelijker zichtbaar dan de "totale druk" interpretatie die men in de meeste leerboeken aantreft.

G.K.Batchelor, 1970, An introduction to Fluid Dynamics, Cambridge University Press, p. 157.

6. In een twee-dimensionale, rotatievrije stroming van een wrijvingsloze onsamendrukbare vloeistof geldt niet alleen de Laplace vergelijking voor de snelheidspotentiaal, maar ook voor een dimensieloze versnellingspotentiaal. Deze is gedefinieerd als de logaritme van het quotiënt van de totale en dynamische druk.

Th. van Holten, niet gepubliceerd werk.

7. Het tipvaan onderzoek beoogt door een vergroting van de massastroom door een windturbine het rendement hiervan te verbeteren. Het is echter vastgelopen op de geïnduceerde weerstand van de tipvanen. Deze is in de loop van het onderzoek reeds gereduceerd tot 30% van de weerstand van vleugels van dezelfde afmetingen, door het neutraliseren van de opgerolde tipwervel. Niet alle losgelaten wervelsterkte komt in de tipwervel terecht. Een volledige opheffing van de geïnduceerde weerstand vereist dat ook het overblijvende wervelvlak wordt geneutraliseerd. Een verdere voortgang van het onderzoek vereist dan ook een veel verfijnder aerodynamisch model voor het beschrijven van de wervelstructuur dan tot nu toe is gebruikt.

8. De publikatie van Rauh & Seelert bediscussieert de theorie van Betz betreffende het rendement van een ideale windturbine. Hun voornaamste punt van kritiek, nl. dat de druk op de wand van de stroombuis die door de windturbine gaat een bijdrage kan leveren in de impulsbalans terwijl Betz deze bijdrage weglaat, is reeds in 1925 door Thoma weerlegd. Verder citeren ze de verkeerde publikatie van Betz als zijn eerste publikatie over dit onderwerp.

A. Rauh, W. Seelert, 1984, The Betz optimum efficiency for windmills, Applied Energy, 17 p. 15.

D. Thoma, 1925, Grundsätzliches zur einfachen Strahltheorie der Schraube, Zeitschrift für Flugmechanik und Motorluftschiffahrt, 10, p. 206.

9. Bij veel windturbines wordt het asvermogen bij hoge windsnelheden beperkt door het teveel aan uit de lucht opgenomen vermogen ter plaatse te dissiperen in warmte i.p.v. rechtstreeks minder vermogen op te nemen. Dit dissiperen gebeurt door de bladen te laten overtrekken. Zowel het uit de lucht opgenomen vermogen als het gedissipeerde vermogen variëren zeer sterk. Bovendien zijn bij een hoge windsnelheid beide grootheden van dezelfde orde. Het rotor-as vermogen, zijnde het verschil hiertussen, kan dan ook slechts grof geregeld worden, gepaard gaande met grote wisselingen van de belastingen. Hiermee wordt de turbine een vermoeingsmachine.

10. Hoeijmakers heeft een numerieke methode ontwikkeld voor de berekening van het oprollen van een continu wervelvlak. Hierbij wordt de kern van het opgerolde vlak vervangen door een discrete wervelijne welke met het wervelvlak verbonden is door een zogenaamd "feeding sheet". Dit leidt tot de introductie van een koppel ter plaatse van de opgerolde wervel. In aero-acoustische toepassingen betekent deze discretisatie dat een extra aero-acoustische quadrupool wordt geïntroduceerd. Bij twee-dimensionale berekeningen in een vlak loodrecht op het zog van een draagvlak, het zgn. Trefftz vlak, leidt deze discretisatie tot het niet constant zijn van de kinetische energie in dit vlak tijdens het oprollen. Hierdoor is deze methode ongeschikt om de geïnduceerde weerstand van het draagvlak te berekenen.

H.W.M. Hoeijmakers, 1989, Computational aerodynamics of ordered vortex flows, proefschrift, NLR rapport NLR TR 88088 U.

11. De televisiekursus "Klassieke Mechanica" van Teleac geeft Aristoteles te weinig eer van zijn werk door simpelweg te stellen dat zijn opvatting van rust als eindpunt van alle beweging foutief is. Het door Teleac getoonde voorbeeld van zijn ongelijk, nl. een balletje dat in een dalvormige schotel op en neer blijft rollen wanneer het eenmaal bovenaan is losgelaten, zou Aristoteles gelijk gegeven hebben als dit experimentje niet enige seconden maar enige minuten had geduurd.

12. Zolang in de pers nog gesproken wordt over stammenonlusten als het gaat over conflicten tussen volkeren in één land zoals in Zuid-Afrika, Namibië en Oeganda, terwijl gelijksoortige conflicten beschreven worden als nationaliteitskwesaties wanneer het Tjecho-Slowakije, Joegoslavië of Roemenië betreft, is er sprake van een Europees superioriteitsgevoel t.o.v. Afrika. Het gebruik van het woord "stammenonlusten" óók voor Europa zou dit gevoel snel relativeren.